Wu, Y.; Pena, L.D.; Anderson, R.F.; Hartman, A.E.; Bolge, L.L.; Basak, C.; Kim, J.; Rijkenberg, M.J.A.; de Baar, H.J.W; Goldstein, S.L. (2022). Assessing neodymium isotopes as an ocean circulation tracer in the Southwest Atlantic. *Earth Planet. Sci. Lett. 599*: 117846.

Published version: https://dx.doi.org/10.1016/j.epsl.2022.117846

Assessing neodymium isotopes as an ocean circulation tracer in the Southwest Atlantic

Yingzhe Wu[a,b,*], Leopoldo D. Pena[a,c], Robert F. Anderson[a,b], Alison E. Hartman[d], Louise L. Bolge[a], Chandranath Basak[a,e], Joohee Kim[a,b], Micha J.A. Rijkenberg[f], Hein J.W. de Baar[f,g], Steven L. Goldstein[a,b]

[a] Lamont-Doherty Earth Observatory of Columbia University, Palisades, New York 10964, USA

[b] Department of Earth and Environmental Sciences, Columbia University, New York 10027, USA

[c] Departament de Dinàmica de la Terra i l'Oceà, Universitat de Barcelona, Martí i Franqués, 08028 Barcelona

[d] Department of Analytical Services, Agricultural Experiment Station Chemical Laboratories, University of Missouri, Columbia, MO 65211, USA

[e] Department of Earth Sciences, University of Delaware, Newark, DE 19716, USA

[f] Department of Ocean Systems, NIOZ Royal Netherlands Institute for Sea Research and Utrecht University, Den Burg, the Netherlands

[g] University of Groningen, Groningen, the Netherlands

revised version for *Earth and Planetary Science Letters*

Abstract

The global overturning ocean circulation plays a key role in global climate by distributing heat around the Earth and by triggering or amplifying major climate changes. Neodymium (Nd) isotopes are widely used to trace present-day and past ocean circulation changes; however, their value as a circulation tracer has been increasingly challenged by studies that have focused on processes that can modify seawater Nd isotope ratios (for example, seawater interaction with particles, pore water fluxes from sediments). The Southwest Atlantic represents an excellent test bed for investigating the integrity of Nd isotopes as an ocean circulation tracer, as it includes the major Atlantic northern and southern hemisphere-sourced end-member water masses associated with the global overturning ocean circulation, Antarctic Intermediate Water, North Atlantic Deep Water, and Antarctic Bottom Water (AAIW, NADW, and AABW, respectively) and potential regional sources of Nd that could impact that integrity. This study reports Nd isotope data on the GEOTRACES GA02 Southwest Atlantic Meridional Transect, spanning the equator to ~50°S. Below the pycnocline, substantial non-conservative behavior is observed only in samples dominated by AAIW in the northern portion of the transect (~25°S to the equator); this appears to reflect addition of Nd from the cratons of South America or Africa from above the pycnocline. This effect is not observed at depths directly below dominated by NADW. Otherwise, Nd isotopes behave as a near-conservative water mass tracer along the transect, with 48% of samples within analytical error of the predicted value from water mass mixing, and 84% within 0.9 ε_{Nd}-units (~3 times the analytical error), thus confirming its potential at most depths and locations in the Southwest Atlantic to reconstruct past ocean circulation changes.

1. Introduction

The global overturning ocean circulation plays an essential role in the climate system, accumulating and redistributing heat around the Earth. However, tracing circulation in the past requires the application of chemical tracers that follow water mass movement. The application of Nd isotope ratios as a paleo-ocean circulation tracer is based on modern ocean observations, whereby its values vary by location and depth such that they fingerprint the globally important water masses and their mixing along their transport paths (Frank, 2002; Goldstein and Hemming, 2003; Tachikawa et al., 2017; van de Flierdt et al., 2016). However, many studies have focused on processes that could add external Nd to the water column throughout the oceans, for example, exchange with particulates along continental margins (Jeandel, 2016; Jeandel et al., 2007; Lacan and Jeandel, 2005b), inputs from rivers and wind-borne dusts (Goldstein et al., 1984; Stichel et al., 2015; Tachikawa et al., 1999), submarine groundwater discharge (Garcia-Solsona and Jeandel, 2020; Johannesson and Burdige, 2007; Johannesson et al., 2011), reversible scavenging of falling particles (Elderfield et al., 1988; Siddall et al., 2008), and benthic fluxes (Abbott, 2019; Abbott et al., 2015; Abbott et al., 2022; Du et al., 2020; Haley et al., 2017). These reservations have also been echoed in modeling studies (Arsouze et al., 2007, 2009; Pasquier et al., 2022; Pöppelmeier et al., 2020). Together they challenge the view that Nd isotopes show near conservative behavior in the present-day deep oceans, and its utility for tracing past ocean circulation.

This study presents Nd isotope ratios and abundances collected by the GEOTRACES GA02 Southwest Atlantic Meridional Transect *(SAMT)* between the equator and ~50°S, a region that encompasses the mixing zone between the main water masses of the Atlantic sector of the global meridional overturning ocean circulation *(AMOC)*. The Southwest Atlantic is also potentially affected by processes that add external Nd to the water masses (e.g. eolian dust, marginal sediments, oceanic volcanism, benthic nepheloid layers) with a variety of Nd isotope signatures. For these reasons, it is one of the best regions on Earth to investigate the integrity of Nd isotopes as an ocean circulation tracer and the impacts of addition of external Nd.

1.1 Nd isotopes in the Earth and the oceans

^{143}Nd is produced by radioactive decay of ^{147}Sm ($t_{1/2}$ = 106 Ga), and variations in Sm/Nd ratios over geologic time has caused ^{143}Nd/^{144}Nd ratios to vary in the Earth. The ^{143}Nd/^{144}Nd ratio is expressed as ε_{Nd}, the deviation in parts per 10,000 from average chondrite, which is an estimate of the bulk Earth; this study uses ^{143}Nd/^{144}Nd = 0.512638 (Jacobsen and Wasserburg, 1980), in order to be consistent with decades of past data, rather than the updated value of 0.512630 (Bouvier et al., 2008); although the difference is small, only 0.16 ε_{Nd} units (and both values are within analytical error). Because Sm/Nd ratios in the continents are ~40% lower than in the mantle, reflecting the way these elements fractionate during continent formation, and are similar in many continental lithologies, $^{143}Nd/^{144}Nd$ ratios in the continents mainly reflect how long the Nd has been in the continental crust (e.g. Goldstein et al., 1984). Old continental crustal rocks are sources of low ε_{Nd} (e.g. the cratons of Canada and Greenland have $\varepsilon_{Nd} < -20$), whereas young mantle-derived rocks are sources of high ε_{Nd} (e.g. North Pacific volcanic arcs have $\varepsilon_{Nd} > +7$) (e.g. Jeandel et al., 2007; Robinson et al., 2021). Nd in seawater is mainly derived from the continents, as reflected by negative ε_{Nd}-values. Its distribution in present-day oceans is characterized by highly negative ε_{Nd}-values in deep waters formed by overturning in the North Atlantic, surrounded by old cratons ($\varepsilon_{Nd} \approx -14$ to -13 in the deep North Atlantic and is < -20 in Baffin Bay) (Piepgras and Wasserburg, 1980, 1987; Stordal and Wasserburg, 1986); higher ε_{Nd}-values in deep waters of the North Pacific ($\varepsilon_{Nd} \approx -4$ to 0), influenced by input from young volcanics (Piepgras and Wasserburg, 1980, 1987); and intermediate ε_{Nd}-values in the Southern Ocean ($\varepsilon_{Nd} \approx -9$ to -8) (Piepgras and Wasserburg, 1982; Stichel et al., 2012). This spatial distribution reflects Nd's short ocean residence time (500-1500 years) compared to the ocean mixing time (Arsouze et al., 2009; Goldstein and O'Nions, 1981; Piepgras et al., 1979; Rempfer et al., 2011; Siddall et al., 2008; Tachikawa et al., 2003; Tachikawa et al., 1999). Early studies of seawater ε_{Nd} concluded that Nd behaves "quasi-conservatively" (almost conservatively) in the deep oceans (Frank, 2002; Goldstein and Hemming, 2003; Jeandel, 1993; Piepgras and Wasserburg, 1980, 1982; von Blanckenburg, 1999), with ε_{Nd} variations over long distances approximating those expected from conservative water mass mixing; this has been supported by recent data syntheses (Tachikawa et al., 2017; van de Flierdt et al., 2016) and studies associated with the international GEOTRACES Program (Behrens et al., 2018; Rahlf et al., 2020; Wang et al., 2021; Zieringer et al., 2019). Nevertheless, as already noted, several recent studies have focused on the effects of external addition of Nd along water mass transport paths, calling into question the utility of Nd isotopes as an ocean circulation tracer.

1.2 The GEOTRACES GA02 Southwest Atlantic Meridional Transect (SAMT)

The Southwest Atlantic is an excellent region to test how well ε_{Nd} behaves as a conservative water mass tracer in the modern ocean because it contains the main AMOC water masses: southward flowing Upper, Middle, and Lower North Atlantic Deep Water (*UNADW*, *MNADW* *and LNADW,* respectively, ε_{Nd} ~ −13.5), and northward flowing Antarctic Intermediate Water, Upper and Lower Circumpolar Deep Water, and Antarctic Bottom Water (*AAIW*, *UDCW*, *LCDW*, *AABW*, respectively, ε_{Nd} ~ −8) (Frank, 2002; Goldstein and Hemming, 2003; Tachikawa et al., 2017; van de Flierdt et al., 2016) (*Fig. 1*). Seawater profiles from 17 hydrographic stations, with 16 samples at each station, were collected between 49.5°S and 0.2°S (*Fig. 1a;* station numbers increase from south to north) during the Southwest Atlantic Meridional GEOTRACES cruise, (GA02 Leg 3; RRS James Cook 057, from Punta Arenas, Chile, to Las Palmas, Spain, March-April 2011) and analyzed for ε_{Nd} and Nd concentrations (*[Nd]*) (*Fig. S1*, *Table S1*). The data are also available online at https://www.bco-dmo.org/dataset/672203 (Wu et al., 2022).

The SAMT is also an exceptional natural laboratory to test the potential effects of external Nd inputs that may impact the ε_{Nd} of Southwest Atlantic water column, causing it to deviate from conservative behavior. The transect crosses the volcanic Rio Grande Rise (RGR; ~30°S) and Vitória-Trindade Ridge (VTR; ~20°S) (*Figs. 1b,c*), where a high-ε_{Nd} signal from oceanic basalts could be added to seawater. The SAMT also crosses major geological age boundaries of South American surficial rocks, where marginal sediments show the highest ε_{Nd}-values near Patagonia, intermediate values between the La Plata estuary and Southern Brazil, and the most negative values adjacent to the Precambrian cratons to the north (*Fig. 1a*). The cratons of central and southern Africa are potential sources of eolian dust with low ε_{Nd}-values, transported to the region by the trade winds. The SAMT also includes a benthic nepheloid layer *(BNL)* with resuspended particles observed within 500 m of the seafloor in the southern part of the transect between ~50°S to ~20°S (*Fig. S2*), which could potentially impact the bottom water ε_{Nd} by dissolution or exchange of resuspended sedimentary Nd.

2. Analytical procedures and water mass end-member calculations

Samples comprised five to ten liters of seawater, depending on the sample depth. They were filtered using 0.2 µm Sartobran® cartridges, acidified using ultrapure Seastar® hydrochloric acid (HCl) to pH ≈ 2 shortly after collection, and were stored. Detailed sample processing and analytical procedures for Nd isotopes and concentrations are given in the *Supplementary Information*. The analytical protocols followed the recommended GEOTRACES sampling and chemical treatment protocols for REEs and Nd isotopes (van de Flierdt et al., 2012).

In order to quantitatively evaluate the extent that seawater ε_{Nd} can be regarded as conservative, we performed an Optimum Multi-parameter Analysis (*OMPA*, modified from Poole and Tomczak, 1999, details are in the *Supplementary Information*) to estimate the fractional water mass compositions for each sample from a set of defined water mass end-members (*Figs. 2, S3, S4, S5; Table 1a*). The OMPA assumed isopycnal mixing in the intermediate and deep-ocean. We divided the water column along three neutral density bands (γ^n 27.1, 27.7, 28.1 kg/m^3), thus creating four layers designated as the *'Shallow'* (above the pycnocline, defined here as the 27.1 kg/m^3 isopycnal), and the *'Upper'*, *'Middle'*, and *'Lower'* deep water layers (*Figs. 1b, 3, 4, S6; and Supplementary Information*). The OMPA was not performed for the Shallow Layer samples because this part of the water column is subject to a large number of processes that are independent of the deep circulation, resulting in a large natural variability. The Upper, Middle, and Lower Layers are those governed by the AMOC.

The OMPA calculations used salinity (*S*), potential temperature (θ), dissolved oxygen (O_2), PO_4^*, N^*, and silicate (SiO_2) concentration (explained in detail in the *Supplementary Information*). PO_4^* and N^* the preformed phosphate ($\mathrm{PO_4^* = PO_4 + O_2/175 - 1.95}$) and nitrate ($\mathrm{N^* = 0.87 * (NO_3 - 16PO_4 + 2.95)}$) , both considered conservative water mass tracers (Broecker et al., 1991; Gruber and Sarmiento, 1997; Rae and Broecker, 2018). The hydrographic characteristics of each water mass were defined (*Fig. 2*) using the S-minimum for AAIW, the O_2-minimum for UCDW, the S-maximum for UNADW, the O_2-minimum for MNADW in the northernmost Stations 17 and 18, the O_2-maximum for LNADW in Stations 17 and 18, the S-maximum for LCDW in the southernmost Stations 1 and 2, and the lowest θ-value for AABW. In the Upper Layer, some of the samples included contributions from South Atlantic Central Water (*SACW)*. Its end-member compositions for the OMPA were defined based on the average values from the SAMT samples above the 27 kg/m^3 isopycnal and below the mixed layer. These SACW samples lie along a θ-S curve with large variability in both (34.48-35.63g/kg; 7.8-16.0°C) (*Fig. S6*). The ε_{Nd}- and [Nd]-values of SACW are defined separately for the southern stations (*SACWs*, Stations 1-12) and the northern stations (*SACWn*; Stations 13-18) (*Table 1a*), because the ε_{Nd}-values at the SACW θ-S-values are higher in the south and lower in the north, and [Nd] values are lower in the south and higher in the north (*Figs. 5a,b*; discussed in *Sections 3 and 4.2*).

The OMPA gave fractional estimates of the water mass mixtures for each sample from the Upper, Middle, and Lower Layers. The predicted ε_{Nd}-values (*Fig. 4b;* calculations are explained in the *Supplementary Information*) for samples within each Layer are calculated using water mass end-members within the same Layer (SACWs was used for Stations 1-12 and SACWn was used for Stations 13-18 in the Upper Layer) (*Figs. 1b, 3*), and are the ε_{Nd}-values expected if this tracer is truly conservative and if the end-member compositions are defined accurately. We also compared the measured and predicted ε_{Nd}-values (*Fig. 4c, $\Delta\varepsilon_{Nd}$ = measured minus predicted ε_{Nd}*) to evaluate how well the samples reflect conservative mixing.

3. Results

SAMT ε_{Nd}-values show a large range, ~ −18 to ~ −7, with the most extreme values in the top 100 m. ε_{Nd}-values of SACW samples, at 250-500 m depending on location, show almost the same range, ~ −15 to ~ −8 (*Fig. 5b*). The Shallow Layer ε_{Nd}-values, above the 27 kg/m^3 isopycnal, are higher in the south and lower in the north, reflecting younger crustal sources of dust or sediment reaching the Atlantic from Patagonia in the south versus older South American and/or African crustal sources in the north (*Figs. 1a,c, 5a,b*). Below the Shallow Layer, in the Upper, Middle, and Lower Layers that reflect the AMOC, ε_{Nd}-values are within the ranges of the major northern and southern sourced water masses (*Fig. 5c*). In all of the profiles, [Nd] shows fluctuations in the Shallow Layer but increases monotonically below it (*Fig. S1*), consistent with global observations (Goldstein and Hemming, 2003).

The SAMT salinity section profile (*Fig. 1b*) clearly distinguishes the major water masses, with southward flowing NADW marked by a high-S wedge that is sandwiched by northward flowing AAIW-UCDW and AABW-LCDW. Overall, the ε_{Nd}-section profile (*Fig. 1c*) strikingly resembles the S-profile, with ε_{Nd} clearly reflecting the southward thinning NADW wedge. S-θ-ε_{Nd} plots (*Fig. 3*) offer further insight into the relationships between these parameters. The high S-and-θ samples (S > 34.8g/kg, θ > 2°C), reflecting the Upper, Middle and Lower NADW end-members (*UNADW, MNADW, LNADW,* respectively*)*, have the lowest ε_{Nd}-values (−13 to −12), similar to the North Atlantic (Lambelet et al., 2016; Piepgras and Wasserburg, 1980, 1987), while the middle-to-lower S-low θ samples (S < 34.7g/kg, θ < 2°C), reflecting the southern water mass end-members (AABW, LCDW, UCDW and AAIW) have the highest ε_{Nd}-values (−9 to

−8), similar to the Southern Ocean (Piepgras and Wasserburg, 1982; Stichel et al., 2012). Other samples with θ-S values intermediate to these end-members show intermediate ε_{Nd}-values. The only significant discrepancy between the S- and ε_{Nd}-section profiles, showing a significant deviation from conservative water mass mixing, is north of Station 13 at ~15°S in the Upper Layer *(Figs. 1b,c*), where the AAIW tongue remains robust to the equator in the S-section profile, while ε_{Nd}-values are too negative (discussed in *Section 4.2.2*).

4. Discussion

4.1. Conservative and non-conservative behavior of ε_{Nd} and [Nd] in the SAMT

The salinity and ε_{Nd}-section profiles (*Fig. 1*) demonstrate the striking similarities between a conservative circulation tracer and Nd isotopes. Both the predicted ε_{Nd}-values of section profile from the OMPA (*Fig. 4b*) and the observations (*Figs. 1b, 4a*) strongly resemble the S-section profile (*Fig. 1b*), excepting the Upper Layer north of ~25ºS. A histogram of all of the below-pycnocline results (*Fig. S7*) shows that of the 198 samples measured, $\Delta\varepsilon_{Nd}$ has an average value of −0.3 ± 0.8 (1σ) ε_{Nd}-units, and a median value of −0.1 ε_{Nd}-unit; in 48% of samples, the measured and the OMPA predicted ε_{Nd}-values agree within typical measurement error (i.e., $\Delta\varepsilon_{Nd}$ = 0.0 ± 0.3), and 84% are within 3-times the typical measurement error (i.e., $\Delta\varepsilon_{Nd}$ = 0.0 ± 0.9) (*Fig. S7*). Additional insight can be gained by evaluating the data from the Lower, Middle, and Upper Layers separately; ε_{Nd}-values agree within the typical measurement error in 46%, 45%, and 54% of samples, respectively (*Figs. 6a,c,e*) fully 68%, 94%, and 82% of the samples, respectively, agree within 3-times the typical measurement error. This means that the vast majority of these data show near conservative mixing behavior. As the samples in the Upper, Middle, and Lower Layers range in ε_{Nd}-values from ~ −13 to −8, ~17 times the typical measurement error, the observed deviations are small compared to the range of ε_{Nd}-values in the dataset (*Figs. 5c, S1*).

This agreement between predicted and observed ε_{Nd}-values is particularly impressive considering that potential sources of external Nd near the transect show a large range of at least ~22 ε_{Nd}-units (*Fig. 5b*; ~73 times the analytical error), the large number of processes that can modify the seawater ε_{Nd}-values that have been discussed in the literature and listed in the introductory paragraph of this paper, and the uncertainties inherent in accurately predicting the

ε_{Nd}-values using the OMPA mixing model. The SAMT dataset clearly demonstrates that, with the exception of the northern region of the Upper Layer, the seawater ε_{Nd}-values in the intermediate to deep Southwest Atlantic Ocean can be effectively predicted by conservative isopycnal water mass mixing.

Insight into magnitudes and locations of the $\Delta\varepsilon_{Nd}$ deviations can be gained by evaluating the data from three depth layers separately. The largest ε_{Nd} deviations from conservative mixing (*Fig. 4c*) are near the pycnocline boundary of $\gamma^n = 27.1$ kg/m^3 in the Upper Layer north of ~26°S (Stations 11-18), where 14 samples (of 50 total Upper Layer samples) show negative $\Delta\varepsilon_{Nd}$ deviations of > 1 ε_{Nd}-unit (*Fig. 6b*). In the Lower Layer (*Fig. 6f*), only 3 of 50 measured samples deviate by more than 1.5 ε_{Nd}-units. Most of the samples with $\Delta\varepsilon_{Nd}$ deviations greater than 1 ε_{Nd}-unit are negative, and located north of 26°S (blue symbols in *Fig. 6f*). Based on limited marine sediment ε_{Nd} data between 26°S and the equator (*Fig. 5b*) (Robinson et al., 2021), we speculate that this reflects a contribution of a negative ε_{Nd} signature from the marine sediments to the bottom seawater in this region. In the Middle Layer (*Figs. 6c,d*), dominated by NADW, only 7 of 98 measured samples deviate more than 1 ε_{Nd}-unit, with no tendency to be too positive or too negative. These results show that the Middle Layer shows strongly conservative behavior, and that the leakage of Nd from above, observed in the Upper Layer in the northern part of the transect, does not extend to the Middle Layer.

Both measured and OMPA predicted Nd concentrations increase with increasing depth below the pycnocline at all stations (*Fig. S1*). Overall [Nd] is surprisingly conservative, as indicated by the similarity of the section profiles (*Figs. 4d,e*). Moreover, this accords with the results of a South Atlantic zonal transect (Zheng et al., 2016) where Nd and the other rare earth elements were shown to behave conservatively. In the SAMT, Figure 4f shows that [Nd] is within 10% of the predicted value over much of the transect. [Nd] shows enrichment > 10% in the north between ~12°S and the equator (Stations 15-18) in the Upper Layer, and between ~17°S and the equator (Stations 13-18) in the Lower Layer, and [Nd] shows depletions > 10% between ~50°S and ~10°S (Stations 1-15) in the Middle Layer.

4.2. Sources of external Nd to seawater and their impacts

The SAMT data show that external Nd added by eolian and shallow sources have major impacts on the Shallow Layer above the pycnocline, such that the ε_{Nd} variability of the surface waters is much larger (−18 to −7) than intermediate and deep water (−13 to −8) (*Figs. 5c, S1*). Below the pycnocline, the vast majority of samples show quasi-conservative mixing for Nd isotopes, with only about half the samples showing deviations outside of measurement error, and only a few showing substantial deviations. As summarized in the Section above, the deviations are mainly in the Upper Layer. Even there, 46% of measured samples are within measurement error of conservative mixing (*Fig. 6a*).

4.2.1. Sources of external Nd to the Shallow Layer

The SAMT offers the opportunity to investigate the sources of Nd to the Shallow Layer, which shows the most extreme range of ε_{Nd}-values from ~ −18 to ~ −7 (*Fig. 5b*); below the Shallow Layer the data are essentially bounded by the ε_{Nd}-values of the major AMOC water masses (*Fig. 5c*). There is a systematic increase of ε_{Nd}-values of terrigenous detritus, eolian dust, sediment and dust sources to the Southwest Atlantic from north to south that is mirrored by the Shallow Layer (*Fig. 5b*).

In the northern part of the transect from ~35°S to the equator, near surface seawater sample (25 and 100 m) (Stations 8-16) ε_{Nd}-values range from ~ −18 to ~ −11.5 (*Figs. 5b, S1*). This could reflect input of Nd from the nearby South American craton (ε_{Nd} ~ −17 to −8) or African-sourced eolian dust (ε_{Nd} ~ −19 to −8) brought to the region by the trade winds (*Figs. 5a,b*) (de Mahiques et al., 2008; Dia et al., 1990; Goldstein et al., 1984). South of ~35°S, the major source of terrigenous detritus is Patagonia. Interestingly, ε_{Nd}-values of the Shallow Layer waters of the southern Stations 1 to 7 (~ −11 to −7) are much more negative than Patagonian marginal marine sediments and Patagonian dusts (~ −4 to +4; *Fig. 5b*). A possible source of Nd with ε_{Nd}-values more negative than Patagonian sources is the Proterozoic age continent of the Malvinas/Falkland Plateau (Wareham et al., 1998). Another possible source of the negative ε_{Nd} signatures south of ~35°S may involve the interaction of the Malvinas and Brazil Currents. The northward flowing Malvinas Current has an estimated flux of ~45 Sv when it converges and mixes with the Brazil Current at the Brazil-Malvinas Confluence near the La Plata estuary (Maamaatuaiahutapu et al., 1998). Leakage of Brazil Current-sourced Nd with negative ε_{Nd}-values into the southward return flow of the Malvinas Current (*Figs. 1, S8*) may contribute to the offset from Patagonian detritus sources. It is noteworthy that there are a large number of Surface Layer samples that show ε_{Nd} ~ −10 over a large latitude range between ~20°-40°S (*Fig. 5b*), which may reflect mixing of the southern- and northern-derived Nd at the Confluence and dispersion by the return flow.

4.2.2. Sources of external Nd to the Upper Layer

As already noted, the largest ε_{Nd} deviations from conservative mixing (*Fig. 4c*) are near the boundary between the Shallow and Upper Layers, at 400-1000 m and between ~15-0°S. Their association at this boundary strongly indicates leakage of Nd from the Shallow to the Upper Layer, and the negative $\Delta\varepsilon_{Nd}$-values (*Figs. 4c, 6b*) indicate addition of continental Nd from sediments eroded from Brazil's Precambrian craton and/or eolian dust from the African craton carried by trade winds, both with low ε_{Nd}-values (de Mahiques et al., 2008; Dia et al., 1990; Goldstein et al., 1984) (*Figs. 5a,b*). Both sources are consistent with very negative ε_{Nd}-values observed in the most shallow samples (25-100 m) in Stations 13-18 (*Figs. 5a,b, S1*). This apparent addition of external Nd from detritus or eolian dust from the Shallow Layer to the Upper Layer contrasts with areas beneath the Saharan dust plume in the eastern North Atlantic, which do not show significant impacts of dust apart from the uppermost surface layer (Stichel et al., 2015; Zieringer et al., 2019). A possible explanation for the difference is that the SAMT samples that display the negative $\Delta\varepsilon_{Nd}$ anomaly are in a region where the ε_{Nd}-values of the shallow detritus input (< −15; *Fig. 5*) are markedly different from the AAIW and UCDW end-members (~ −8). Also notable is that these highly negative $\Delta\varepsilon_{Nd}$-values occur directly beneath a well-developed oxygen minimum zone (*OMZ*) (*Fig. S5c*), where regeneration of organic matter may release Nd back into seawater and locally alter the isotopic composition. This interpretation is further supported by positive Δ[Nd]-values, with 10-20% more Nd in solution than expected from water mass mixing (*Fig. 4f*).

4.2.3. Negligible impact from SAMT oceanic basalts to seawater Nd

Another potential source of external Nd is oceanic basalts, which could result in the addition of Nd with very high ε_{Nd}-values (e.g. Mid-Atlantic Ridge basalts have average ε_{Nd} of +8.6 ± 2.5

(Class and Lehnert, 2012), 1σ, n = 844). Along the SAMT, volcanic rocks from the Rio Grande Rise (RGR) and Vitória-Trindade Ridge (VTR) (*Fig. S9*) have ε_{Nd}-values of −3.7 ± 2.4 (1σ, n=10) and +2.9 ± 0.6 (1σ, n = 47), respectively (data are from EarthChem: www.earthchem.org/portal and data sources are listed in the *Supplementary Information Table S2*). In the SAMT, exchange or addition of Nd from the RGR (near Stations 9 and 10) and VTR (near Stations 12 and 13) can potentially influence the seawater ε_{Nd} signal, resulting in a positive $\Delta\varepsilon_{Nd}$ and possibly a positive Δ[Nd] downstream along the main water mass transport path after it bathes the volcanic RGR and VTR. The SAMT data near RGR and VTR show no discernible positive deviations of $\Delta\varepsilon_{Nd}$ and Δ[Nd] in the transect profiles (*Figs. 4c,f*), indicating negligible influence from the volcanics. A volcanic influence on regional seawater imparting more positive ε_{Nd} has been observed in the water column near the Cape Verde Islands (Stichel et al., 2015). The absence of more positive ε_{Nd} in the water column near the RGR and VTR may reflect the thicker sediments there compared to the Cape Verde Islands (Straume et al., 2019).

4.2.4. Sources of external Nd to the Lower Layer

Benthic nepheloid layers (*BNLs*) are a common feature in the deep water column with the potential to impact seawater ε_{Nd}-values. BNLs are characterized by high particle concentrations (Gardner et al., 2018) that potentially act as a source of external Nd through remobilization (e.g. Stichel et al., 2015), or as a sink through scavenging of Nd onto the remobilized particles. A recent study (Jaume-Seguí et al., 2020) ascribed possible impacts on deep seawater in the North Atlantic during deglaciations to BNLs. The SAMT cruise identified the presence of an extensive BNL between Stations 2-12 (~49° - ~22°S), as shown by beam attenuation (*Fig. S2*). Within the BNL, $\Delta\varepsilon_{Nd}$-values of the bottom water samples are close to 0 (*Figs. 4c, 6f*), interestingly in contrast to positive Δ[Nd] values elsewhere in the bottom water (*Fig. 4f*). The absence of a deviation from conservative water mass mixing within the BNL means that the resuspended particles in this case do not impact the bottom water ε_{Nd}-values.

Another potential source of external Nd to the bottom water is a benthic pore water flux (Abbott, 2019; Abbott et al., 2015; Haley et al., 2017). This process can be expected to cause positive $\Delta\varepsilon_{Nd}$ and Δ[Nd] values in the lower layer in the southern stations near Patagonia, and negative $\Delta\varepsilon_{Nd}$ and positive Δ[Nd] values in the northern stations (*Figs. 5a,b*). While $\Delta\varepsilon_{Nd}$-values of most Lower Layer samples are close to 0, there is a small tendency toward too low ε_{Nd}-values in the north, mainly within ~1 ε_{Nd}-unit but clearly skewed toward negative values – ε_{Nd}-values are mainly within 1 ε_{Nd}-unit that can be seen in the $\Delta\varepsilon_{Nd}$ section profile and the individual data (*Figs. 6e,f*), and positive Δ[Nd] values (*Fig. 4f*), that may reflect a flux of Nd with negative ε_{Nd}-values from the bottom sediment.

4.3. Comparison with other parts of the Atlantic Ocean

To put the SAMT results into a broader Atlantic basin-wide perspective, we compared our results with other published Atlantic data. Most of the intermediate and deep water ε_{Nd}-values from the SAMT are consistent with the published data, with some regional impacts on ε_{Nd} as discussed below.

4.3.1. Water mass end-member compositions in Atlantic water mass formation regions

The compositions of the AMOC water mass end-members in their formation regions were determined to evaluate how much they are modified between formation and transport to the SAMT region (shown in *Figs. 7, 8*). ε_{Nd} and [Nd] end-member values are defined from the published data of filtered seawater samples from the AMOC water mass formation regions (*WMFR*) in the western North Atlantic and the Southern Ocean. The data are from 17°N to 65°N for the North Atlantic water masses (Filippova et al., 2017; Hartman, 2015; Lacan and Jeandel, 2004, 2005a; Lambelet et al., 2016; Pahnke et al., 2012; Rickli et al., 2009; Shiller, 2021; Sholkovitz et al., 1994; Sholkovitz and Schneider, 1991; Stichel et al., 2018; van de Flierdt et al., 2012) and from 56°S to 67°S for the Southern Ocean water masses (Hathorne et al., 2015; Stichel et al., 2012).

The hydrographic properties of the AMOC water mass end-members are defined using World Ocean Atlas (WOA) 2018 (García et al., 2019a, b; Locarnini et al., 2019; Zweng et al., 2019). The WMFR end-member compositions (*Table 1b*) are defined based on the same hydrographic properties as the SAMT end-members, that is the S-minimum for AAIW, S-maximum for UNADW and LCDW, O_2-minimum for UCDW and MNADW, O_2-maximum for

LNADW, and the lowest θ-value for AABW. The corresponding ε_{Nd} and [Nd] data of these samples were used to define the end-member compositions.

Comparing the WMFR and SAMT end-member compositions, most of them are effectively the same, the only exceptions are AAIW and AABW (*Figs. 7b,c, 8b,c; Table 1*). In AAIW, the SAMT end-member has lower S than the WFMR end-member (a difference of ~0.1g/kg, compared to 0.01-0.04g/kg for the others), and slightly lower [Nd], but no significant change of the ε_{Nd}-value (~ −8), thus indicating some dilution with fresher water between the formation region and the SAMT. AABW is the only AMOC end-member that shows significant modification to the Nd-system between its formation region and the SAMT. The Southern Ocean end-member has more negative ε_{Nd} (−9.0 vs −8.0) and lower [Nd] (26.07 vs 36.99 pmol/g). This modification of AABW is most likely a consequence of its long flow path from the Southern Ocean to the Southwest Atlantic. The direct pathway is blocked at depth by the Malvinas/Falkland Plateau, and the AABW enters the Atlantic basin from the Southern Ocean east of South Georgia Island (Abrahamsen et al., 2019), and then travels nearly 2000 km westward along the Plateau's northern margin toward SAMT Stations 1 and 2. Along this path, Nd is added from the margins and/or the seafloor. The more positive ε_{Nd} of this input accords the characteristics of the detrital input to the Southwest Atlantic from Patagonia (*Figs. 5a,b*)

4.3.2. Comparison of SAMT ε_{Nd} and the rest of the Atlantic

The Southwest Atlantic is part of the broader AMOC, and in order to assess how the SAMT results fit in the basinal context, the intermediate and deep SAMT samples (> 100 m, θ < 6°C) are compared in θ-S and ε_{Nd}-S plots with the published data, separately for the South Atlantic and the Atlantic sector of the Southern Ocean (*Fig. 7*), and for the North Atlantic (*Fig. 8*). The comparison with the South Atlantic-Southern Ocean data highlights the evolution of the Southern Ocean water masses near their source regions, and NADW towards the end of its path within the Atlantic, and the comparison with the North Atlantic data highlights the source of NADW and the fate of the Southern Ocean water masses near their end path. The basinal context is also shown by meridional transects the western and eastern Atlantic basins for salinity and ε_{Nd} (*Figs. 9, S10*).

In the South Atlantic and Southern Ocean Atlantic sector, almost all of the published seawater ε_{Nd} data fall within the θ-S compositional range of the individual SAMT samples and mixing envelopes of the SAMT end-members, and all of the AMOC end-members are represented (*Fig. 7b*). With a few exceptions, this is also mainly the case for ε_{Nd}-S (*Fig. 7c*). The compositions of the published southwest Atlantic seawater samples coincide with SAMT, as do those from the south-central Atlantic crossing the Mid-Atlantic Ridge, and most samples from the southeast Atlantic (*Fig. 7c*, yellow triangles). The most important exception to this coherency is seen in some of the samples in the Angola Basin (*Fig. 7c*, black triangles) that show even more negative ε_{Nd}-values than the SAMT and WMFR end-members (Rahlf et al., 2020). This has been interpreted as resulting from partial dissolution of Fe-Mn oxides originating from surface waters and lateral transport of dissolved Nd originating from African shelf sediments (Rahlf et al., 2020; Zheng et al., 2016). Interestingly, the region affected by the highly negative ε_{Nd}-values is limited and concentrated between ~10-28°S along the transect (*Fig. S10c*), and it appears that these waters sampled in the central Angola Basin do not contribute significantly to the NADW wedge south of the Walvis Ridge, which show ε_{Nd}-values expected from its AMOC position. All of the other exceptions are from intermediate depths corresponding to the Upper Layer in the SAMT, which accords from our observations in the SAMT that this is the depth region that is most vulnerable to local modification: these are two samples at ~1000 and 1600 m (Garcia-Solsona et al., 2014) at ~50°S in the Southern Ocean, and two samples at ~1000 and 1200 m in the Cape Basin (Wang et al., 2021) (*Fig. 7c*).

The SAMT data are compared to North Atlantic intermediate and deep samples (below 1000 m) from ~45°N (*Fig. 8a*), where NADW is fully formed. Most of these North Atlantic samples lie close to the UNADW-MNADW-LNADW end-member mixing curve in θ-S space, with some extending toward AABW, and none show indications of contributions from AAIW, UCDW or LCDW (*Fig. 8b*). The general absence of Southern Ocean water mass contributions are reflected in the restricted range of North Atlantic ε_{Nd}-values; with few exceptions they fall within the restricted range of −14 to −11 (*Fig. 8c*). In the Northwest Atlantic, the formation region of NADW, they show a statistically small range of ε_{Nd}-values of −12.8 ± 0.7 (1σ, n = 129, this does not include the Caribbean samples), close to the WMFR values of the NADW water masses (−13.2, −12.6, and −12.2 for UNADW, MNADW and LNADW, respectively, *Table 1b*). The shallower samples from 1000-2000 m Atlantic (ε_{Nd} = −13.4 ± 0.6, 1σ, n = 40) show more negative ε_{Nd} than the deeper samples (ε_{Nd} = −12.6 ± 0.5, 1σ, n = 81), indicating contributions of Labrador Sea Water (Hartman, 2015; Lambelet et al., 2016). These are the samples that show more negative ε_{Nd} than the UNADW WMFR end-member in Figure 8c (brown squares). The tongue of Labrador Sea Water can also be observed in the western Atlantic transect (*Fig. 9c*). If 1000-2000 m Northwest Atlantic samples are excluded, the Northwest Atlantic ε_{Nd} for intermediate and deep water is −12.5 ± 0.6 (1σ, n = 86). Samples from outside of the NADW formation region show lower ε_{Nd}, with the Northeast Atlantic (ε_{Nd} = −11.7 ± 0.6, 1σ, n = 133) and the Central North Atlantic subtropical gyre (ε_{Nd} = −11.8 ± 0.5, 1σ, n = 33) showing essentially the same ε_{Nd}-values and small variability.

In contrast to the South Atlantic, many North Atlantic samples show θ-S values outside of the AMOC end-member mixing envelopes compared to the South Atlantic samples, towards both higher and lower S and higher θ (*Figs. 7b,8b*). Although the North Atlantic data set shows limited ε_{Nd} variability overall, this likely contributes to the small amount there is. For example, the only significant population of samples with ε_{Nd}-values more negative than the UNADW WMFR value are those from 1000-2000 m in the Northwest Atlantic, and these samples also tend to show lower salinity than the UNADW end-member (*Fig. 8c*, brown squares). Caribbean Sea seawater occupy a unique range of S-ε_{Nd}, showing typical North Atlantic salinity and high ε_{Nd} (−9.0 ± 1.7, 1σ, n = 14; *Fig. 8c*), reflecting its setting as a semi-enclosed basin isolated from the main Atlantic basin with young continent and volcanics that serve as sources of radiogenic Nd (Osborne et al., 2014; Pindell et al., 1991; Thompson et al., 2004). The highest salinity samples are those in the Northeast Atlantic near the Mediterranean Sea, in this case their ε_{Nd}-values of ~ −12 to −11 are typical for the Northeast Atlantic (*Figs. 8b,c, S10b,c*). Accounting for the characteristics of the Mediterranean Outflow (high salinity of ~38.5g/kg, ε_{Nd} ~ −9.4, [Nd] ~23 pmol/kg; Naranjo et al., 2017; Spivack and Wasserburg, 1988) shows that even the most saline North Atlantic sample has only ~10% of an Outflow component, and most have only a few percent.

Meridional ε_{Nd} and salinity transects are compared in the western and eastern Atlantic basins for all published data and the SAMT (*Figs. 9, S10*). In the western Atlantic basin the agreement is stunningly good for the AMOC water masses, with the exception of AAIW north of ~20°S (*Figs. 9b,c*). The extension of the transect into the northern hemisphere corroborates our findings that the AAIW salinity signal reaches north of the equator but the ε_{Nd}-signal disappears at ~20°S.

Compared to the western basin, the eastern Atlantic basin (*Fig. S10c*) shows similar ε_{Nd}-values for AAIW and AABW but some variations for the NADW. In the Northeast Atlantic (~20°N), ε_{Nd} is affected by radiogenic Nd from the Canary and Cape Verde Islands (Stichel et al., 2015; Zieringer et al., 2019). In the Southeast Atlantic (10-20°S), ε_{Nd} is influenced by partial dissolution of Fe-Mn oxides originating from surface waters in the Angola basin and less radiogenic Nd originating from sediments of the African shelf (Rahlf et al., 2020; Zheng et al., 2016) (*Fig. S10c*). The fewer regional impacts in the western Atlantic basin may reflect faster water mass advection there, allowing less opportunity for local effects.

5. Conclusions

Although recent studies have emphasized the probability of non-conservative behavior of ε_{Nd} in some areas of the oceans, analyses of dissolved ε_{Nd} in the GEOTRACES GA02 Southwest Atlantic Meridional Transect (SAMT) confirm its potential use as a "quasi-conservative" water mass tracer in intermediate and deep waters. Our evaluation of Nd isotopic deviations from predictions of conservative behavior using Optimum Multi-parameter Analysis to calculate the fractional water masses in each sample show that 48% of measured intermediate and deep samples associated with the AMOC water masses are within experimental error of predicted ε_{Nd}-values and 84% are within ± 0.9 ε_{Nd}-units (3-times the analytical error). Substantial non-conservative behavior is observed only in samples dominated by AAIW in the northern portion of the transect (~25°S to the equator). With the exception of this region, in the surface layer above the pycnocline, terrigenous sources of Nd locally modify ε_{Nd} but this signature is not transferred detectably into the deep-ocean. Benthic pore water fluxes may add Nd to the bottom waters in some locations where measured [Nd] is higher than predicted [Nd], however, in most instances the bottom water ε_{Nd}-values do not show deviations from conservative behavior, and in the SAMT deviations are observed only in the northern part of the transect. The presence of a benthic nepheloid layer in the southern part of the SAMT has no impact on the conservative behavior for ε_{Nd} and [Nd]. Major volcanic edifices in the SAMT associated with the Rio Grande Rise and Vitória-Trindade Ridge have no impact on conservative behavior of ε_{Nd}. This study confirms that, with some exceptions, ε_{Nd} effectively traces water mass mixing of the AMOC and can be used to reconstruct present and past changes of the AMOC, potentially providing valuable perspective to trace modern circulation, as well as to understand paleo-climate changes, as long as appropriate sites are chosen for study.

Acknowledgements

This study could not have been made without Captain Bill Richardson and the crew of the RRS James Cook Cruise JC057. We thank Arnold Gordon for discussions on the water mass pathways. Y.W. thanks Karla Knudson for help with editing the manuscript. Comments from anonymous reviewers helped to improve the paper and are much appreciated. L.P. acknowledges support from the Ramón y Cajal program and grant no. CTM2016-75411-R (MINECO, Spain). This study is mainly supported by U.S. NSF grant OCE-12-60514 to S.L.G., who also acknowledges support from the Storke Endowment of the Department of Earth and Environmental Sciences of Columbia University.

Author contributions

S.L.G. wrote the NSF proposal that primarily supported this study. Y.W., L.D.P., S.L.G., and R.F.A. designed the study. A.E.H. and L.D.P. participated in the cruise and collected the samples. Y.W. and L.D.P. processed samples for Nd isotopes. Y.W. and L.D.P. measured Nd isotopes with assistance from L.L.B. Y.W. processed samples and measured Nd concentrations with assistance from L.L.B. Y.W., L.D.P., S.L.G., R.F.A., C.B., and J.K. participated in data interpretation. L.L.B. kept the analytical instruments operating in top form. J.K. made significant contributions to revisions while Y.W. was on maternity leave. M.J.A.R. and H.J.W.d.B. were the Chief Scientist and the principal investigator of JC057, respectively. Y.W. was the main manuscript author, and all others contributed to revising and editing.

References

Abbott, A.N., 2019. A benthic flux from calcareous sediments results in non-conservative neodymium behavior during lateral transport: A study from the Tasman Sea. Geology 47, 363-366.

Abbott, A.N., Haley, B.A., McManus, J., 2015. Bottoms up: Sedimentary control of the deep North Pacific Ocean's εNd signature. Geology 43, 1035-1035.

Abbott, A.N., Löhr, S.C., Payne, A., Kumar, H., Du, J., 2022. Widespread lithogenic control of marine authigenic neodymium isotope records? Implications for paleoceanographic reconstructions. Geochimica et Cosmochimica Acta 319, 318-336.

Abrahamsen, E.P., Meijers, A.J.S., Polzin, K.L., Naveira Garabato, A.C., King, B.A., Firing, Y.L., Sallée, J.-B., Sheen, K.L., Gordon, A.L., Huber, B.A., Meredith, M.P., 2019. Stabilization of dense Antarctic water supply to the Atlantic Ocean overturning circulation. Nature Climate Change 9, 742-746.

Arsouze, T., Dutay, J.C., Lacan, F., Jeandel, C., 2007. Modeling the neodymium isotopic composition with a global ocean circulation model. Chemical Geology 239, 165-177.

Arsouze, T., Dutay, J.C., Lacan, F., Jeandel, C., 2009. Reconstructing the Nd oceanic cycle using a coupled dynamical – biogeochemical model. Biogeosciences 6, 2829-2846.

Basile, I., Grousset, F.E., Revel, M., Petit, J.R., Biscaye, P.E., Barkov, N.I., 1997. Patagonian origin of glacial dust deposited in East Antarctica (Vostok and Dome C) during glacial stages 2, 4 and 6. Earth and Planetary Science Letters 146, 573-589.

Bayon, G., Burton, K.W., Soulet, G., Vigier, N., Dennielou, B., Etoubleau, J., Ponzevera, E., German, C.R., Nesbitt, R.W., 2009. Hf and Nd isotopes in marine sediments: Constraints on global silicate weathering. Earth and Planetary Science Letters 277, 318-326.

Bayon, G., Skonieczny, C., Delvigne, C., Toucanne, S., Bermell, S., Ponzevera, E., André, L., 2016. Environmental Hf–Nd isotopic decoupling in World river clays. Earth and Planetary Science Letters 438, 25-36.

Behrens, M.K., Pahnke, K., Schnetger, B., Brumsack, H.-J., 2018. Sources and processes affecting the distribution of dissolved Nd isotopes and concentrations in the West Pacific. Geochimica et Cosmochimica Acta 222, 508-534.

Bouvier, A., Vervoort, J.D., Patchett, P.J., 2008. The Lu–Hf and Sm–Nd isotopic composition of CHUR: Constraints from unequilibrated chondrites and implications for the bulk composition of terrestrial planets. Earth and Planetary Science Letters 273, 48-57.

Broecker, W.S., Blanton, S., Smethie, W.M., Ostlund, G., 1991. Radiocarbon decay and oxygen utilization in the Deep Atlantic Ocean. Global Biogeochemical Cycles 5, 87-117.

Class, C., Lehnert, K., 2012. PetDB expert MORB (mid-ocean ridge basalt) compilation. EarthChem Library, 1-2.

de Mahiques, M.M., Tassinari, C.C.G., Marcolini, S., Violante, R.A., Figueira, R.C.L., da Silveira, I.C.A., Burone, L., e Sousa, S.H.d.M., 2008. Nd and Pb isotope signatures on the Southeastern South American upper margin: Implications for sediment transport and source rocks. Marine Geology 250, 51-63.

Dia, A., Allègre, C.J., Erlank, A.J., 1990. The development of continental crust through geological time: the South African case. Earth and Planetary Science Letters 98, 74-89.

Du, J., Haley, B.A., Mix, A.C., 2020. Evolution of the Global Overturning Circulation since the Last Glacial Maximum based on marine authigenic neodymium isotopes. Quaternary Science Reviews 241, 106396.

Elderfield, H., Whitfield, M., Burton, J.D., Bacon, M.P., Liss, P.S., Charnock, H., Lovelock, J.E., Liss, P.S., Whitfield, M., 1988. The oceanic chemistry of the rare-earth elements. Philosophical Transactions of the Royal Society of London. Series A, Mathematical and Physical Sciences 325, 105-126.

Filippova, A., Frank, M., Kienast, M., Rickli, J., Hathorne, E., Yashayaev, I.M., Pahnke, K., 2017. Water mass circulation and weathering inputs in the Labrador Sea based on coupled Hf–Nd isotope compositions and rare earth element distributions. Geochimica et Cosmochimica Acta 199, 164-184.

Frank, M., 2002. Radiogenic isotopes: tracers of past ocean circulation and erosional input. Reviews of geophysics 40.

Gaiero, D.M., Brunet, F., Probst, J.-L., Depetris, P.J., 2007. A uniform isotopic and chemical signature of dust exported from Patagonia: Rock sources and occurrence in southern environments. Chemical Geology 238, 107-120.

García, H.E., Weathers, K., Paver, C.R., Smolyar, I., Boyer, T.P., Locarnini, R.A., Zweng, M.M., Mishonov, A.V., Baranova, O.K., Seidov, D., Reagan, J.R., 2019a. World Ocean Atlas 2018, Volume 3: Dissolved Oxygen, Apparent Oxygen Utilization, and Dissolved Oxygen Saturation. NOAA Atlas NESDIS 83, 38 pp.

García, H.E., Weathers, K., Paver, C.R., Smolyar, I., Boyer, T.P., Locarnini, R.A., Zweng, M.M., Mishonov, A.V., Baranova, O.K., Seidov, D., Reagan, J.R., 2019b. World Ocean Atlas 2018. Volume 4: Dissolved Inorganic Nutrients (phosphate, nitrate and nitrate+ nitrite, silicate). NOAA Atlas NESDIS 84, 35 pp.

Garcia-Solsona, E., Jeandel, C., 2020. Balancing Rare Earth Element distributions in the Northwestern Mediterranean Sea. Chemical Geology 532, 119372.

Garcia-Solsona, E., Jeandel, C., Labatut, M., Lacan, F., Vance, D., Chavagnac, V., Pradoux, C., 2014. Rare earth elements and Nd isotopes tracing water mass mixing and particle-seawater interactions in the SE Atlantic. Geochimica et Cosmochimica Acta 125, 351-372.

Gardner, W.D., Richardson, M.J., Mishonov, A.V., 2018. Global assessment of benthic nepheloid layers and linkage with upper ocean dynamics. Earth and Planetary Science Letters 482, 126-134.

Gili, S., Gaiero, D.M., Goldstein, S.L., Chemale Jr, F., Jweda, J., Kaplan, M.R., Becchio, R.A., Koester, E., 2017. Glacial/interglacial changes of Southern Hemisphere wind circulation from the geochemistry of South American dust. Earth and Planetary Science Letters 469, 98-109.

Gili, S., Vanderstraeten, A., Chaput, A., King, J., Gaiero, D.M., Delmonte, B., Vallelonga, P., Formenti, P., Di Biagio, C., Cazanau, M., Pangui, E., Doussin, J.-F., Mattielli, N., 2022. South

African dust contribution to the high southern latitudes and East Antarctica during interglacial stages. Communications Earth & Environment 3, 129.

Goldstein, S.L., Hemming, S.R., 2003. Long-lived isotopic tracers in oceanography, paleoceanography, and ice-sheet dynamics. Treatise on geochemistry 6, 453-489.

Goldstein, S.L., O'Nions, R.K., Hamilton, P.J., 1984. A Sm-Nd isotopic study of atmospheric dusts and particulates from major river systems. Earth and planetary Science letters 70, 221-236.

Goldstein, S.L., O'Nions, R.K., 1981. Nd and Sr isotopic relationships in pelagic clays and ferromanganese deposits. Nature 292, 324.

Gruber, N., Sarmiento, J.L., 1997. Global patterns of marine nitrogen fixation and denitrification. Global Biogeochemical Cycles 11, 235-266.

Haley, B.A., Du, J., Abbott, A.N., McManus, J., 2017. The impact of benthic processes on rare Earth element and neodymium isotope distributions in the oceans. Frontiers in Marine Science 4, 426.

Hartman, A.E., 2015. The neodymium composition of Atlantic Ocean water masses: implications for the past and present. Columbia University, New York, NY.

Hathorne, E.C., Stichel, T., Brück, B., Frank, M., 2015. Rare earth element distribution in the Atlantic sector of the Southern Ocean: The balance between particle scavenging and vertical supply. Marine Chemistry 177, 157-171.

Hellerman, S., Rosenstein, M., 1983. Normal monthly wind stress over the world ocean with error estimates. Journal of Physical Oceanography 13, 1093-1104.

Henry, F., Probst, J.-L., Thouron, D., Depetris, P.J., Garçon, V., 1996. Nd-Sr isotopic compositions of dissolved and particulate material transported by the Parana and Uruguay rivers during high (december 1993) and low (september 1994) water periods. Sciences Géologiques, Bulletin 49, 89-100.

Höppner, N., Lucassen, F., Chiessi, C.M., Sawakuchi, A.O., Kasemann, S.A., 2018. Holocene provenance shift of suspended particulate matter in the Amazon River basin. Quaternary Science Reviews 190, 66-80.

Howe, J.N.W., Huang, K.-F., Oppo, D.W., Chiessi, C.M., Mulitza, S., Blusztajn, J., Piotrowski, A.M., 2018. Similar mid-depth Atlantic water mass provenance during the Last Glacial Maximum and Heinrich Stadial 1. Earth and Planetary Science Letters 490, 51-61.

Howe, J.N.W., Piotrowski, A.M., Rennie, V.C.F., 2016. Abyssal origin for the early Holocene pulse of unradiogenic neodymium isotopes in Atlantic seawater. Geology 44, 831-834.

Huang, K.-F., Oppo, D.W., Curry, W.B., 2014. Decreased influence of Antarctic intermediate water in the tropical Atlantic during North Atlantic cold events. Earth and Planetary Science Letters 389, 200-208.

Jacobsen, S.B., Wasserburg, G., 1980. Sm-Nd isotopic evolution of chondrites. Earth and Planetary Science Letters 50, 139-155.

Jaume-Seguí, M., Kim, J., Pena, L.D., Goldstein, S.L., Knudson, K.P., Yehudai, M., Hartman, A.E., Bolge, L., Ferretti, P., 2020. Distinguishing Glacial AMOC and Interglacial Non-AMOC Nd Isotopic Signals in the Deep Western Atlantic Over the Last 1 Myr. Paleoceanography and Paleoclimatology 36, e2020PA003877.

Jeandel, C., 1993. Concentration and isotopic composition of Nd in the South Atlantic Ocean. Earth and Planetary Science Letters 117, 581-591.

Jeandel, C., 2016. Overview of the mechanisms that could explain the 'Boundary Exchange' at the land–ocean contact. Philosophical Transactions of the Royal Society A: Mathematical, Physical and Engineering Sciences 374, 20150287.

Jeandel, C., Arsouze, T., Lacan, F., Techine, P., Dutay, J.-C., 2007. Isotopic Nd compositions and concentrations of the lithogenic inputs into the ocean: A compilation, with an emphasis on the margins. Chemical Geology 239, 156-164.

Johannesson, K.H., Burdige, D.J., 2007. Balancing the global oceanic neodymium budget: Evaluating the role of groundwater. Earth and Planetary Science Letters 253, 129-142.

Johannesson, K.H., Chevis, D.A., Burdige, D.J., Cable, J.E., Martin, J.B., Roy, M., 2011. Submarine groundwater discharge is an important net source of light and middle REEs to coastal waters of the Indian River Lagoon, Florida, USA. Geochimica et Cosmochimica Acta 75, 825-843.

Lacan, F., 2002. Masses d'eau des Mers Nordiques et de l'Atlantique Subarctique tracées par les isotopes du néodyme. Université Paul Sabatier-Toulouse III.

Lacan, F., Jeandel, C., 2004. Subpolar Mode Water formation traced by neodymium isotopic composition. Geophysical Research Letters 31.

Lacan, F., Jeandel, C., 2005a. Acquisition of the neodymium isotopic composition of the North Atlantic Deep Water. Geochemistry, Geophysics, Geosystems 6.

Lacan, F., Jeandel, C., 2005b. Neodymium isotopes as a new tool for quantifying exchange fluxes at the continent–ocean interface. Earth and Planetary Science Letters 232, 245-257.

Lambelet, M., van de Flierdt, T., Crocket, K., Rehkämper, M., Kreissig, K., Coles, B., Rijkenberg, M.J.A., Gerringa, L.J.A., de Baar, H.J.W., Steinfeldt, R., 2016. Neodymium isotopic composition and concentration in the western North Atlantic Ocean: Results from the GEOTRACES GA02 section. Geochimica et Cosmochimica Acta 177, 1-29.

Lantzsch, H., Hanebuth, T.J.J., Chiessi, C.M., Schwenk, T., Violante, R.A., 2014. The high-supply, current-dominated continental margin of southeastern South America during the late Quaternary. Quaternary Research 81, 339-354.

Locarnini, R.A., Mishonov, A.V., Baranova, O.K., Boyer, T.P., Zweng, M.M., García, H.E., Reagan, J.R., Seidov, D., Weathers, K., Paver, C.R., Smolyar, I., 2019. World Ocean Atlas 2018, Volume 1: Temperature. NOAA Atlas NESDIS 81, 52 pp.

Maamaatuaiahutapu, K., Garçon, V., Provost, C., Mercier, H., 1998. Transports of the Brazil and Malvinas Currents at their Confluence. Journal of Marine Research 56, 417-438.

Naranjo, C., García-Lafuente, J., Sammartino, S., Sánchez-Garrido, J.C., Sánchez-Leal, R., Jesús Bellanco, M., 2017. Recent changes (2004–2016) of temperature and salinity in the Mediterranean outflow. Geophysical Research Letters 44, 5665-5672.

Osborne, A.H., Haley, B.A., Hathorne, E.C., Flögel, S., Frank, M., 2014. Neodymium isotopes and concentrations in Caribbean seawater: Tracing water mass mixing and continental input in a semi-enclosed ocean basin. Earth and Planetary Science Letters 406, 174-186.

Pahnke, K., Goldstein, S.L., Hemming, S.R., 2008. Abrupt changes in Antarctic Intermediate Water circulation over the past 25,000 years. Nature Geoscience 1, 870-874.

Pahnke, K., van de Flierdt, T., Jones, K.M., Lambelet, M., Hemming, S.R., Goldstein, S.L., 2012. GEOTRACES intercalibration of neodymium isotopes and rare earth element concentrations in seawater and suspended particles. Part 2: Systematic tests and baseline profiles. Limnology and Oceanography: Methods 10, 252-269.

Pasquier, B., Hines, S.K.V., Liang, H., Wu, Y., Goldstein, S.L., John, S.G., 2022. GNOM v1.0: an optimized steady-state model of the modern marine neodymium cycle. Geosci. Model Dev. 15, 4625-4656.

Piepgras, D.J., Wasserburg, G.J., 1980. Neodymium isotopic variations in seawater. Earth and Planetary Science Letters 50, 128-138.

Piepgras, D.J., Wasserburg, G.J., 1982. Isotopic Composition of Neodymium in Waters from the Drake Passage. Science 217.

Piepgras, D.J., Wasserburg, G.J., 1987. Rare earth element transport in the western North Atlantic inferred from Nd isotopic observations. Geochimica et Cosmochimica Acta 51, 1257-1271.

Piepgras, D.J., Wasserburg, G.J., Dasch, E.J., 1979. The isotopic composition of Nd in different ocean masses. Earth and Planetary Science Letters 45, 223-236.

Pindell, J.L., Barrett, S.F., Dengo, G., Case, J.E., 1991. Geological evolution of the Caribbean region; A plate-tectonic perspective, The Caribbean Region. Geological Society of America, p. 0.

Poole, R., Tomczak, M., 1999. Optimum multiparameter analysis of the water mass structure in the Atlantic Ocean thermocline. Deep Sea Research Part I: Oceanographic Research Papers 46, 1895-1921.

Pöppelmeier, F., Blaser, P., Gutjahr, M., Süfke, F., Thornalley, D.J.R., Grützner, J., Jakob, K.A., Link, J.M., Szidat, S., Lippold, J., 2019. Influence of Ocean Circulation and Benthic Exchange on Deep Northwest Atlantic Nd Isotope Records During the Past 30,000 Years. Geochemistry, Geophysics, Geosystems 20, 4457-4469.

Pöppelmeier, F., Scheen, J., Blaser, P., Lippold, J., Gutjahr, M., Stocker, T.F., 2020. Influence of Elevated Nd Fluxes on the Northern Nd Isotope End Member of the Atlantic During the Early Holocene. Paleoceanography and Paleoclimatology 35, e2020PA003973.

Rae, J.W.B., Broecker, W., 2018. What fraction of the Pacific and Indian oceans' deep water is formed in the Southern Ocean? Biogeosciences 15, 3779-3794.

Rahlf, P., Hathorne, E., Laukert, G., Gutjahr, M., Weldeab, S., Frank, M., 2020. Tracing water mass mixing and continental inputs in the southeastern Atlantic Ocean with dissolved neodymium isotopes. Earth and Planetary Science Letters 530, 115944.

Rempfer, J., Stocker, T.F., Joos, F., Dutay, J.-C., Siddall, M., 2011. Modelling Nd-isotopes with a coarse resolution ocean circulation model: Sensitivities to model parameters and source/sink distributions. Geochimica et Cosmochimica Acta 75, 5927-5950.

Rickli, J., Frank, M., Halliday, A.N., 2009. The hafnium–neodymium isotopic composition of Atlantic seawater. Earth and Planetary Science Letters 280, 118-127.

Robinson, S., Ivanovic, R., van de Flierdt, T., Blanchet, C.L., Tachikawa, K., Martin, E.E., Cook, C.P., Williams, T., Gregoire, L., Plancherel, Y., Jeandel, C., Arsouze, T., 2021. Global continental and marine detrital εNd: An updated compilation for use in understanding marine Nd cycling. Chemical Geology 567, 120119.

Rousseau, T.C.C., Sonke, J.E., Chmeleff, J., van Beek, P., Souhaut, M., Boaventura, G., Seyler, P., Jeandel, C., 2015. Rapid neodymium release to marine waters from lithogenic sediments in the Amazon estuary. Nature Communications 6, 7592.

Shiller, A.M., 2021. Dissolved rare earth element (REE) concentrations from the GEOTRACES North Atlantic Transect (Section GA03) collected on the R/V Knorr cruises KN199-04, KN199-05, and KN204-01 during 2010 and 2011. Biological and Chemical Oceanography Data Management Office (BCO-DMO). (Version 2) Version Date 2021-07-28. 10.26008/1912/bco-dmo.651138.2.

Sholkovitz, E.R., Landing, W.M., Lewis, B.L., 1994. Ocean particle chemistry: The fractionation of rare earth elements between suspended particles and seawater. Geochimica et Cosmochimica Acta 58, 1567-1579.

Sholkovitz, E.R., Schneider, D.L., 1991. Cerium redox cycles and rare earth elements in the Sargasso Sea. Geochimica et Cosmochimica Acta 55, 2737-2743.

Siddall, M., Khatiwala, S., van de Flierdt, T., Jones, K., Goldstein, S.L., Hemming, S., Anderson, R.F., 2008. Towards explaining the Nd paradox using reversible scavenging in an ocean general circulation model. Earth and Planetary Science Letters 274, 448-461.

Spivack, A.J., Wasserburg, G.J., 1988. Neodymium isotopic composition of the Mediterranean outflow and the eastern North Atlantic. Geochimica et Cosmochimica Acta 52, 2767-2773.

Stichel, T., Frank, M., Rickli, J., Haley, B.A., 2012. The hafnium and neodymium isotope composition of seawater in the Atlantic sector of the Southern Ocean. Earth and Planetary Science Letters 317, 282-294.

Stichel, T., Hartman, A.E., Duggan, B., Goldstein, S.L., Scher, H., Pahnke, K., 2015. Separating biogeochemical cycling of neodymium from water mass mixing in the Eastern North Atlantic. Earth and Planetary Science Letters 412, 245-260.

Stichel, T., Pahnke, K., Duggan, B., Goldstein, S.L., Hartman, A.E., Paffrath, R., Scher, H.D., 2018. TAG Plume: Revisiting the Hydrothermal Neodymium Contribution to Seawater. Frontiers in Marine Science 5.

Stordal, M.C., Wasserburg, G.J., 1986. Neodymium isotopic study of Baffin Bay water: sources of REE from very old terranes. Earth and Planetary Science Letters 77, 259-272.

Straume, E.O., Gaina, C., Medvedev, S., Hochmuth, K., Gohl, K., Whittaker, J.M., Abdul Fattah, R., Doornenbal, J.C., Hopper, J.R., 2019. GlobSed: Updated Total Sediment Thickness in the World's Oceans. Geochemistry, Geophysics, Geosystems 20, 1756-1772.

Tachikawa, K., Arsouze, T., Bayon, G., Bory, A., Colin, C., Dutay, J.-C., Frank, N., Giraud, X., Gourlan, A.T., Jeandel, C., 2017. The large-scale evolution of neodymium isotopic composition in the global modern and Holocene ocean revealed from seawater and archive data. Chemical Geology 457, 131-148.

Tachikawa, K., Athias, V., Jeandel, C., 2003. Neodymium budget in the modern ocean and paleo-oceanographic implications. Journal of Geophysical Research: Oceans 108.

Tachikawa, K., Jeandel, C., Roy-Barman, M., 1999. A new approach to the Nd residence time in the ocean: the role of atmospheric inputs. Earth and Planetary Science Letters 170, 433-446.

Thompson, P.M.E., Kempton, P.D., White, R.V., Kerr, A.C., Tarney, J., Saunders, A.D., Fitton, J.G., McBirney, A., 2004. Hf–Nd isotope constraints on the origin of the Cretaceous Caribbean plateau and its relationship to the Galápagos plume. Earth and Planetary Science Letters 217, 59-75.

van de Flierdt, T., Griffiths, A.M., Lambelet, M., Little, S.H., Stichel, T., Wilson, D.J., 2016. Neodymium in the oceans: a global database, a regional comparison and implications for palaeoceanographic research. Phil. Trans. R. Soc. A 374, 20150293.

van de Flierdt, T., Pahnke, K., Amakawa, H., Andersson, P., Basak, C., Coles, B., Colin, C., Crocket, K., Frank, M., Frank, N., Goldstein, S.L., Goswami, V., Haley, B.A., Hathorne, E.C., Hemming, S.R., Henderson, G.M., Jeandel, C., Jones, K., Kreissig, K., Lacan, F., Lambelet, M., Martin, E.E., Newkirk, D.R., Obata, H., Pena, L., Piotrowski, A.M., Pradoux, C., Scher, H.D., Schöberg, H., Singh, S.K., Stichel, T., Tazoe, H., Vance, D., Yang, J., 2012. GEOTRACES intercalibration of neodymium isotopes and rare earth element concentrations in seawater and suspended particles. Part 1: reproducibility of results for the international intercomparison. Limnology and Oceanography: Methods 10, 234-251.

von Blanckenburg, F., 1999. Tracing past ocean circulation? Science 286, 1862-1863.

Wang, R., Clegg, J.A., Scott, P.M., Larkin, C.S., Deng, F., Thomas, A.L., Zheng, X.-Y., Piotrowski, A.M., 2021. Reversible scavenging and advection – Resolving the neodymium paradox in the South Atlantic. Geochimica et Cosmochimica Acta 314, 121-139.

Wareham, C.D., Pankhurst, R.J., Thomas, R.J., Storey, B.C., Grantham, G.H., Jacobs, J., Eglington, B.M., 1998. Pb, Nd, and Sr Isotope Mapping of Grenville-Age Crustal Provinces in Rodinia. The Journal of Geology 106, 647-660.

Wu, Y., Pena, L.D., Bolge, L.L., Goldstein, S.L., 2022. Depth profiles of seawater dissolved 143Nd/144Nd from RRS James Cook JC-57 in the southwest Atlantic, Punta Arenas (Chile) to Las Palmas (Spain), March 2011 (GEOTRACES-SWAT project). Biological and Chemical Oceanography Data Management Office (BCO-DMO). (Version 1) Version Date 2017-01-06. 10.26008/1912/bco-dmo.672203.1.

Zhang, Y., Chiessi, C.M., Mulitza, S., Zabel, M., Trindade, R.I.F., Hollanda, M.H.B.M., Dantas, E.L., Govin, A., Tiedemann, R., Wefer, G., 2015. Origin of increased terrigenous supply to the NE South American continental margin during Heinrich Stadial 1 and the Younger Dryas. Earth and Planetary Science Letters 432, 493-500.

Zheng, X.-Y., Plancherel, Y., Saito, M.A., Scott, P.M., Henderson, G.M., 2016. Rare earth elements (REEs) in the tropical South Atlantic and quantitative deconvolution of their non-conservative behavior. Geochimica et Cosmochimica Acta 177, 217-237.

Zieringer, M., Frank, M., Stumpf, R., Hathorne, E.C., 2019. The distribution of neodymium isotopes and concentrations in the eastern tropical North Atlantic. Chemical Geology 511, 265-278.

Zweng, M.M., Reagan, J.R., Seidov, D., Boyer, T.P., Locarnini, R.A., García, H.E., Mishonov, A.V., Baranova, O.K., Weathers, K., Paver, C.R., Smolyar, I., 2019. World Ocean Atlas 2018, Volume 2: Salinity. NOAA Atlas NESDIS 82, 50 pp.

Figure 1. Station locations, and salinity and ε_{Nd} section profiles of the GEOTRACES GA02 Southwest Atlantic Meridional Transect (*SAMT*). (a) Map of the Southwest Atlantic with the numbered SAMT stations (white dots). Main pathways for the surface Brazil Current and Malvinas Current are shown in white. The ε_{Nd} signature of different South America regions is adapted from Jeandel et al., 2007; Robinson et al., 2021. (b) Salinity (*S*) section profile with S-contours (black) and neutral density contours (γ^n, yellow). The Optimum Multiparameter Analysis (*OMPA*) was performed along three neutral density bands defining the Upper, Middle, and Lower Layers (γ^n = 27.1-27.7, 27.7-28.1, and > 28.1 kg/m^3, respectively) assuming isopycnal mixing. The water masses sourced in the north are Upper, Middle, and Lower North Atlantic Deep Water (*UNADW*, *MNADW*, *LNADW*, respectively); those sourced in the south are Antarctic Intermediate Water, Upper and Lower Circumpolar Deep Water, and Antarctic Bottom Water (*AAIW*, *UCDW*, *LCDW*, *AABW*, respectively). The Rio Grande Rise (*RGR*) and Vitória-Trindade Ridge (*VTR*) are labeled. (c) ε_{Nd}-section profile with ε_{Nd} contours, showing a striking resemblance to the S-section, except in the northern part of the Upper Layer, where AAIW continues to the equator in the S-profile but peters out in the ε_{Nd}-profile.

Figure 2. Neutral density (γ^n) versus other seawater parameters of SAMT samples and water mass end-members. (a) Salinity (*S*). (b) Potential temperature (θ). (c) Oxygen (O_2). (d) PO_4^*. (e) ε_{Nd}. (f) Nd concentration (*[Nd]*). The grey diamonds are SAMT water mass end-members and listed in *Table 1a*. The legend gives the Station numbers from 1 in the south to 18 near the equator.

Figure 3. Salinity (*S*), potential temperature (θ), and ε_{Nd}-values of SAMT samples (γ^n > 27.1 kg/m^3). (a) θ vs. S. (b) θ vs. ε_{Nd}. (c) ε_{Nd} vs. S. High-S NADW is characterized by low ε_{Nd} (−14 to −12). Low salinity AAIW and low-θ AABW are characterized by high ε_{Nd} (−9 to −8). UCDW and LCDW with relatively low O_2 concentration and high-S, respectively, in the southernmost stations are also characterized by high ε_{Nd} (−9 to −8). γ^n-isopycnals are shown in dashed curves. The OMPA water mass end-members are shown in grey diamonds. SAMT samples show systematic changes with latitude following red, grey, and blue curves from stations in the south to the equator. To a first order, seawater ε_{Nd}-values below the depths of AAIW reflect mixtures of the main water masses.

Figure 4. Section profiles of various Nd parameters: (a) measured ε_{Nd}, (b) predicted ε_{Nd}, (c) $\Delta\varepsilon_{Nd}$ (measured ε_{Nd} – predicted ε_{Nd}), (d) measured [Nd], (e) predicted [Nd], and (f) Δ[Nd] (measured [Nd] – predicted [Nd]). The measured ε_{Nd} and predicted ε_{Nd} sections resemble each other except in the northern part of section at AAIW depths, right beneath the O_2 minimum zone (*OMZ*), where low measured ε_{Nd}-values are observed. The bottom water shows that measured [Nd] values are higher than predicted values except in the benthic nepheloid layer (*BNL*).

Figure 5. ε_{Nd} of dust sources, marine sediments, river sediments, and SAMT surface and deep waters. (a) ε_{Nd} of surface water (25 m) from the SAMT (circles) and ε_{Nd} signature of regions of South American and Africa (adapted from Jeandel et al., 2007; Robinson et al., 2021). Black arrows indicate directions of the westerlies (~60-35°S) and trade winds (~35°S-0°) (Hellerman and Rosenstein, 1983); the dashed line is the approximate boundary. Surface water ε_{Nd}-values are higher in the south and lower in the north, consistent with sediments eroded from South America (~50°S-0°) and eolian dust input from Africa (~35°S-0°). (b) ε_{Nd} vs. latitude of

dust sources, marine sediments, and river sediments from South America and Africa (small grey symbols) and SAMT water in the top 100m (grey symbols with colored marker lines), and at South Atlantic Central Water (*SACW*) depths, ~250-500m (symbols in red, orange, yellow, and blue). ε_{Nd}-values of marginal sediments are highest near Patagonia, intermediate at the La Plata estuary to Southern Brazil, and most negative adjacent to the Precambrian cratons in the north. The shallow water ε_{Nd}-values show the same general geographic trend but are offset from the sediments to more negative values. The cause of this offset is discussed in the main text. Sediment symbols: Patagonia marine sediment, grey squares; Patagonia top soil and dust, black circles; Rio de La Plata, grey circles; Southern Brazil, grey triangles; Parnaíba and Sao Francisco Rivers, grey diamonds; Amazon River and French Guiana, grey crosses; South Africa, empty squares; Namibia dust, empty circles; Congo River, empty triangles. Sediment data sources: Basile et al., 1997; Bayon et al., 2009; Bayon et al., 2016; de Mahiques et al., 2008; Dia et al., 1990; Gaiero et al., 2007; Gili et al., 2017; Gili et al., 2022; Goldstein et al., 1984; Goldstein and O'Nions, 1981; Henry et al., 1996; Höppner et al., 2018; Howe et al., 2018; Howe et al., 2016; Lantzsch et al., 2014; Pahnke et al., 2008; Pöppelmeier et al., 2019; Rousseau et al., 2015; Zhang et al., 2015. (c) ε_{Nd} vs. depth of selected SAMT stations 3, 5, 11, 12, 13, 14, 16, 17, and 18. The shallow water ε_{Nd} varies from −18 to −7 (in the grey area). The intermediate and deep water ε_{Nd} varies from −13 to −8 (between grey dashed lines). These diagrams indicate that the shallow water ε_{Nd} signature is not transferred to intermediate and deep water.

Figure 6. OMPA results: histograms of $\Delta\varepsilon_{Nd}$ (measured ε_{Nd} – predicted ε_{Nd}) and predicted vs. measured ε_{Nd} in three neutral density bands. (a, b) γ^n = 27.1-27.7 kg/m^3, (c,d) γ^n = 27.7-28.1, (e,f) γ^n > 28.1. The solid 1:1 line represents equal measured to predicted ε_{Nd}. The diagonal lines represent equal $\Delta\varepsilon_{Nd}$ in 1 ε_{Nd}-unit intervals. The agreement between measured and predicted ε_{Nd}-values improves going down the water column.

Figure 7. SAMT samples compared with published South Atlantic and Southern Ocean Atlantic Sector data. (a) Map with sampling stations. (b) θ vs. S. (c) ε_{Nd} vs. S. Plotted samples are from > 1000m, θ < 6°C**.** Symbols: SAMT, grey diamonds; SE Atlantic from the Angola Basin, yellow triangles; other SE Atlantic, yellow triangles; South Central Atlantic, orange circles; SW Atlantic, red squares; SAMT end-members, large grey diamonds; water mass formation region end-members, large red and blue circles (southern- and northern-sourced water masses, respectively). Data sources: Garcia-Solsona et al., 2014; Jeandel, 1993; Rahlf et al., 2020; Rickli et al., 2009; Stichel et al., 2012; Wang et al., 2021.

Figure 8. SAMT samples compared with published North Atlantic data. (a) Map with sampling stations. (b) θ vs. S. (c) ε_{Nd} vs. S. The published data are from south of ~45°N, where NADW is fully formed. Plotted samples are from > 1000 m, θ < 6°C**.** Symbols: SAMT, grey diamonds; NE Atlantic, blue triangles; North Central Atlantic, navy blue circles; NW Atlantic, purple squares; NW Atlantic data at 1000-2000 m, brown squares; Caribbean Sea, black squares; SAMT end-members, large grey diamonds; water mass formation region end-members, large red and blue circles (southern- and northern-sourced water masses, respectively). Data sources: Hartman, 2015; Huang et al., 2014; Lacan, 2002; Lambelet et al., 2016; Osborne et al., 2014; Stichel et al., 2015; Zieringer et al., 2019.

Figure 9. Salinity and ε_{Nd} transects in the West Atlantic between 60°N-60°S. (a) Map. (b) S-

transect. (c) ε_{Nd} transect. The S- and ε_{Nd}-transects agree with each other very well with the exception of AAIW north of ~20°S. Data sources: Hartman, 2015; Lacan, 2002; Lacan and Jeandel, 2004, 2005a; Lambelet et al., 2016; Piepgras and Wasserburg, 1980, 1982, 1987; Stichel et al., 2012.

Figure 1.

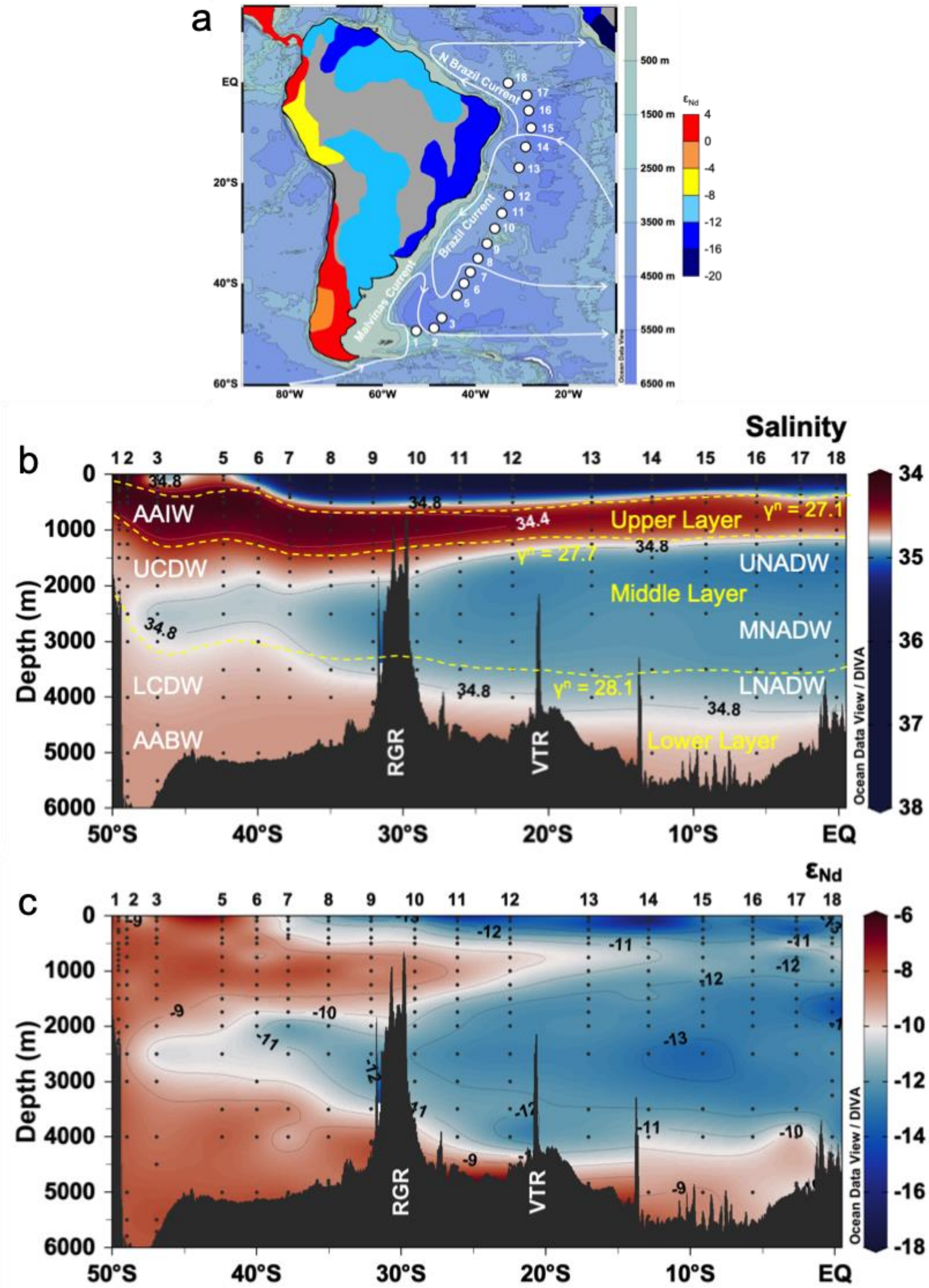
a
N Brazil Current
Brazil Current
Malvinas Current
EQ
20°S
40°S
60°S
80°W
60°W
40°W
20°W
500 m
1500 m
2500 m
3500 m
4500 m
5500 m
6500 m
ε_{Nd}
b
Salinity
Depth (m)
AAIW
UCDW
LCDW
AABW
Upper Layer
Middle Layer
Lower Layer
UNADW
MNADW
LNADW
$\gamma^n = 27.1$
$\gamma^n = 27.7$
$\gamma^n = 28.1$
RGR
VTR
50°S
40°S
30°S
20°S
10°S
EQ
Ocean Data View / DIVA
c
ε_{Nd}
Depth (m)
RGR
VTR
Ocean Data View / DIVA

Figure 2.

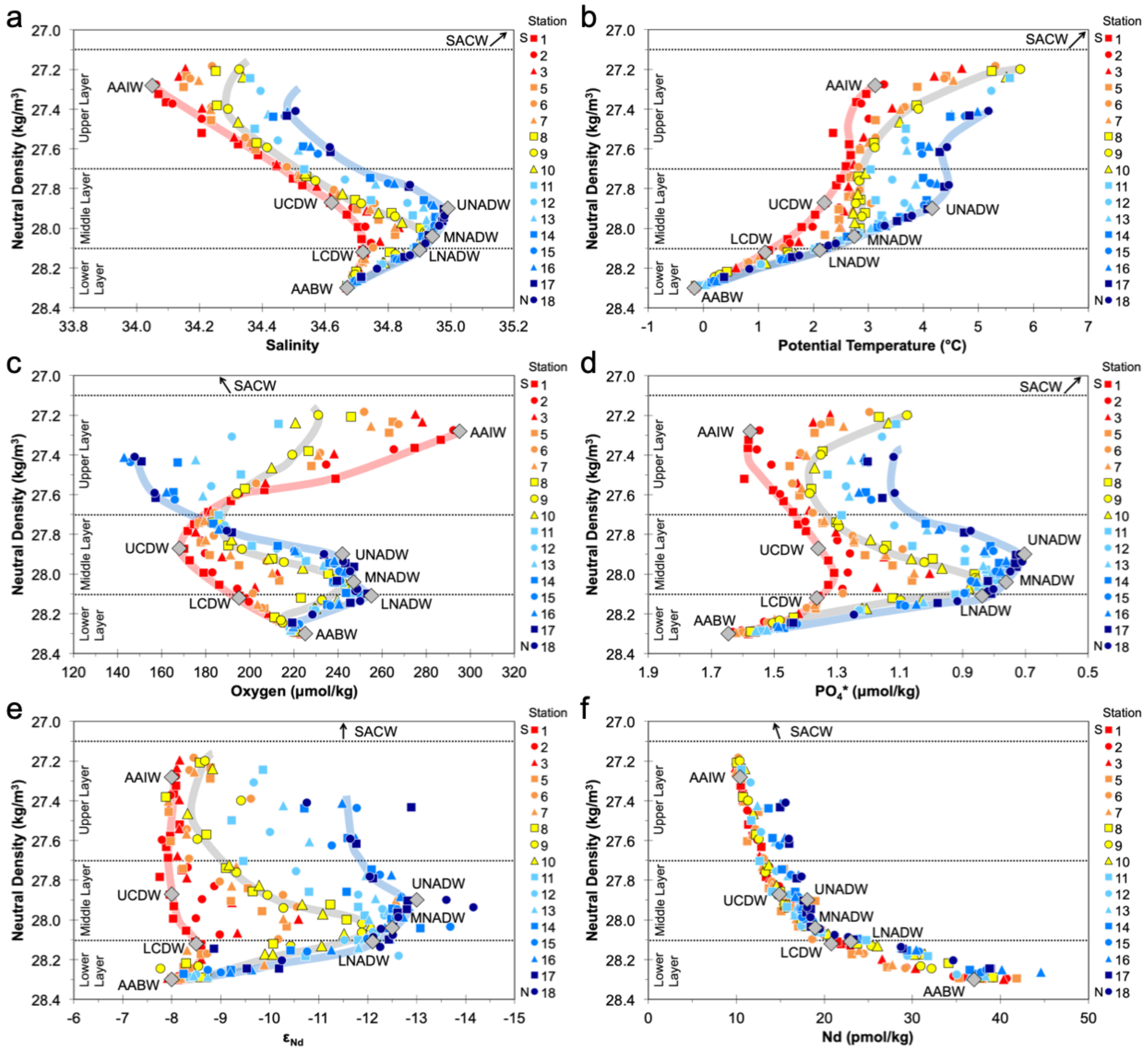
a
b
c
d
e
f
Station
S
N
1
2
3
5
6
7
8
9
10
11
12
13
14
15
16
17
18
SACW
AAIW
UCDW
LCDW
UNADW
MNADW
LNADW
AABW
Upper Layer
Middle Layer
Lower Layer
Neutral Density (kg/m³)
Salinity
Potential Temperature (°C)
Oxygen (µmol/kg)
PO4* (µmol/kg)
εNd
Nd (pmol/kg)

Figure 3.

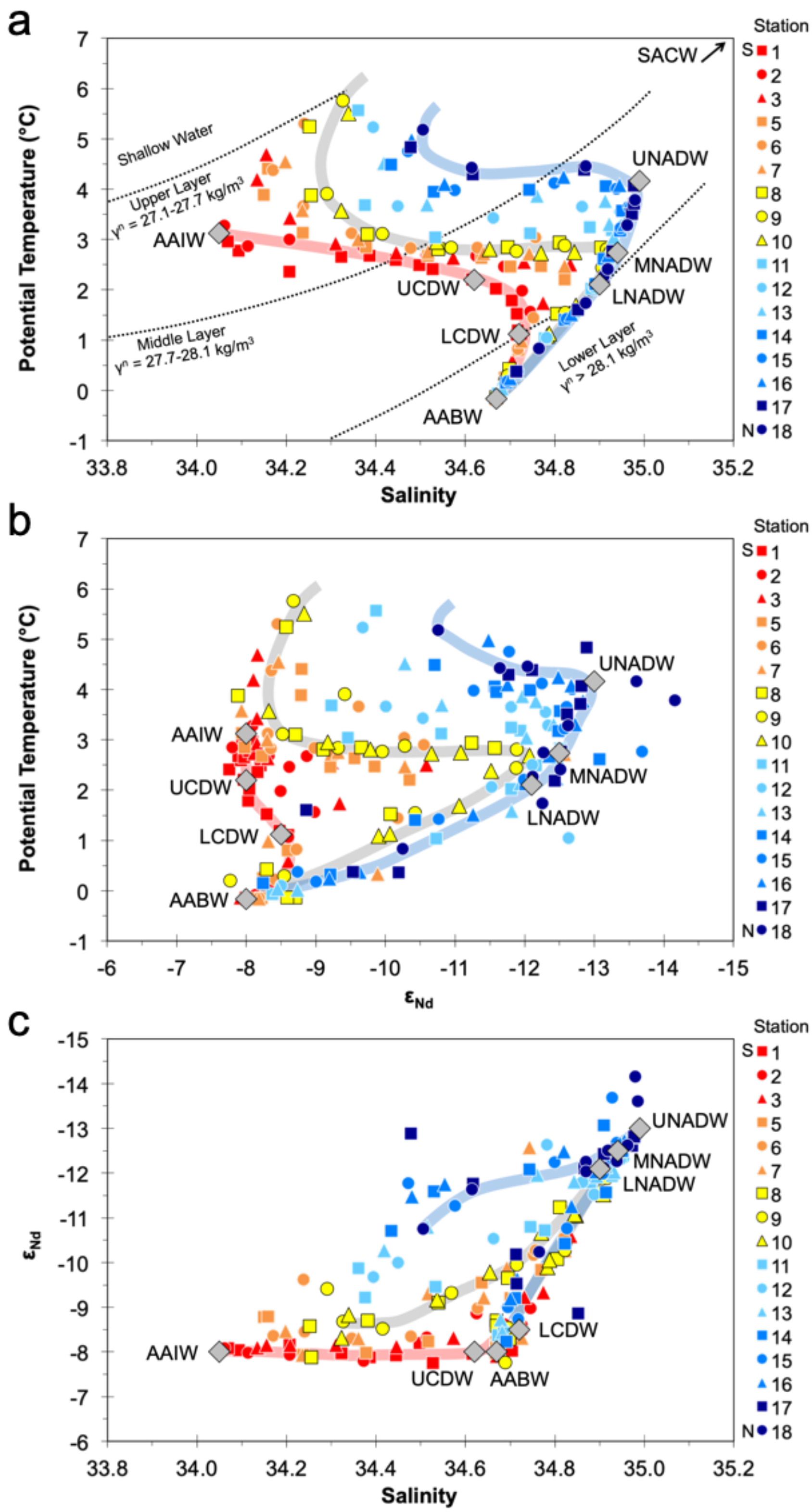
a
Potential Temperature (°C)
Salinity
Station
SACW
Shallow Water
Upper Layer
γⁿ = 27.1-27.7 kg/m³
Middle Layer
γⁿ = 27.7-28.1 kg/m³
Lower Layer
γⁿ > 28.1 kg/m³
AAIW
UCDW
LCDW
AABW
UNADW
MNADW
LNADW
b
Potential Temperature (°C)
εNd
Station
AAIW
UCDW
LCDW
AABW
UNADW
MNADW
LNADW
c
εNd
Salinity
Station
AAIW
UCDW
AABW
LCDW
UNADW
MNADW
LNADW
S
N
1
2
3
5
6
7
8
9
10
11
12
13
14
15
16
17
18

Figure 4.

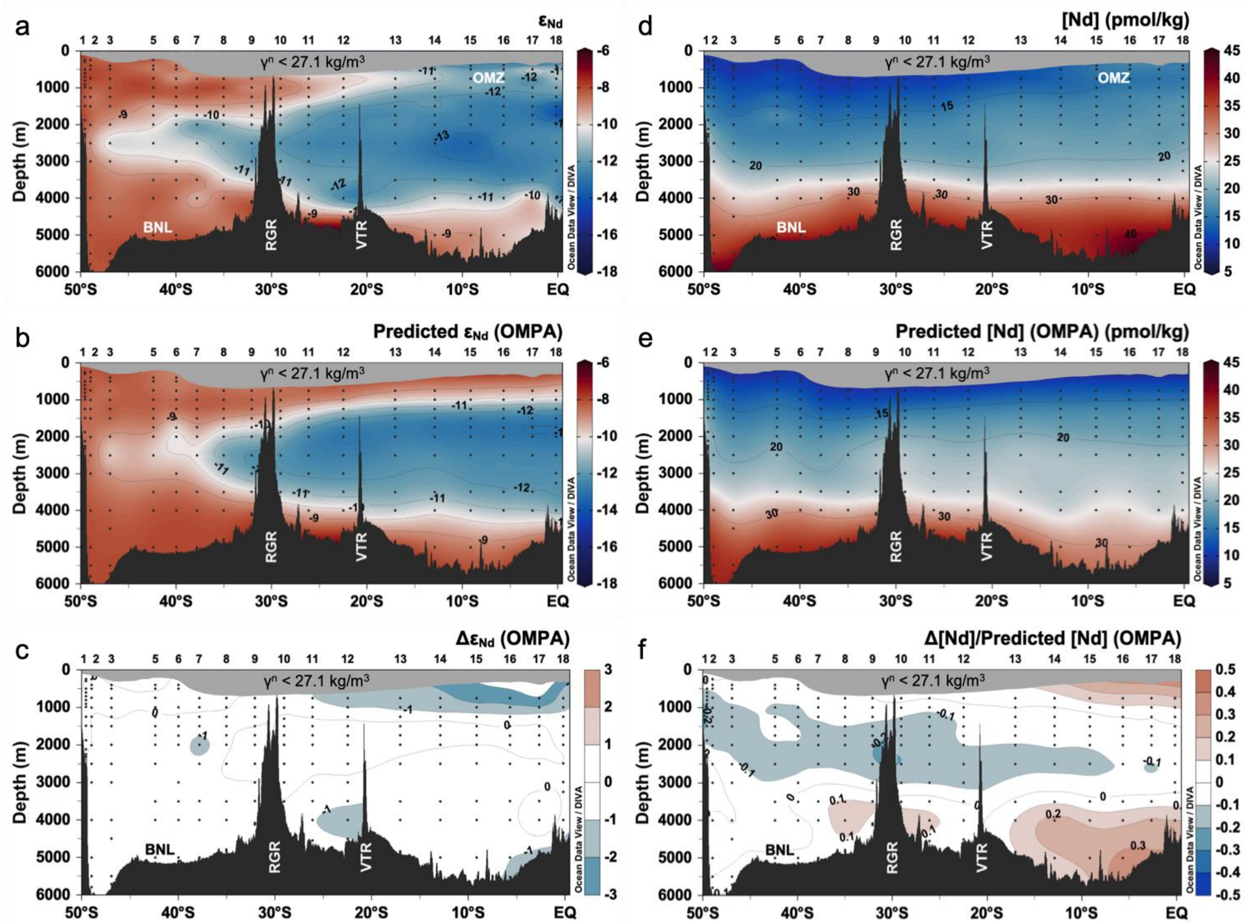
a
εNd
b
Predicted εNd (OMPA)
c
ΔεNd (OMPA)
d
[Nd] (pmol/kg)
e
Predicted [Nd] (OMPA) (pmol/kg)
f
Δ[Nd]/Predicted [Nd] (OMPA)
γn < 27.1 kg/m3
OMZ
BNL
RGR
VTR
Depth (m)
50°S
40°S
30°S
20°S
10°S
EQ
Ocean Data View / DIVA

Figure 5.

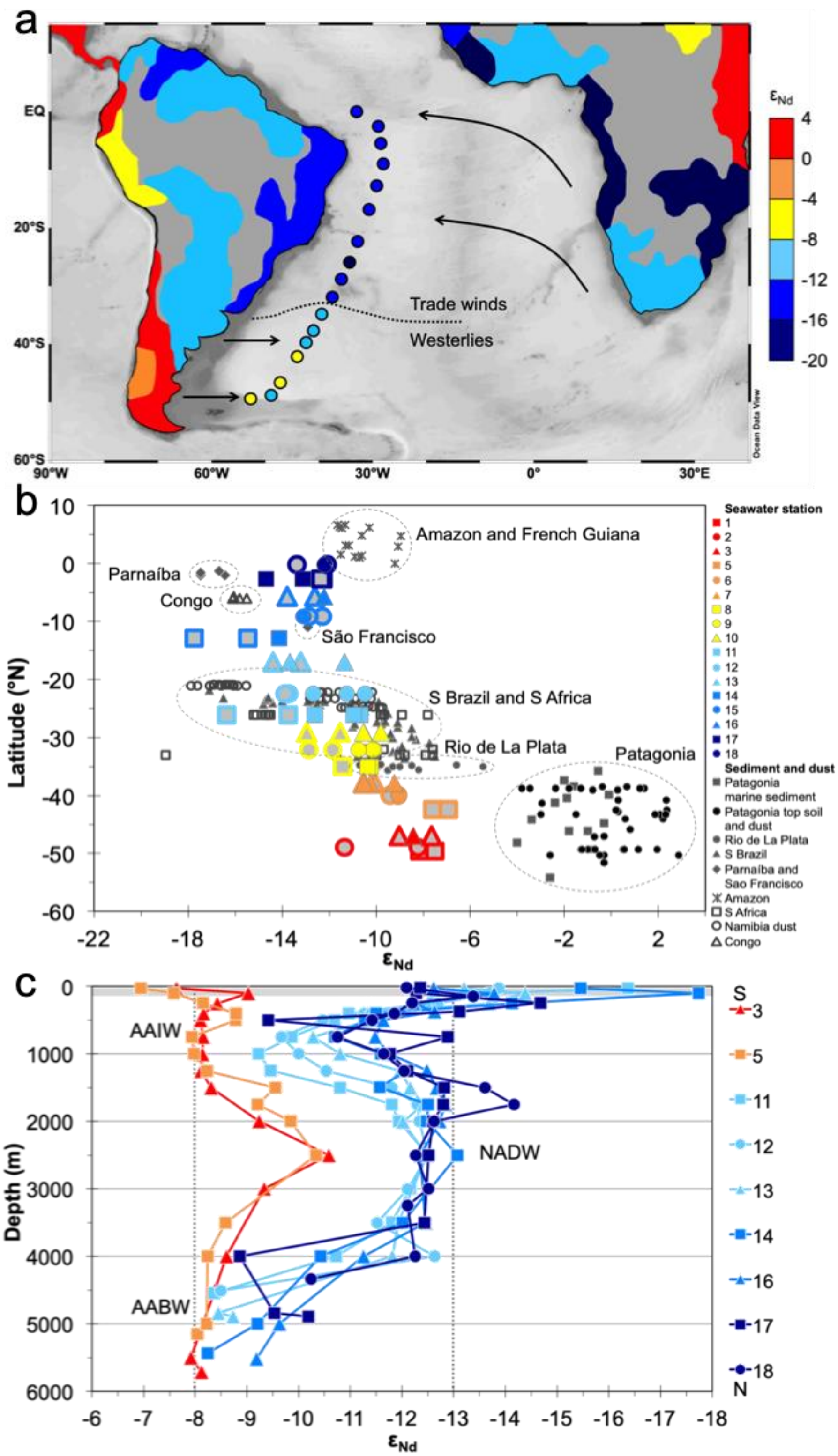
a
EQ
20°S
40°S
60°S
90°W
60°W
30°W
0°
30°E
Trade winds
Westerlies
Ocean Data View
εNd
4
0
-4
-8
-12
-16
-20
b
Amazon and French Guiana
Parnaíba
Congo
São Francisco
S Brazil and S Africa
Rio de La Plata
Patagonia
Latitude (°N)
εNd
Seawater station
Sediment and dust
Patagonia marine sediment
Patagonia top soil and dust
Rio de La Plata
S Brazil
Parnaíba and Sao Francisco
Amazon
S Africa
Namibia dust
Congo
c
AAIW
NADW
AABW
Depth (m)
εNd
S
N

Figure 6.

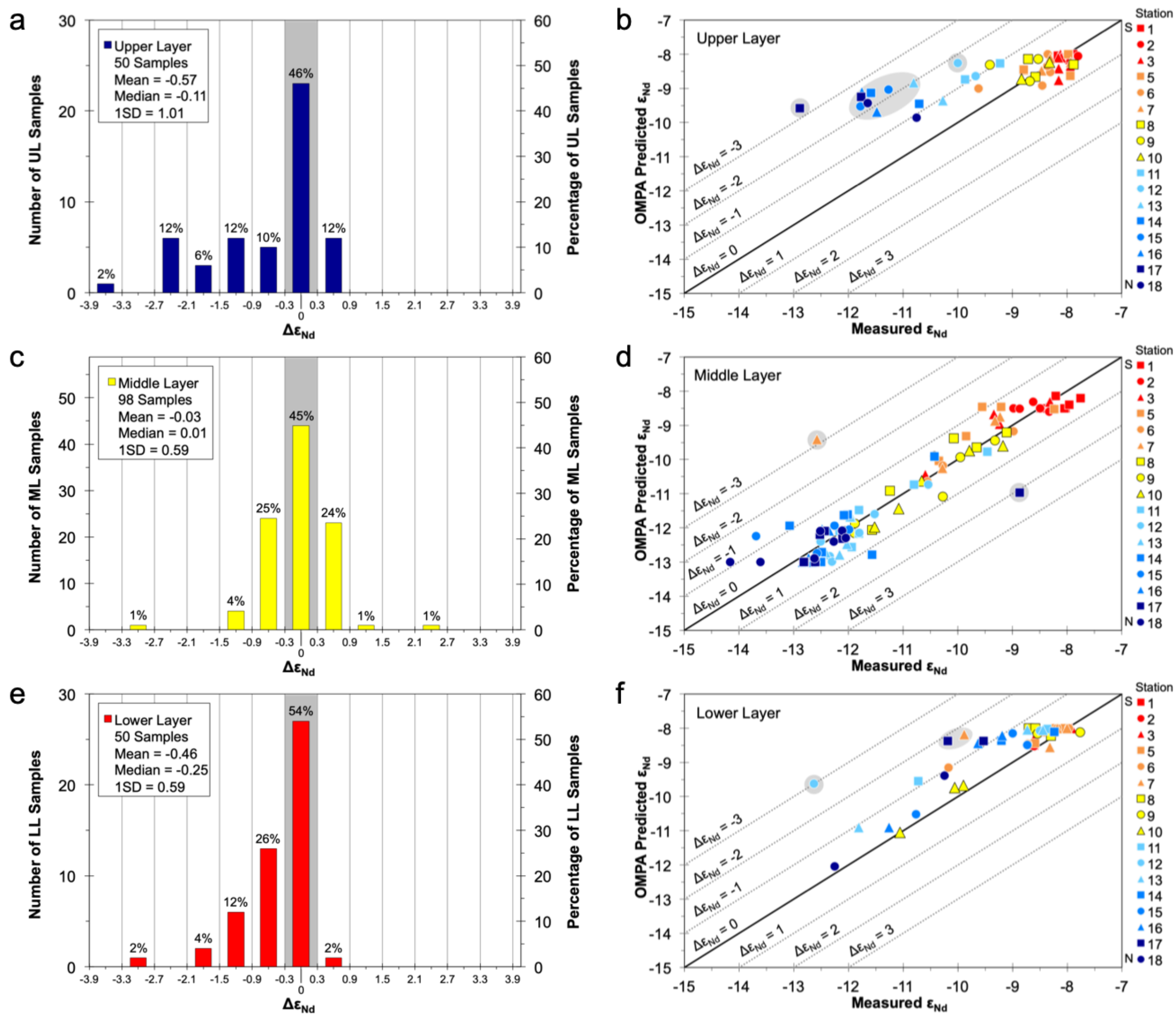
a
Upper Layer
50 Samples
Mean = -0.57
Median = -0.11
1SD = 1.01
Number of UL Samples
Percentage of UL Samples
2%
12%
6%
12%
10%
46%
12%
$\Delta\varepsilon_{Nd}$
b
Upper Layer
OMPA Predicted ε_{Nd}
Measured ε_{Nd}
Station
S
N
c
Middle Layer
98 Samples
Mean = -0.03
Median = 0.01
1SD = 0.59
Number of ML Samples
Percentage of ML Samples
1%
4%
25%
45%
24%
1%
1%
$\Delta\varepsilon_{Nd}$
d
Middle Layer
OMPA Predicted ε_{Nd}
Measured ε_{Nd}
e
Lower Layer
50 Samples
Mean = -0.46
Median = -0.25
1SD = 0.59
Number of LL Samples
Percentage of LL Samples
2%
4%
12%
26%
54%
2%
$\Delta\varepsilon_{Nd}$
f
Lower Layer
OMPA Predicted ε_{Nd}
Measured ε_{Nd}
$\Delta\varepsilon_{Nd}$ = -3
$\Delta\varepsilon_{Nd}$ = -2
$\Delta\varepsilon_{Nd}$ = -1
$\Delta\varepsilon_{Nd}$ = 0
$\Delta\varepsilon_{Nd}$ = 1
$\Delta\varepsilon_{Nd}$ = 2
$\Delta\varepsilon_{Nd}$ = 3

Figure 7.

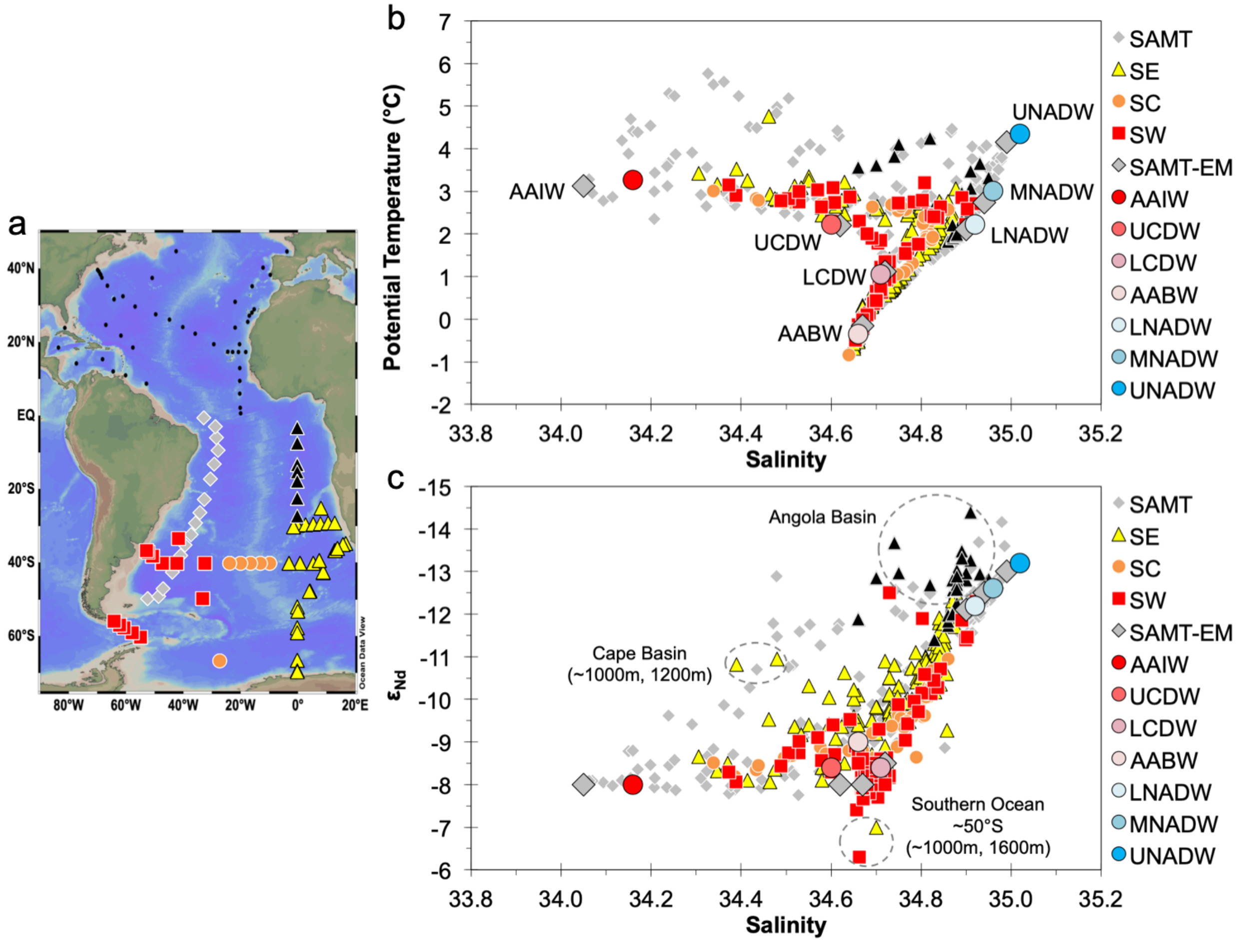
a
40°N
20°N
EQ
20°S
40°S
60°S
80°W
60°W
40°W
20°W
0°
20°E
Ocean Data View
b
Potential Temperature (°C)
Salinity
AAIW
UCDW
LCDW
AABW
UNADW
MNADW
LNADW
SAMT
SE
SC
SW
SAMT-EM
AAIW
UCDW
LCDW
AABW
LNADW
MNADW
UNADW
c
ε_{Nd}
Salinity
Angola Basin
Cape Basin
(~1000m, 1200m)
Southern Ocean
~50°S
(~1000m, 1600m)
SAMT
SE
SC
SW
SAMT-EM
AAIW
UCDW
LCDW
AABW
LNADW
MNADW
UNADW

Figure 8.

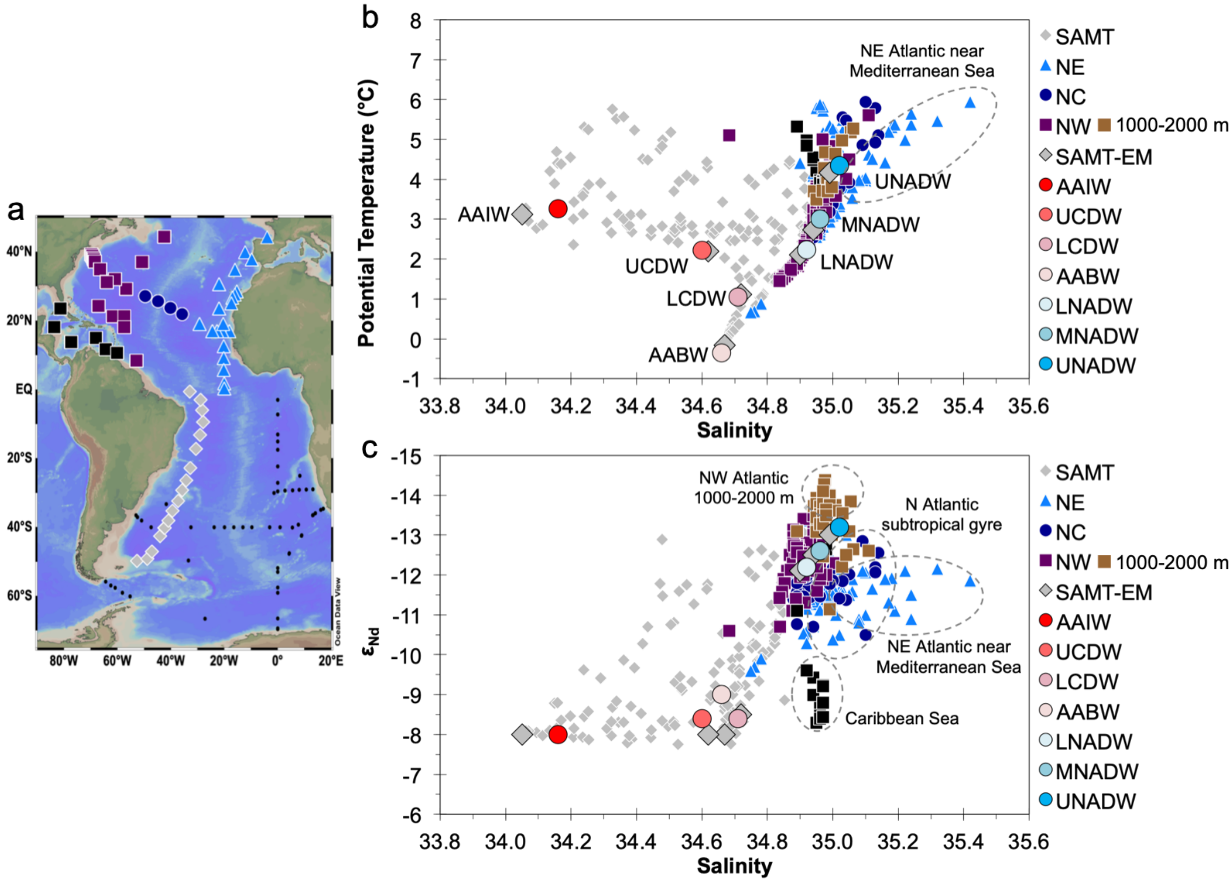
a
40°N
20°N
EQ
20°S
40°S
60°S
80°W
60°W
40°W
20°W
0°
20°E
Ocean Data View
b
Potential Temperature (°C)
Salinity
NE Atlantic near Mediterranean Sea
AAIW
UCDW
LCDW
AABW
UNADW
MNADW
LNADW
SAMT
NE
NC
NW
1000-2000 m
SAMT-EM
AAIW
UCDW
LCDW
AABW
LNADW
MNADW
UNADW
c
εNd
Salinity
NW Atlantic 1000-2000 m
N Atlantic subtropical gyre
NE Atlantic near Mediterranean Sea
Caribbean Sea
SAMT
NE
NC
NW
1000-2000 m
SAMT-EM
AAIW
UCDW
LCDW
AABW
LNADW
MNADW
UNADW

Figure 9.

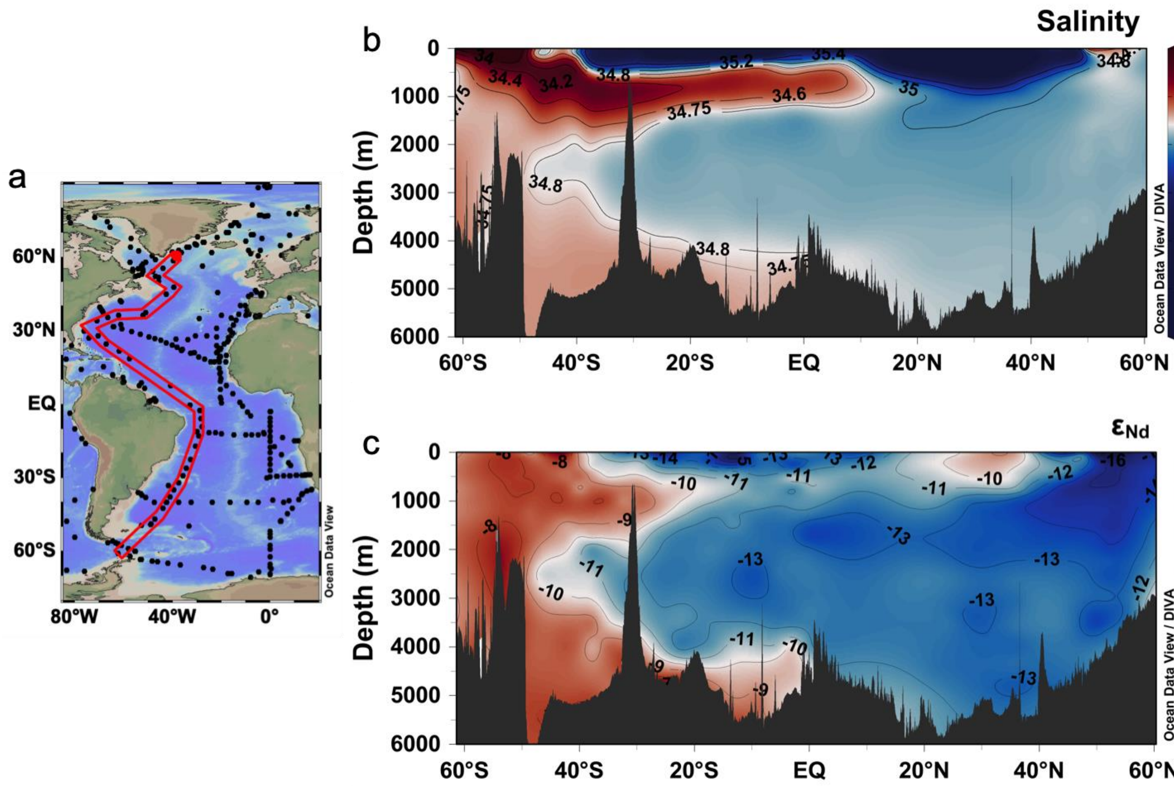
a
60°N
30°N
EQ
30°S
60°S
80°W
40°W
0°
Ocean Data View
b
Salinity
Depth (m)
0
1000
2000
3000
4000
5000
6000
60°S
40°S
20°S
EQ
20°N
40°N
60°N
34
34.5
35
35.5
36
36.5
37
Ocean Data View / DIVA
c
εNd
-6
-8
-10
-12
-14
-16
-18

Table 1. Water mass end-member compositions based on data from (a) the SAMT and (b) water mass formation regions.

	Salinity	Potential Temperature	Oxygen	PO_4^*	N^*	Silicate	ε_{Nd}	[Nd]
	g/kg	°C	µmol/kg	µmol/kg	µmol/kg	µmol/kg		pmol/kg
a) SAMT								
UNADW	34.99	4.16	242	0.70	2.03	16	−13.0	18.00
MNADW	34.94	2.74	247	0.76	1.87	27	−12.5	18.47
LNADW	34.90	2.11	255	0.84	1.11	32	−12.1	22.69
SACWn	35.16	12.30	186	0.12	1.22	5	−13.8	15.80
SACWs	35.16	12.30	186	0.12	1.22	5	−10.4	11.13
AAIW	34.05	3.12	295	1.58	0.36	15	−8.1	10.32
UCDW	34.62	2.20	168	1.36	−2.05	81	−8.0	14.85
LCDW	34.72	1.12	195	1.36	0.65	108	−8.5	21.45
AABW	34.67	−0.16	225	1.65	0.25	127	−8.0	36.99
b) WMFR								
UNADW	35.02	4.35	250	0.69	2.19	13	−13.2	17.49
MNADW	34.96	3.01	263	0.78	1.72	19	−12.6	18.27
LNADW	34.92	2.23	266	0.81	1.79	25	−12.2	23.63
AAIW	34.16	3.27	285	1.52	1.22	22	−8.0	10.79
UCDW	34.60	2.22	175	1.36	0.79	75	−8.4	13.94
LCDW	34.71	1.05	198	1.37	0.58	109	−8.4	22.50
AABW	34.66	−0.35	235	1.65	−0.22	122	−9.0	26.07

Table caption: (a) SAMT end-member compositions are determined from characteristics of this data set, and discussed in the Sections 2 and S1.3. (b) Determination of WMFR compositions is discussed in Section 4.3.1.

Supplementary Information for:

Assessing neodymium isotopes as an ocean circulation tracer in the Southwest Atlantic

Yingzhe Wu[a,b,*], Leopoldo D. Pena[a,c], Robert F. Anderson[a,b], Alison E. Hartman[d], Louise L. Bolge[a], Chandranath Basak[e], Joohee Kim[a,b], Micha J.A. Rijkenberg[f], Hein J.W. de Baar[f,g], Steven L. Goldstein[a,b]

[a] Lamont-Doherty Earth Observatory of Columbia University, Palisades, New York 10964, USA

[b] Department of Earth and Environmental Sciences, Columbia University, New York 10027, USA

[c] Departament de Dinàmica de la Terra i l'Oceà, Universitat de Barcelona, Martí i Franqués, 08028 Barcelona

[d] Department of Analytical Services, Agricultural Experiment Station Chemical Laboratories, University of Missouri, Columbia, MO 65211, USA

[e] Department of Earth Sciences, University of Delaware, Newark, DE 19716, USA

[f] Department of Ocean Systems, NIOZ Royal Netherlands Institute for Sea Research and Utrecht University, Den Burg, the Netherlands

[g] University of Groningen, Groningen, the Netherlands

S1. Methods

S1.1. Nd isotopes, sample preparation and analyses

A sub-sample of 50 mL was taken from each seawater sample for rare earth element (REE) concentration measurements (see Section S1.2). For the remaining 5-10 L of seawater, REEs were preconcentrated from each sample using C18 cartridges (Waters Corp., Sep-Pak classic, 360 mg, 55-105 μm) loaded with a complexing agent composed of a mixture of 2-ethylhexyl hydrogen phosphate (HDEHP) and 2-ethylhexyl dihydrogen phosphate (H_2MEHP) mixture (first proposed by Shabani et al., 1992). Our procedure is based on previously published methods (Jeandel et al., 1998; Lacan and Jeandel, 2001; Pahnke et al., 2012). C18 cartridges were first cleaned in a 0.5 N HCl bath overnight, then 10 mL of 6 N HCl was passed through them, and then they were flushed with > 500 mL of Milli-Q water. Cartridges were stored in Milli-Q water after cleaning. 300 μL of the complexing agent mixture was loaded on a clean cartridge for a 5 L sample. Seawater samples were adjusted to pH ≈ 3.5 by adding Optima® ammonium hydroxide before being pumped through the cartridges at 20 mL/min by a peristaltic pump in the ultra-clean chemistry laboratory at Lamont-Doherty Earth Observatory (LDEO) of Columbia University. Cartridges were then eluted with 10 mL of 0.01 N HCl to remove barium. After barium elution, cartridges were eluted with 35 mL of 6 N HCl at 10 mL/min by a peristaltic pump to collect REEs. The REEs were dried and further purified by Eichrom RE-spec® column chemistry. Nd fractions were extracted from REEs by LN-spec® column chemistry and dried. They were redissolved in 0.5-1 mL of 3% nitric acid (HNO_3) for Nd isotope analysis depending on the Nd amount in each sample (~3 to ~75 ng, ~19 ng on average). To determine the Nd amount in each sample, a small aliquot (1-2%) was taken from each sample and measured on a VG PlasmaQuad ExCell® quadrupole ICP-MS. Based on these Nd amounts, samples were divided in groups for Nd isotope analysis.

Nd isotope ratios were measured on a Thermo Scientific Neptune-Plus® multicollector-inductively coupled plasma-mass spectrometer (MC-ICP-MS) at LDEO. The instrument was coupled with an Elemental Scientific Inc. (ESI) Apex® desolvating nebulizer sample introduction system. All measured Nd isotopic compositions were corrected for mass fractionation using an exponential law with $^{146}Nd/^{144}Nd = 0.7219$. For each analytical session, standard JNdi-1 was measured between every sample. For each sample, the measured $^{143}Nd/^{144}Nd$ ratio was further normalized to $^{143}Nd/^{144}Nd_{JNdi}$ = 0.512115 (Tanaka et al., 2000), using the average measured JNdi-1 sample of a measuring session. For each group of samples with similar Nd amounts, JNdi-1 was measured at the same concentration as the samples. JNdi-1 standards yielded long-term external reproducibilities (2σ) as follows: ± 0.13 ε_{Nd} units for 40 ppb, ± 0.23 ε_{Nd} units for 20 ppb, ± 0.23 ε_{Nd} units for 15 ppb, and ± 0.43 ε_{Nd} units for 10 ppb samples. The $^{143}Nd/^{144}Nd$ ratios are expressed as ε_{Nd}, the deviation in parts per 10,000 from average chondrite, which is an estimate of the bulk Earth; this study uses $^{143}Nd/^{144}Nd$ = 0.512638 (Jacobsen and Wasserburg, 1980), in order to be consistent with decades of past data, rather than the updated value of 0.512630 (Bouvier et al., 2008); although the difference is small, only 0.16 ε_{Nd} units (and both values are within analytical error).

S1.2. Nd concentrations

For Nd concentrations, a multielement REE spike enriched in ^{138}La, ^{142}Ce, ^{145}Nd, ^{149}Sm, ^{153}Eu, ^{155}Gd, ^{161}Dy, ^{167}Er, ^{171}Yb, and ^{176}Lu (Wu et al., 2020) was added to each 10 ml-sized sample. The sample-spike mixture was allowed to equilibrate for at least 24 hours and then was purified and preconcentrated through an ESI seaFast® Automated Preconcentration System for Undiluted Seawater (Elemental Scientific Inc. or ESI, Omaha, Nebraska, USA) (Wu et al., 2020). The preconcentrated REEs were measured on a VG PlasmaQuad ExCell® quadrupole ICP-MS, which was coupled to a CETAC Aridus™ desolvating introduction system (that minimized molecular oxide ion formation with a self-aspirated ESI Apex ST PFA micro flow nebulizer. For quality control, we repeatedly analyze seawater samples from a GEOTRACES intercalibration station Bermuda Atlantic Time Series (BATS; 31.7°N, 64.1°W) in the North Atlantic at 20 m (n = 18) and 2000 m (n = 16) (Wu et al., 2020). For the BATS 20 and 2000 m samples, long-term external reproducibility (2σ RSD%) for Nd is 1.9% and 1.6%, respectively, using a two standard deviation filter on the data (Wu et al., 2020).

S1.3. Calculation of predicted Nd isotope ratios and concentrations

We defined the AMOC water mass end-member compositions before calculating fractional water mass contributions (*Figs. 2, S4*). We have used proximal end-member values (i.e., within the transect, from our set of data) to define water mass compositions because using the global end-member values would require accounting for potential mixing with other water masses and would be impacted by possible modifications to [Nd] along the transport path. Some of the Upper Layer samples had contributions from South Atlantic Central Water (*SACW*). The SACW end-member was defined using average values of samples in the Shallow Layer above the 27 kg/m^3 isopycnal, and below the pycnocline, since samples above the pycnocline have very large natural variability. For the intermediate and deep water (discussed in the text as the Upper, Middle, and Lower Layers that are part of the AMOC), the neutral densities were defined according to the hydrographic characteristics of each water mass as follows (*Fig. 2*): the salinity (*S*) minimum for AAIW, the dissolved oxygen (O_2) minimum for UCDW, the S-maximum for UNADW, the O_2-minimum for MNADW in the northernmost Stations 17 and 18, the O_2-maximum for LNADW in Stations 17 and 18, the S-maximum for LCDW in the southernmost Stations 1 and 2, and the lowest potential temperature (θ) for AABW. Then the values for the other parameters (S, θ, O_2, PO_4^*, N^*, and silicate (SiO_2) concentration) corresponding to the neutral densities of these water masses were used as end-member compositions (*Figs. 2, S4*). Here PO_4^* and N^* are the preformed phosphate ($\mathrm{PO}_4^* = \mathrm{PO}_4 + \mathrm{O}_2/175 - 1.95$) and nitrate ($\mathrm{N}^* = 0.87 * (\mathrm{NO}_3 - 16\mathrm{PO}_4 + 2.95)$) in the ocean, respectively, and are considered conservative water mass tracers (Broecker et al., 1991; Gruber and Sarmiento, 1997; Rae and Broecker, 2018). The values chosen for each end-member are listed in *Table 1a*. Section profiles of these tracers are shown in *Fig. S5*.

We used a modified version of Optimum Multiparameter Analysis (OMPA) (Poole and Tomczak, 1999) to identify the fractional contributions to each sample from the AMOC water masses. The method is a constrained non-negative least squares solution to the fraction of water masses for a given depth and location based on observed conservative hydrographic properties and the assignment of the “end-member” characteristics of each individual water mass. This prevents calculation of negative fractional water mass contributions. Given the relatively large number of water types present along the section we need to apply additional constraints to the calculation to over-determine the solution. For this purpose we use neutral density surfaces to break the analysis into three vertical domains that we call the Upper, Middle, and Lower Layers (γ^n = 27.1-27.7, γ^n = 27.7-28.1, and γ^n > 28.1 kg/m^3, respectively). Given the presence of a relatively intense O_2-minimum zone in the northern part of the Upper Layer, we decided to split this domain into two. In the northern part O_2 was not used as its behavior deviates from conservative mixing. The following equations were used in the OMPA:

$$\sum_{i=1}^{n} \mathrm{f}_i \times \mathrm{x}_i^j = \mathrm{x}$$

$$\sum_{i=1}^{n} \mathrm{f}_i = 1$$

where f_i is the fractional contribution (> 0) of water mass i, x_i^j is the value of water mass i for the tracer j, and x is the measured value. Because not all tracers are measured equally well, and because the defined end-member values also present some uncertainty, we need to weigh the equations differently, thereby adjusting the contribution of each tracer equation (and the conservation equation) to the least squares constraint. The weights for each tracer equation are calculated considering the deviation of property values from their average and the largest source water variance among the end-members, following Frants et al., 2013. Within reasonable limits, the exact choice of weights does not strongly affect the outcome (Jenkins et al., 2015). The weighting of the mass conservation equation denotes the degree to which the sum of the water type contributions may not be exactly 1. We chose a weighting factor of 500, that is, a constraint of 0.5% in the summation equation. Distributions of each intermediate and deep water mass are shown in section profiles (*Fig. S3*). For samples close to the boundary of the three vertical domains, we included them in both domains above and below the boundary in the OMPA. For example, samples at 1000 m north of Station 12 (γ^n = 27.56-27.62 kg/m^3, depending on location) were calculated in both upper and middle layers and samples within γ^n = 28.05-28.15 kg/m^3 (at ~2100 m to ~4000 m, depending on location) were calculated in both middle and lower layers.

After the fractional water mass contributions were calculated based on the OMPA, the predicted $\varepsilon_{\mathrm{Nd}}$ and Nd concentration [Nd] values were calculated as:

$$\varepsilon\mathrm{Nd}_{\mathrm{predicted}} = \frac{\sum_{i=1}^{n} \varepsilon\mathrm{Nd}_i \times [\mathrm{Nd}]_i \times \mathrm{f}_i}{\sum_{i=1}^{n} [\mathrm{Nd}]_i \times \mathrm{f}_i}$$

$$[\mathrm{Nd}]_{\mathrm{predicted}} = \sum_{i=1}^{n} [\mathrm{Nd}]_i \times \mathrm{f}_i$$

where $\varepsilon\mathrm{Nd}_i$, $[\mathrm{Nd}]_i$ and f_i are the Nd isotopic composition, Nd concentration, and mass fractional contribution of water mass i, respectively. The $\varepsilon_{\mathrm{Nd}}$ and [Nd] deviations were calculated as:

$$\Delta\varepsilon\mathrm{Nd} = \varepsilon\mathrm{Nd}_{\mathrm{measured}} - \varepsilon\mathrm{Nd}_{\mathrm{predicted}}, \text{ and } \Delta[\mathrm{Nd}] = [\mathrm{Nd}]_{\mathrm{measured}} - [\mathrm{Nd}]_{\mathrm{predicted}}.$$

Supplementary Figures

Figure S1. Vertical profiles of ε_{Nd} and [Nd] for each SAMT station.

Figure S2. Section profile of beam attenuation coefficient along the SAMT. High beam attenuation coefficient values indicate nepheloid layers with high particulate concentrations. The nepheloid layer in the SAMT is shown within 500 m of the seafloor from ~50°S to ~20°S.

Figure S3. Section profiles showing percentages of each intermediate and deep water mass. Results are from the OMPA, the water masses are AAIW, UCDW, LCDW, AABW, UNADW, and LNADW and residuals along the SAMT.

Figure S4. Neutral density (γ^n) plotted against N^* and silicate of samples and the water mass end-members from the SAMT. (a) N^*. (b) Silicate (SiO_2). The grey diamonds are water mass end-members defined from the SAMT and listed in *Table 1a*. The legend numbers are station numbers from Station 1 in the south to Station 18 at the equator.

Figure S5. Section profiles of tracers used in the OMPA. (a) Salinity (S). (b) Potential temperature (θ). (c) Dissolved oxygen (O_2). (d) PO_4^*. (e) N^*. (f) Silicate (SiO_2).

Figure S6. Potential temperature vs. salinity for SAMT samples. (a) All samples. (b) Data within the rectangle in (a), limited by $S < 34.5$g/kg, $\theta < 14$°C. Isopycnals of neutral density defining the Upper, Middle, and Lower Layers are shown in dashed curves. The grey diamonds are water mass end-members defined from the SAMT, listed in *Table 1a*, and used in the OMPA calculation.

Figure S7. Histogram of $\Delta\varepsilon_{Nd}$, based on the OMPA. $\Delta\varepsilon_{Nd}$ = (measured ε_{Nd} – predicted ε_{Nd}). The y-axis on the left is the number of calculated samples, and on the right is the percentage of calculated samples. $\Delta\varepsilon_{Nd}$-values are shown for the three neutral density layers (Upper Layer in blue, Middle in yellow, and Lower in red, explained in the text). Samples from the "Shallow Layer" above the pycnocline are not used. The numbers above the columns are percentage values within each interval.

Figure S8. The Malvinas and Brazil Currents, and the Brazil-Malvinas Confluence. As represented by the Mariano Global Surface Velocity Analysis (MGSVA) (Gyory et al., 2001-2013). Along with the main currents, the arrows also show northward and southward return flow.

Figure S9. Histograms of published ε_{Nd}-values for Rio Grande Rise and Vitório-Trindade Ridge volcanic rocks. (a) Rio Grande Rise (RGR); data are from Gibson et al., 2005; Hoernle et al., 2015. (b) Vitório-Trindade Ridge (VTR); data are from Bongiolo et al., 2015; Halliday et al., 1992; Kogarko et al., 2003; Marques et al., 1999; Peyve and Skolotnev, 2014; Siebel et al., 2000.

Figure S10. Salinity and ε_{Nd} transects in the East Atlantic. (a) Map showing available data, the transect used in (b) and (c) are outlined in red. (b) and (c) Salinity and ε_{Nd} transects. Published ε_{Nd} data are from Garcia-Solsona et al., 2014; Hartman, 2015; Jeandel, 1993; Rahlf et al., 2020; Rickli et al., 2009; Stichel et al., 2012; Stichel et al., 2015; Wang et al., 2021; Zieringer et al., 2019. The East Atlantic S- and ε_{Nd}-transects resemble each other, particularly in the far south boundary between the NADW wedge (generally blue) and the Southern Ocean waters (generally brown). Like the Upper Layer in the SAMT, the AAIW signal can be observed north of 30°S in the S-transect, but is not observed in the ε_{Nd}-transect. The effect of input from Nd sources with highly negative ε_{Nd}-values in the Angola Basin (Rahlf et al., 2020) is also clearly seen, mainly between the surface and ~3500 meters, along with the loss of that negative ε_{Nd}-signal south of ~30°S.

References

Bongiolo, E.M., Pires, G.L.C., Geraldes, M.C., Santos, A.C., Neumann, R., 2015. Geochemical modeling and Nd–Sr data links nephelinite–phonolite successions and xenoliths of Trindade Island (South Atlantic Ocean, Brazil). Journal of Volcanology and Geothermal Research 306, 58-73.

Bouvier, A., Vervoort, J.D., Patchett, P.J., 2008. The Lu–Hf and Sm–Nd isotopic composition of CHUR: Constraints from unequilibrated chondrites and implications for the bulk composition of terrestrial planets. Earth and Planetary Science Letters 273, 48-57.

Broecker, W.S., Blanton, S., Smethie, W.M., Ostlund, G., 1991. Radiocarbon decay and oxygen utilization in the Deep Atlantic Ocean. Global Biogeochemical Cycles 5, 87-117.

Frants, M., Gille, S.T., Hewes, C.D., Holm-Hansen, O., Kahru, M., Lombrozo, A., Measures, C.I., Mitchell, B.G., Wang, H., Zhou, M., 2013. Optimal multiparameter analysis of source water distributions in the Southern Drake Passage. Deep Sea Research Part II: Topical Studies in Oceanography 90, 31-42.

Garcia-Solsona, E., Jeandel, C., Labatut, M., Lacan, F., Vance, D., Chavagnac, V., Pradoux, C., 2014. Rare earth elements and Nd isotopes tracing water mass mixing and particle-seawater interactions in the SE Atlantic. Geochimica et Cosmochimica Acta 125, 351-372.

Gibson, S.A., Thompson, R.N., Day, J.A., Humphris, S.E., Dickin, A.P., 2005. Melt-generation processes associated with the Tristan mantle plume: Constraints on the origin of EM-1. Earth and Planetary Science Letters 237, 744-767.

Gruber, N., Sarmiento, J.L., 1997. Global patterns of marine nitrogen fixation and denitrification. Global Biogeochemical Cycles 11, 235-266.

Gyory, J., Mariano, A.J., Ryan, E.H., 2001-2013. “The Malvinas Current.” Ocean Surface Currents. https://oceancurrents.rsmas.miami.edu/atlantic/malvinas.html.

Halliday, A.N., Davies, G.R., Lee, D.-C., Tommasini, S., Paslick, C.R., Fitton, J.G., James, D.E., 1992. Lead isotope evidence for young trace element enrichment in the oceanic upper mantle. Nature 359, 623-627.

Hartman, A.E., 2015. The neodymium composition of Atlantic Ocean water masses: implications for the past and present. Columbia University, New York, NY.

Hoernle, K., Rohde, J., Hauff, F., Garbe-Schönberg, D., Homrighausen, S., Werner, R., Morgan, J.P., 2015. How and when plume zonation appeared during the 132 Myr evolution of the Tristan Hotspot. Nature Communications 6, 7799.

Jacobsen, S.B., Wasserburg, G., 1980. Sm-Nd isotopic evolution of chondrites. Earth and Planetary Science Letters 50, 139-155.

Jeandel, C., 1993. Concentration and isotopic composition of Nd in the South Atlantic Ocean. Earth and Planetary Science Letters 117, 581-591.

Jeandel, C., Thouron, D., Fieux, M., 1998. Concentrations and isotopic compositions of neodymium in the eastern Indian Ocean and Indonesian straits. Geochimica et Cosmochimica Acta 62, 2597-2607.

Jenkins, W., Smethie Jr, W., Boyle, E., Cutter, G., 2015. Water mass analysis for the US GEOTRACES (GA03) North Atlantic sections. Deep Sea Research Part II: Topical Studies in Oceanography 116, 6-20.

Kogarko, L., Levskii, L., Gushchina, N., 2003. Isotope sources of hot spots in the Trindade and Martin Vaz Islands, Southwestern Atlantic, Doklady earth sciences. Pleiades Publishing, Ltd.(Плеадес Паблишинг, Лтд), pp. 1116-1119.

Lacan, F., Jeandel, C., 2001. Tracing Papua New Guinea imprint on the central Equatorial Pacific Ocean using neodymium isotopic compositions and Rare Earth Element patterns. Earth and Planetary Science Letters 186, 497-512.

Marques, L.S., Ulbrich, M.N.C., Ruberti, E., Tassinari, C.G., 1999. Petrology, geochemistry and Sr–Nd isotopes of the Trindade and Martin Vaz volcanic rocks (Southern Atlantic Ocean). Journal of Volcanology and Geothermal Research 93, 191-216.

Pahnke, K., Van de Flierdt, T., Jones, K.M., Lambelet, M., Hemming, S.R., Goldstein, S.L., 2012. GEOTRACES intercalibration of neodymium isotopes and rare earth element concentrations in seawater and suspended particles. Part 2: Systematic tests and baseline profiles. Limnology and Oceanography: Methods 10, 252-269.

Peyve, A.A., Skolotnev, S.G., 2014. Systematic variations in the composition of volcanic rocks in tectono-magmatic seamount chaines in the Brazil Basin. Geochemistry International 52, 111-130.

Poole, R., Tomczak, M., 1999. Optimum multiparameter analysis of the water mass structure in the Atlantic Ocean thermocline. Deep Sea Research Part I: Oceanographic Research Papers 46, 1895-1921.

Rae, J.W.B., Broecker, W., 2018. What fraction of the Pacific and Indian oceans' deep water is formed in the Southern Ocean? Biogeosciences 15, 3779-3794.

Rahlf, P., Hathorne, E., Laukert, G., Gutjahr, M., Weldeab, S., Frank, M., 2020. Tracing water mass mixing and continental inputs in the southeastern Atlantic Ocean with dissolved neodymium isotopes. Earth and Planetary Science Letters 530, 115944.

Rickli, J., Frank, M., Halliday, A.N., 2009. The hafnium–neodymium isotopic composition of Atlantic seawater. Earth and Planetary Science Letters 280, 118-127.

Shabani, M.B., Akagi, T., Masuda, A., 1992. Preconcentration of trace rare-earth elements in seawater by complexation with bis (2-ethylhexyl) hydrogen phosphate and 2-ethylhexyl dihydrogen phosphate adsorbed on a C18 cartridge and determination by inductively coupled plasma mass spectrometry. Analytical Chemistry 64, 737-743.

Siebel, W., Becchio, R., Volker, F., Hansen, M.A.F., Viramonte, J., Trumbull, R.B., Haase, G., Zimmer, M., 2000. Trindade and Martín Vaz Islands, South Atlantic: Isotopic (Sr, Nd, Pb) and trace element constraints on plume related magmatism. Journal of South American Earth Sciences 13, 79-103.

Stichel, T., Frank, M., Rickli, J., Haley, B.A., 2012. The hafnium and neodymium isotope composition of seawater in the Atlantic sector of the Southern Ocean. Earth and Planetary Science Letters 317, 282-294.

Stichel, T., Hartman, A.E., Duggan, B., Goldstein, S.L., Scher, H., Pahnke, K., 2015. Separating biogeochemical cycling of neodymium from water mass mixing in the Eastern North Atlantic. Earth and Planetary Science Letters 412, 245-260.

Tanaka, T., Togashi, S., Kamioka, H., Amakawa, H., Kagami, H., Hamamoto, T., Yuhara, M., Orihashi, Y., Yoneda, S., Shimizu, H., 2000. JNdi-1: a neodymium isotopic reference in consistency with LaJolla neodymium. Chemical Geology 168, 279-281.

Wang, R., Clegg, J.A., Scott, P.M., Larkin, C.S., Deng, F., Thomas, A.L., Zheng, X.-Y., Piotrowski, A.M., 2021. Reversible scavenging and advection – Resolving the neodymium paradox in the South Atlantic. Geochimica et Cosmochimica Acta 314, 121-139.

Wu, Y., Pena, L.D., Goldstein, S.L., Basak, C., Bolge, L.L., Jones, K.M., McDaniel, D.K., Hemming, S.R., 2020. A User-Friendly Workbook to Facilitate Rapid and Accurate Rare Earth Element Analyses by ICP-MS for Multispiked Samples. Geochemistry, Geophysics, Geosystems 21, e2020GC009042.

Zieringer, M., Frank, M., Stumpf, R., Hathorne, E.C., 2019. The distribution of neodymium isotopes and concentrations in the eastern tropical North Atlantic. Chemical Geology 511, 265-278.

Figure S1.

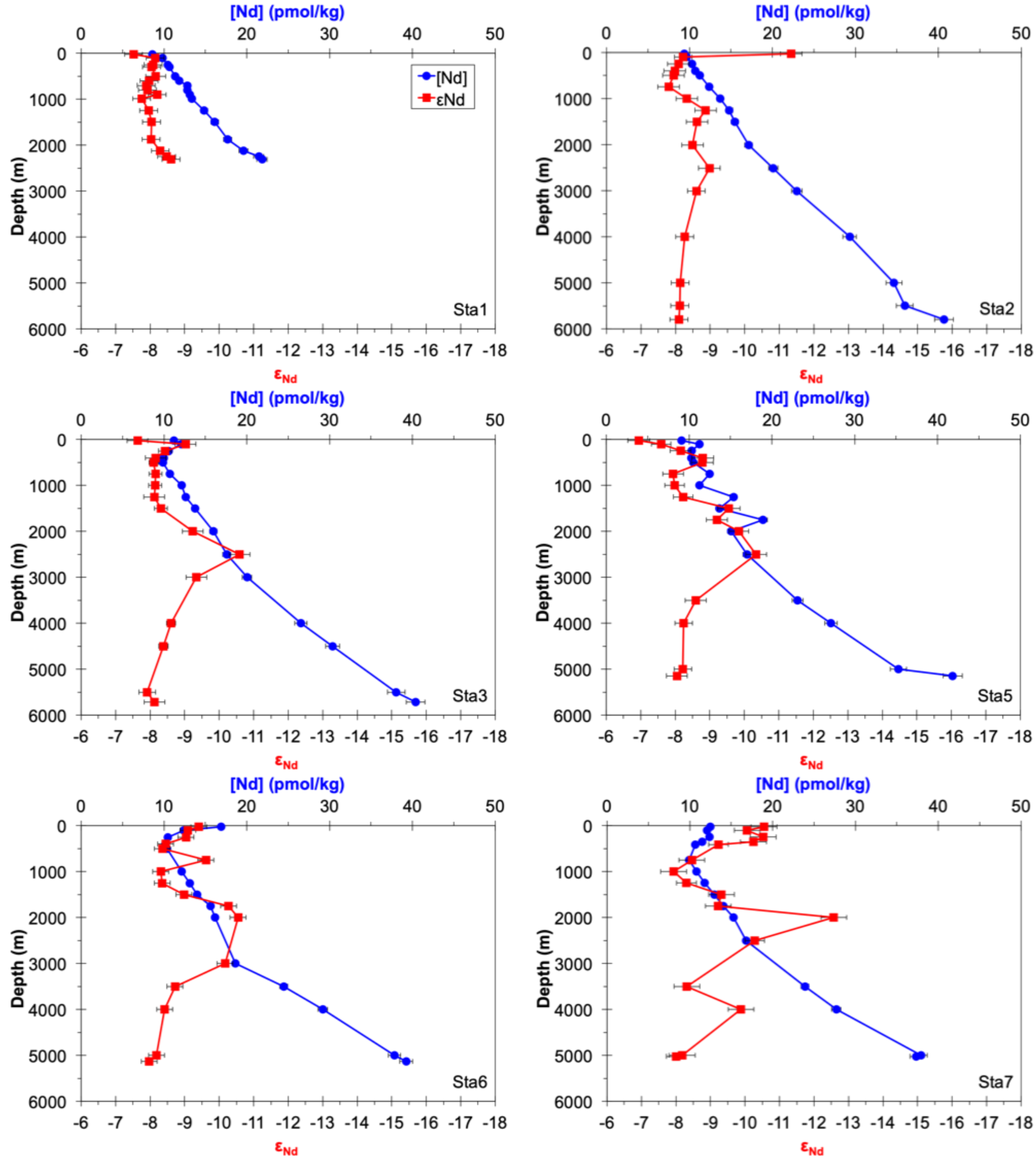

Figure S1. Continued

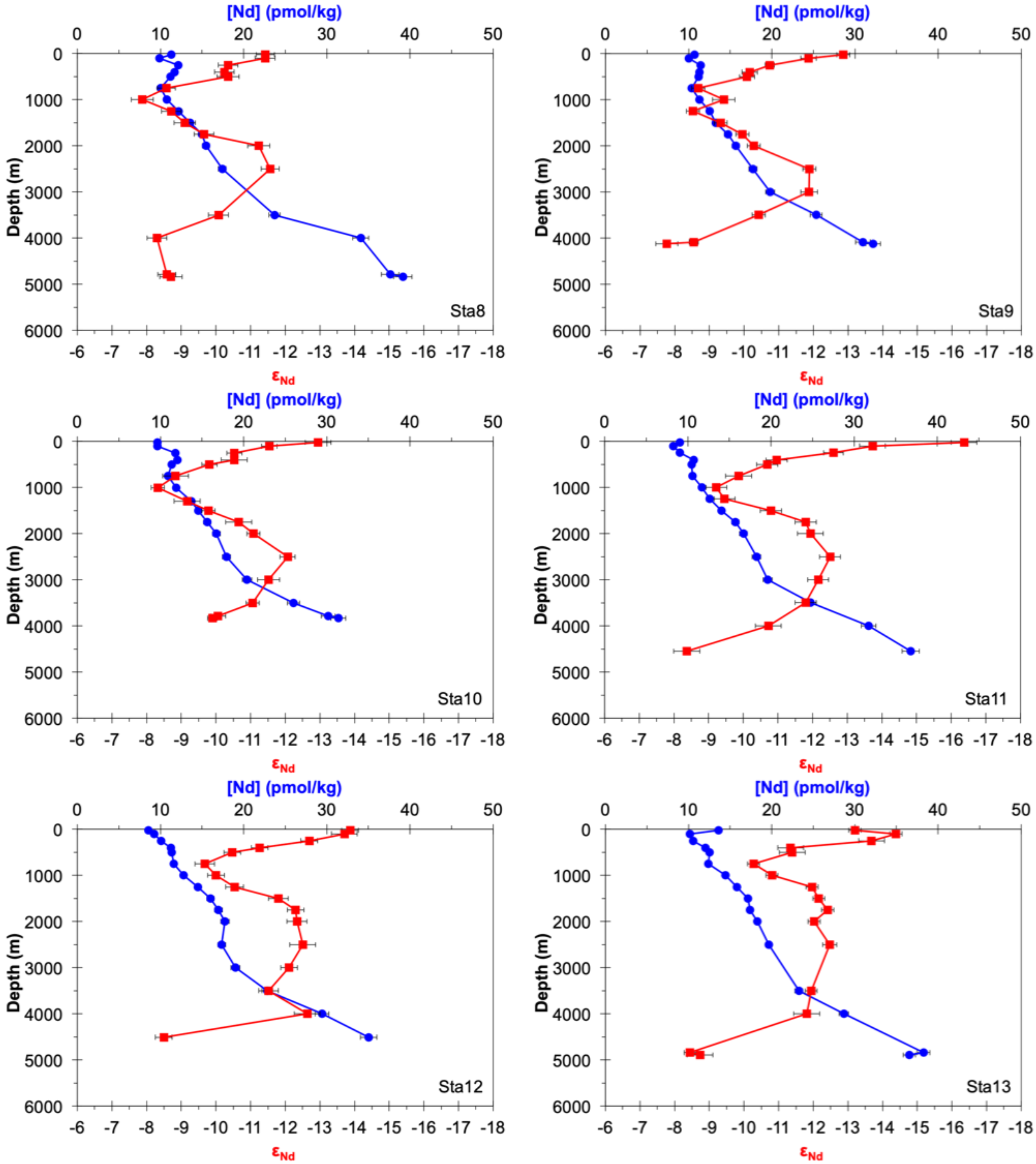

Figure S1. Continued

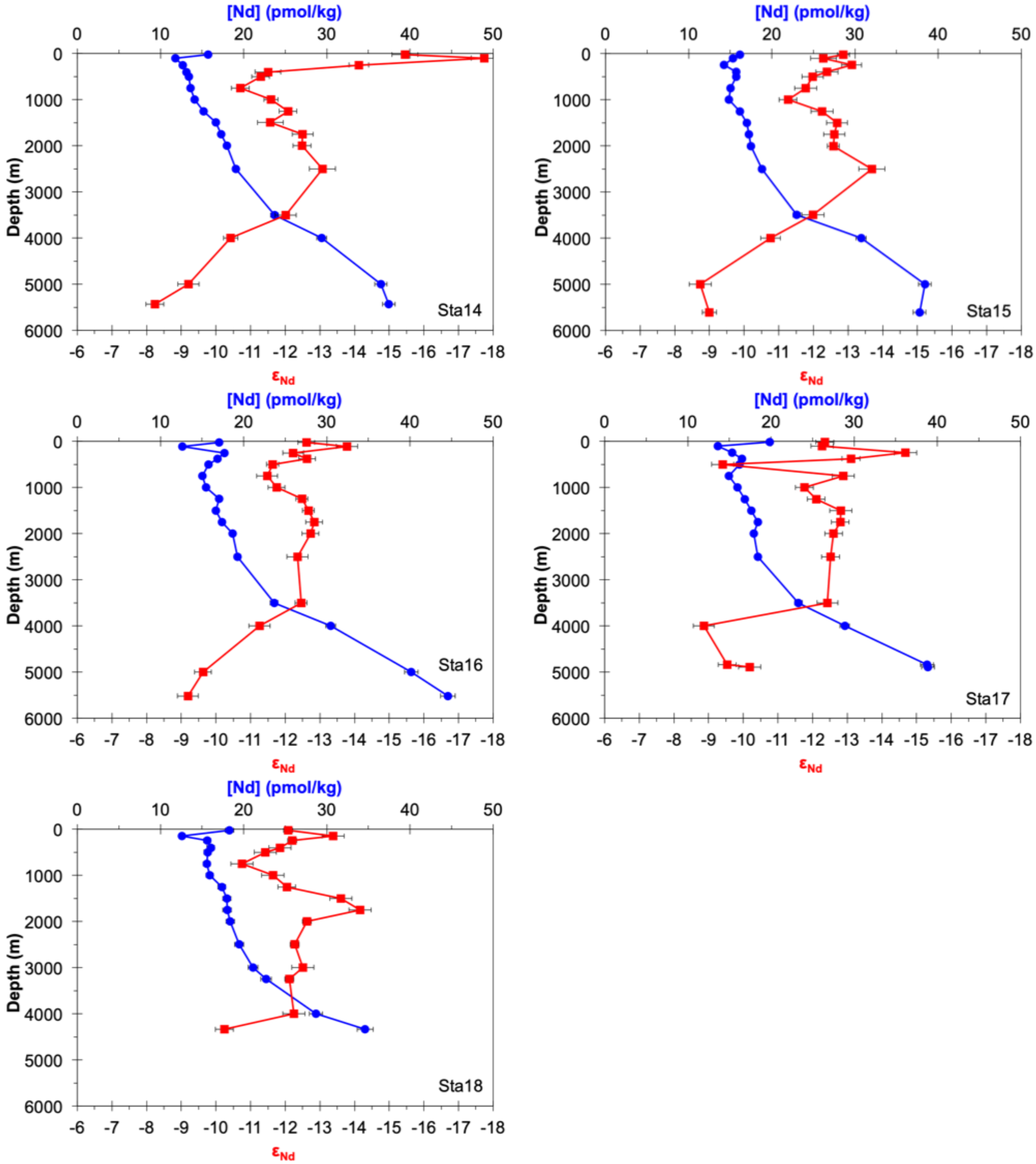

Figure S2.

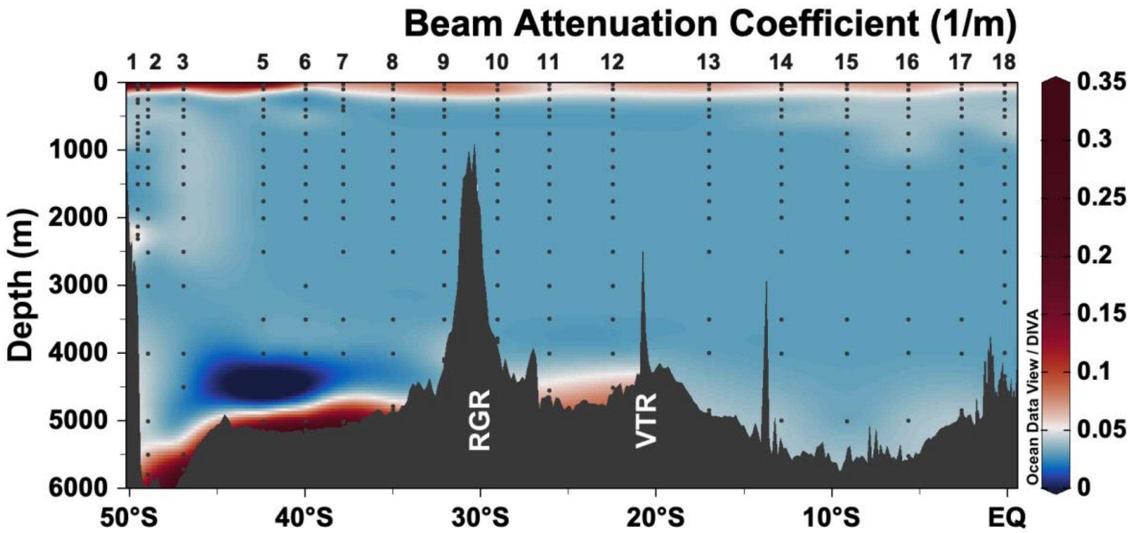
Beam Attenuation Coefficient (1/m)
1 2 3 5 6 7 8 9 10 11 12 13 14 15 16 17 18
Depth (m)
0
1000
2000
3000
4000
5000
6000
RGR
VTR
50°S
40°S
30°S
20°S
10°S
EQ
0.35
0.3
0.25
0.2
0.15
0.1
0.05
0
Ocean Data View / DIVA

Figure S3.

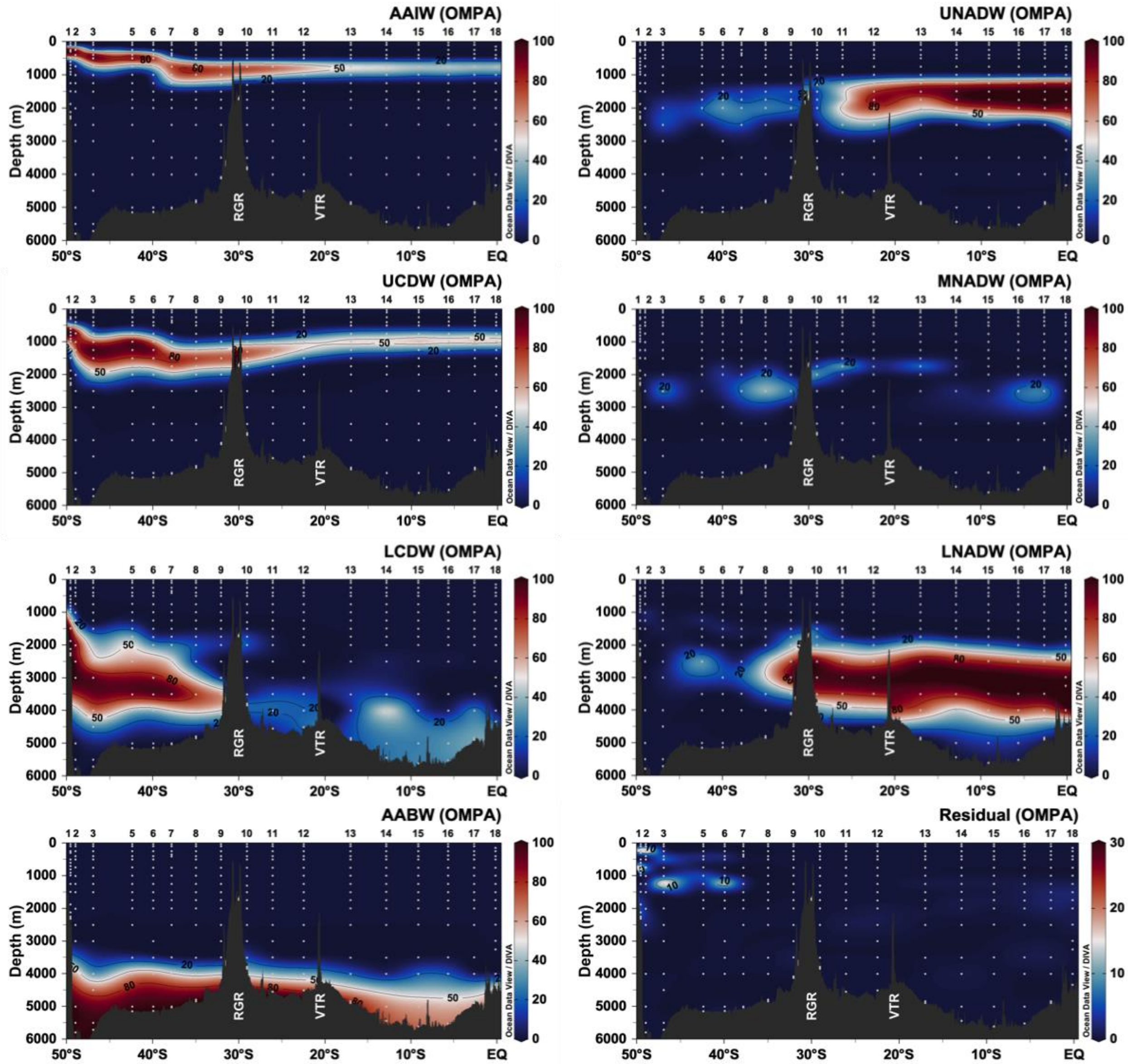

AAIW (OMPA)
UNADW (OMPA)
UCDW (OMPA)
MNADW (OMPA)
LCDW (OMPA)
LNADW (OMPA)
AABW (OMPA)
Residual (OMPA)
Depth (m)
RGR
VTR
50°S
40°S
30°S
20°S
10°S
EQ
Ocean Data View / DIVA

Figure S4.

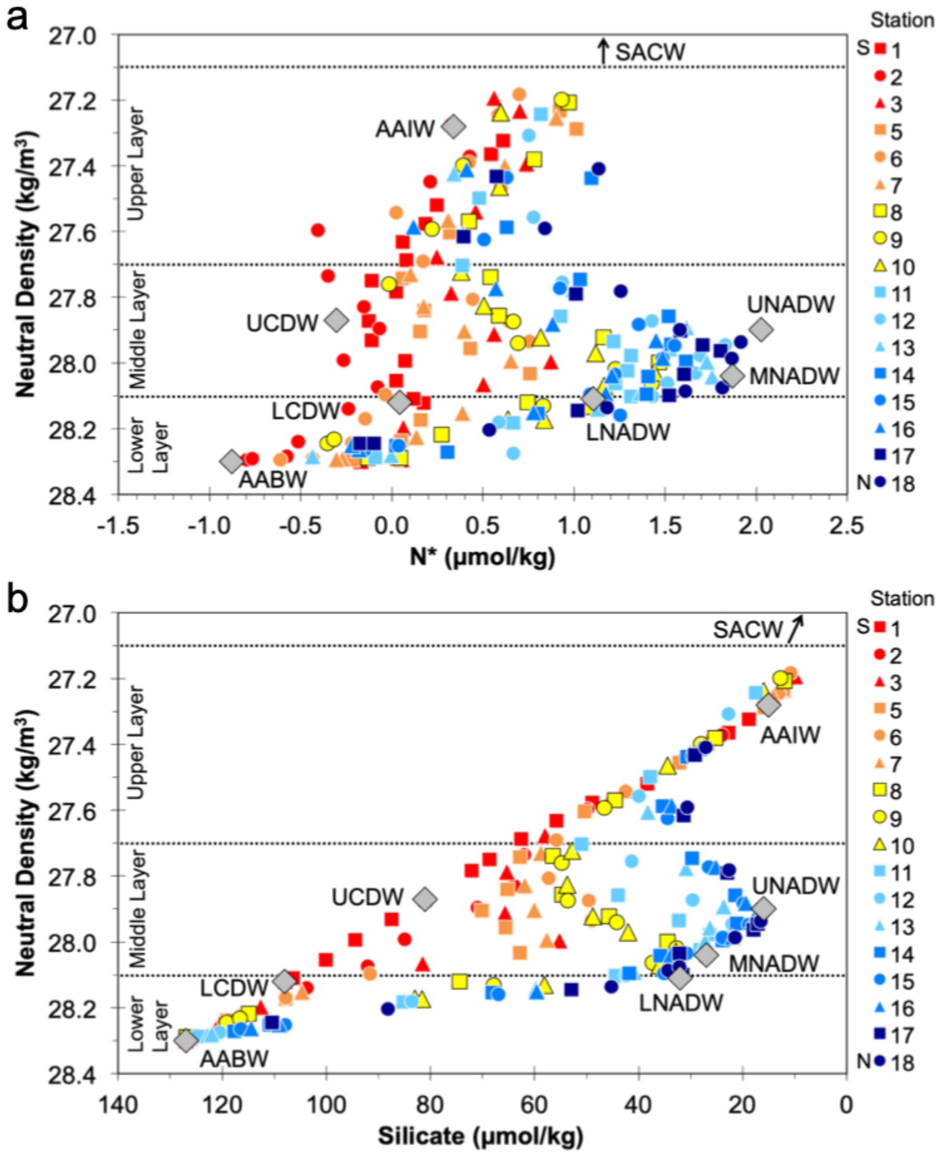
a
Neutral Density (kg/m³)
N* (µmol/kg)
SACW
AAIW
UCDW
UNADW
MNADW
LCDW
LNADW
AABW
Upper Layer
Middle Layer
Lower Layer
Station
S 1
2
3
5
6
7
8
9
10
11
12
13
14
15
16
17
N 18
b
Neutral Density (kg/m³)
Silicate (µmol/kg)
SACW
AAIW
UCDW
UNADW
MNADW
LCDW
LNADW
AABW
Upper Layer
Middle Layer
Lower Layer
Station
S 1
2
3
5
6
7
8
9
10
11
12
13
14
15
16
17
N 18

Figure S5.

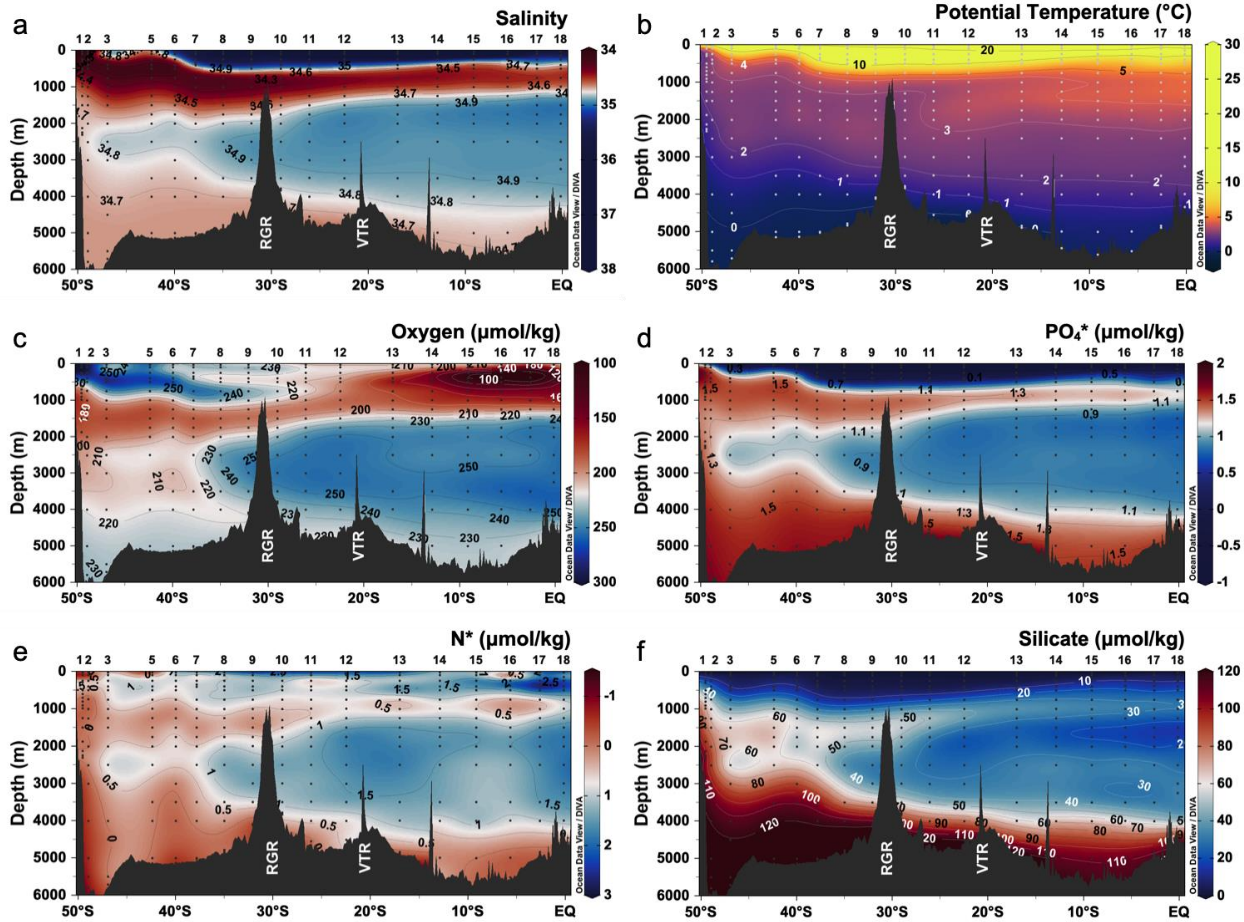
a
Salinity
Depth (m)
RGR
VTR
50°S
40°S
30°S
20°S
10°S
EQ
Ocean Data View / DIVA
b
Potential Temperature (°C)
c
Oxygen (µmol/kg)
d
PO₄* (µmol/kg)
e
N* (µmol/kg)
f
Silicate (µmol/kg)

Figure S6.

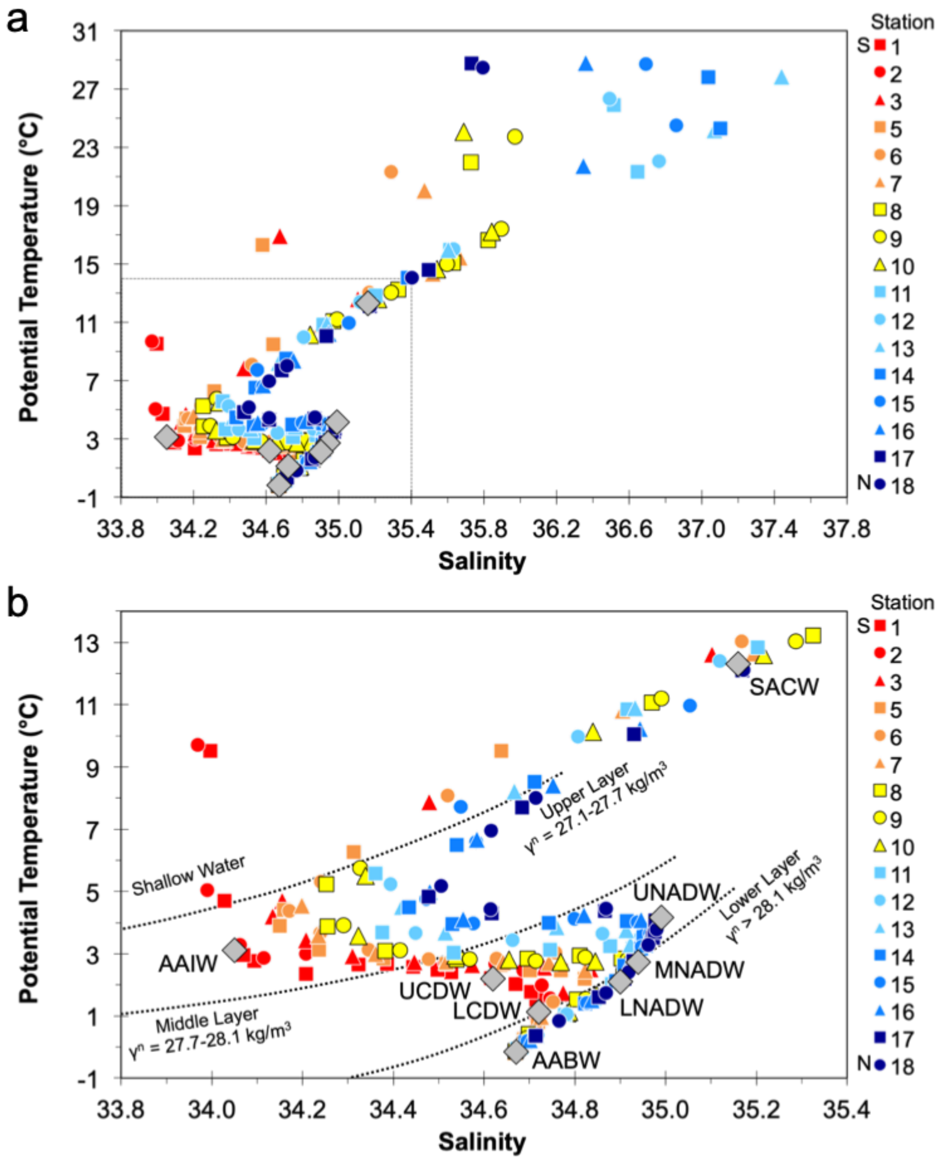
a
Potential Temperature (°C)
Salinity
Station
S
N
b
Shallow Water
Upper Layer
γ^n = 27.1-27.7 kg/m³
Middle Layer
γ^n = 27.7-28.1 kg/m³
Lower Layer
γ^n > 28.1 kg/m³
SACW
AAIW
UCDW
LCDW
UNADW
MNADW
LNADW
AABW

Figure S7.

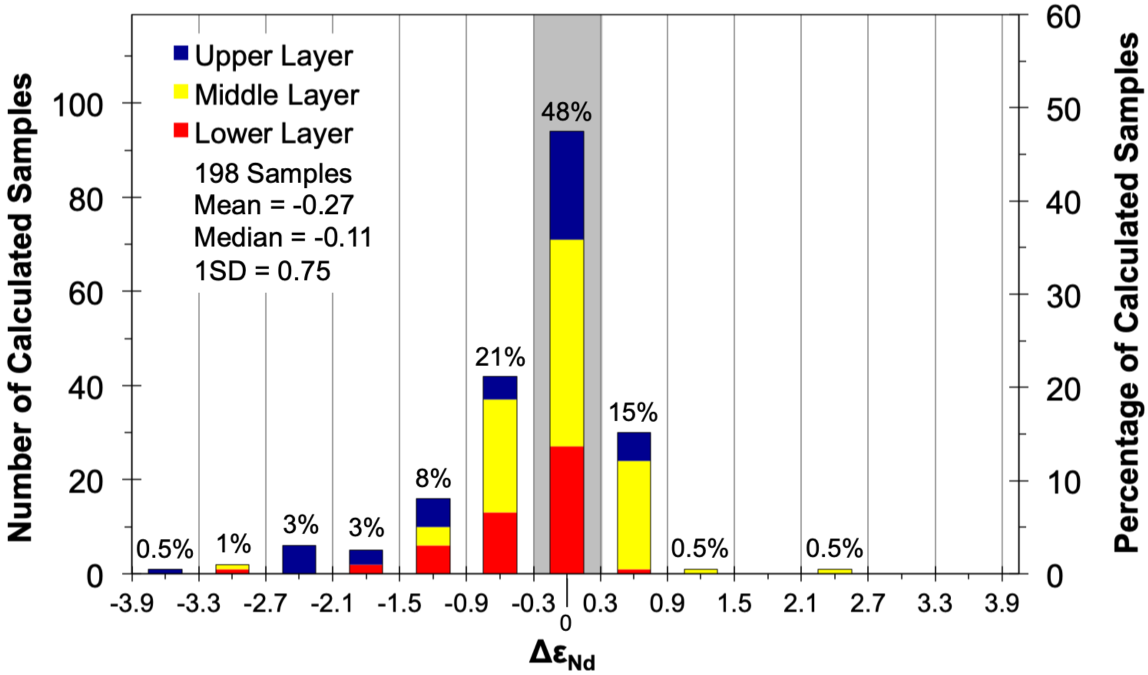
Upper Layer
Middle Layer
Lower Layer
198 Samples
Mean = -0.27
Median = -0.11
1SD = 0.75
48%
21%
15%
8%
3%
3%
1%
0.5%
0.5%
0.5%
Number of Calculated Samples
Percentage of Calculated Samples
$\Delta\varepsilon_{Nd}$
-3.9
-3.3
-2.7
-2.1
-1.5
-0.9
-0.3
0
0.3
0.9
1.5
2.1
2.7
3.3
3.9
0
20
40
60
80
100
0
10
20
30
40
50
60

Figure S8.

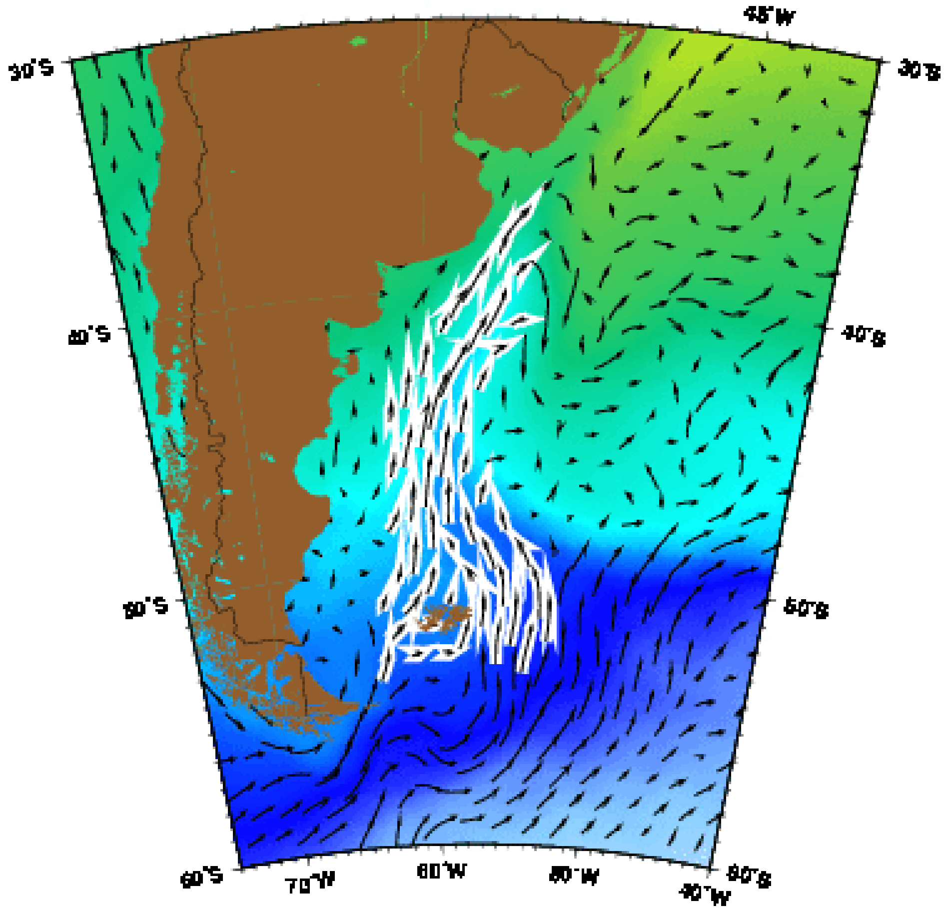

Figure S9.

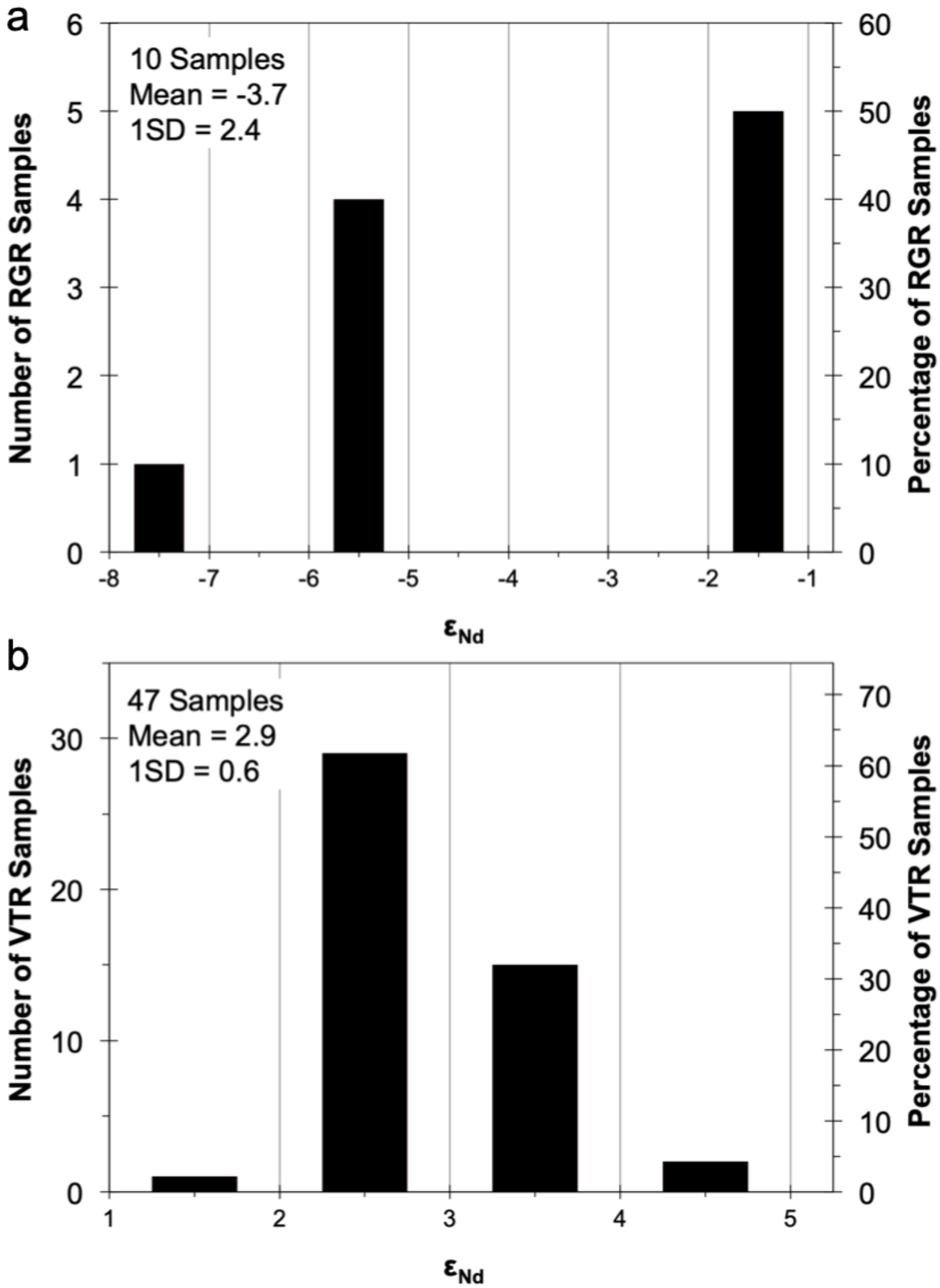
a
10 Samples
Mean = -3.7
1SD = 2.4
Number of RGR Samples
Percentage of RGR Samples
0
1
2
3
4
5
6
0
10
20
30
40
50
60
-8
-7
-6
-5
-4
-3
-2
-1
ε_{Nd}
b
47 Samples
Mean = 2.9
1SD = 0.6
Number of VTR Samples
Percentage of VTR Samples
0
10
20
30
0
10
20
30
40
50
60
70
1
2
3
4
5
ε_{Nd}

Figure S10.

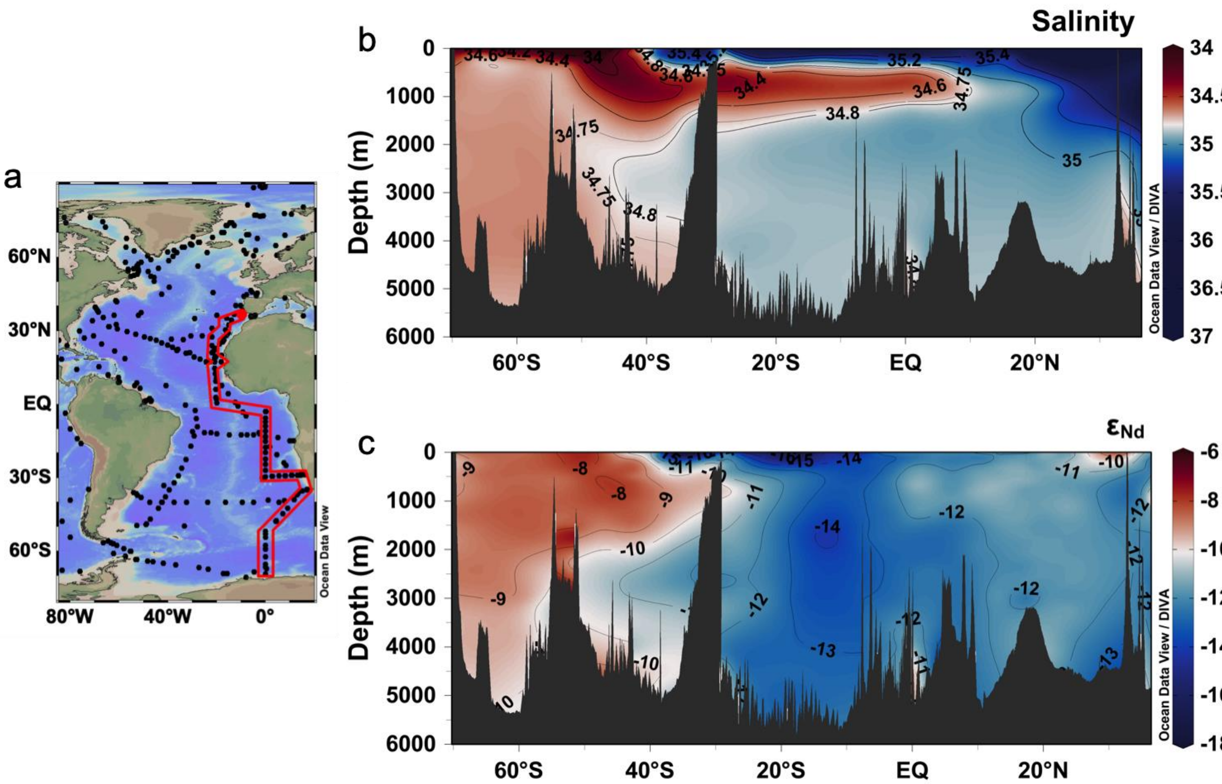

a
60°N
30°N
EQ
30°S
60°S
80°W
40°W
0°
Ocean Data View
b
Salinity
Depth (m)
0
1000
2000
3000
4000
5000
6000
60°S
40°S
20°S
EQ
20°N
34
34.5
35
35.5
36
36.5
37
Ocean Data View / DIVA
c
εNd
-6
-8
-10
-12
-14
-16
-18

Table S1. Data for the 17 seawater profiles collected from the SAMT. Sampling location, depth, salinity, potential temperature, neutral density, oxygen concentration, silicate concentration, nutrient concentration, PO_4^*, N^*, ε_{Nd}, external 2 standard deviation of ε_{Nd}, Nd concentration, external 2 standard deviation of Nd concentration, fractional contributions of water masses calculated based on the OMPA, predicted ε_{Nd} based on water mass mixing calculations, and $\Delta\varepsilon_{Nd}$-value (= measured ε_{Nd} – predicted ε_{Nd}).

Table S2. ε_{Nd} of volcanic rocks from the RGR (Gibson et al., 2005; Hoernle et al., 2015) and VTR (Bongiolo et al., 2015; Halliday et al., 1992; Kogarko et al., 2003; Marques et al., 1999; Peyve and Skolotnev, 2014; Siebel et al., 2000).

Table S1.

Depth	Salinity	Potential Temperature	Neutral Density	Oxygen	Silicate	Phosphate	Nitrate	PO_4^*	N^*	ε_{Nd}	Ext. 2sd	[Nd]	Ext. 2sd	SACW	AAIW	UCDW	UNADW	MNADW	LNADW	LCDW	AABW	Predicted ε_{Nd}	$\Delta\varepsilon_{Nd}$
m		°C	kg/m^3	µmol/kg	µmol/kg	µmol/kg	µmol/kg	µmol/kg	µmol/kg			pmol/kg	pmol/kg										
Station 1 (-49.55°N -52.69°E)																							
2312	34.72	1.11	28.12	197.70	107.95	2.19	32.21	1.36	0.17	-8.60	0.26	21.86	0.44							100%		-8.50	-0.10
2248	34.72	1.19	28.11	195.20	106.38	2.19	32.29	1.36	0.12	-8.48	0.26	21.45	0.43							100%		-8.50	0.02
2123	34.72	1.53	28.05	186.10	100.10	2.21	32.50	1.33	0.02	-8.29	0.26	19.58	0.39							100%		-8.50	0.21
1874	34.70	1.79	27.99	179.00	94.49	2.24	32.91	1.31	0.07	-8.02	0.26	17.68	0.35							100%		-8.50	0.48
1497	34.67	2.03	27.93	172.60	87.45	2.29	33.58	1.33	-0.11	-8.04	0.26	16.13	0.32							100%		-8.50	0.46
1248	34.62	2.21	27.87	170.20	81.01	2.34	34.28	1.36	-0.13	-7.96	0.26	14.85	0.30			29%				73%		-8.39	0.43
987	34.53	2.41	27.78	171.80	72.08	2.37	34.95	1.40	0.02	-7.75	0.26	13.35	0.27			67%				34%		-8.21	0.46
902	34.50	2.49	27.75	174.70	68.64	2.38	34.94	1.42	-0.11	-8.20	0.26	13.12	0.26			79%				21%		-8.14	-0.07
800	34.44	2.59	27.69	181.10	62.53	2.36	34.82	1.44	0.08	-7.92	0.26	12.80	0.26			100%						-8.00	0.08
701	34.39	2.68	27.63	191.30	55.74	2.33	34.35	1.47	0.06	-7.88	0.26	12.84	0.26			100%						-8.00	0.12
599	34.32	2.65	27.58	206.60	48.90	2.27	33.63	1.50	0.18	-7.97	0.26	11.85	0.24	1%	10%	88%						-8.03	0.06
500	34.21	2.36	27.52	238.80	38.31	2.18	32.23	1.60	0.25	-8.16	0.28	11.34	0.23		54%	46%						-8.05	-0.12
300	34.09	2.78	27.36	274.70	22.78	1.96	29.10	1.58	0.54	-8.04	0.26	10.67	0.21		100%							-8.10	0.06
250	34.07	2.96	27.32	286.60	18.85	1.89	28.04	1.58	0.61	-8.09	0.26	10.47	0.21		100%							-8.10	0.01
100	34.03	4.71	27.07	298.80	5.69	1.66	22.52	1.41	-0.89	-8.15	0.26	9.84	0.20										
24	34.00	9.51	26.29	288.40	0.00	1.03	13.06	0.73	-0.44	-7.52	0.26	8.62	0.17										
Station 2 (-48.97°N -48.88°E)																							
5797	34.67	-0.14	28.30	224.80	125.74	2.31	33.03	1.64	-0.80	-8.10	0.26	40.67	0.81								100%	-8.00	-0.10
5497	34.67	-0.12	28.29	224.40	125.35	2.30	32.97	1.63	-0.77	-8.12	0.26	35.94	0.72								100%	-8.00	-0.12
5000	34.67	-0.08	28.28	221.80	124.84	2.29	32.98	1.60	-0.58	-8.13	0.26	34.65	0.69								100%	-8.00	-0.13
4001	34.69	0.24	28.24	213.40	119.73	2.26	32.65	1.53	-0.52	-8.27	0.26	29.31	0.59							38%	62%	-8.13	-0.14
3004	34.73	1.06	28.14	199.40	103.77	2.18	31.59	1.37	-0.24	-8.60	0.26	22.96	0.46						0%	100%		-8.52	-0.08
2509	34.75	1.57	28.07	194.20	92.09	2.12	30.93	1.28	-0.08	-8.98	0.31	20.10	0.40							100%		-8.50	-0.48
2007	34.73	1.98	27.99	182.90	84.92	2.17	31.48	1.27	-0.27	-8.49	0.31	17.12	0.34							100%		-8.50	0.01
1504	34.69	2.47	27.90	179.60	70.97	2.18	31.90	1.26	-0.07	-8.62	0.31	15.48	0.31			60%	1%			38%		-8.31	-0.31
1253	34.63	2.68	27.83	177.70	63.95	2.23	32.60	1.30	-0.15	-8.87	0.31	14.81	0.30			84%			8%	9%		-8.51	-0.35
1003	34.51	2.69	27.73	177.50	61.96	2.34	34.04	1.40	-0.35	-8.32	0.31	13.71	0.27			89%			10%	1%		-8.60	0.27
746	34.37	2.85	27.60	195.10	49.82	2.32	33.64	1.48	-0.41	-7.80	0.31	12.36	0.25	3%		100%						-8.05	0.25
497	34.21	3.00	27.45	234.60	31.69	2.12	31.18	1.51	0.21	-7.94	0.31	11.23	0.22	20%	46%	34%						-8.48	0.54
400	34.11	2.87	27.37	265.20	24.04	1.99	29.38	1.56	0.43	-7.98	0.31	10.72	0.21	4%	90%	7%						-8.18	0.20
248	34.06	3.28	27.28	292.30	14.95	1.83	26.64	1.55	0.33	-8.08	0.31	10.32	0.21		100%							-8.10	0.02
99	33.99	5.05	26.99	296.70	4.11	1.61	21.27	1.35	-1.28	-8.22	0.26	9.67	0.19										
25	33.97	9.71	26.21	289.10	0.00	1.07	14.35	0.77	0.16	-11.34	0.31	9.39	0.19										

Table S1. Continued

Depth	Salinity	Potential Temperature	Neutral Density	Oxygen	Silicate	Phosphate	Nitrate	PO_4^*	N^*	ε_{Nd}	Ext. 2sd	[Nd]	Ext. 2sd	SACW	AAIW	UCDW	UNADW	MNADW	LNADW	LCDW	AABW	Predicted ε_{Nd}	$\Delta\varepsilon_{Nd}$
m		°C	kg/m^3	µmol/kg	µmol/kg	µmol/kg	µmol/kg	µmol/kg	µmol/kg			pmol/kg	pmol/kg										
Station 3 (-46.93°N -47.22°E)																							
5715	34.67	-0.16	28.30	223.10	126.90	2.26	32.95	1.58	-0.17	-8.12	0.30	40.37	0.81								100%	-8.00	-0.12
5501	34.67	-0.13	28.29	222.20	126.23	2.24	33.00	1.56	0.05	-7.92	0.24	38.04	0.76								100%	-8.00	0.08
4500	34.68	0.17	28.24	215.50	120.57	2.23	32.62	1.51	-0.14	-8.38	0.13	30.37	0.61							30%	70%	-8.10	-0.29
4001	34.71	0.59	28.20	208.40	112.56	2.18	32.02	1.42	0.06	-8.61	0.13	26.53	0.53							73%	27%	-8.30	-0.30
3001	34.77	1.73	28.06	202.20	81.52	1.97	29.10	1.17	0.50	-9.34	0.30	20.03	0.40						4%	96%		-8.67	-0.67
2502	34.83	2.50	28.00	212.50	55.23	1.74	25.91	1.01	0.87	-10.59	0.30	17.59	0.35				19%	30%		51%		-10.44	-0.15
2001	34.73	2.56	27.91	187.40	65.65	2.03	30.16	1.15	0.56	-9.23	0.30	15.95	0.32			47%	14%			39%		-8.96	-0.28
1501	34.57	2.64	27.79	175.40	65.27	2.25	33.44	1.30	0.33	-8.31	0.19	13.75	0.27			86%			4%	10%		-8.32	0.01
1250	34.45	2.74	27.68	182.10	57.98	2.30	34.10	1.39	0.25	-8.12	0.30	12.63	0.25			100%						-8.00	-0.12
1002	34.31	2.92	27.54	207.00	42.67	2.19	32.65	1.42	0.46	-8.15	0.19	12.12	0.24	21%	8%	71%						-8.42	0.27
751	34.21	3.43	27.39	238.20	26.93	2.01	30.01	1.42	0.74	-8.15	0.19	10.71	0.21	31%	49%	20%						-8.76	0.60
502	34.13	4.20	27.23	278.10	12.05	1.74	25.65	1.38	0.70	-8.10	0.13	9.85	0.20		100%							-8.10	0.00
401	34.16	4.70	27.19	275.00	9.93	1.70	24.91	1.32	0.56	-8.16	0.30	9.96	0.20		100%							-8.10	-0.06
250	34.48	7.87	26.99	237.10	6.36	1.37	20.02	0.78	0.90	-8.43	0.19	10.54	0.21										
99	35.10	12.61	26.61	217.90	2.81	0.78	10.52	0.07	0.92	-9.03	0.30	12.09	0.24										
26	34.67	16.91	25.19	242.00	0.41	0.18	0.35	-0.39	0.41	-7.63	0.30	11.18	0.22										
Station 5 (-42.38°N -44.02°E)																							
5146	34.67	-0.16	28.29	222.10	126.93	2.25	32.82	1.57	-0.21	-8.05	0.30	41.82	0.84								100%	-8.00	-0.05
5001	34.67	-0.15	28.29	222.20	126.48	2.24	32.90	1.56	0.02	-8.22	0.26	35.28	0.71								100%	-8.00	-0.22
4000	34.69	0.25	28.24	213.40	119.20	2.20	32.37	1.47	0.05	-8.24	0.26	27.12	0.54							40%	61%	-8.13	-0.11
3502	34.72	0.80	28.17	206.50	107.73	2.14	31.44	1.37	0.16	-8.59	0.30	23.11	0.46							93%	7%	-8.44	-0.15
2503	34.82	2.20	28.03	213.20	62.80	1.79	26.61	1.06	0.76	-10.34	0.30	16.98	0.34						40%	60%		-10.03	-0.31
2000	34.77	2.47	27.96	195.00	65.59	1.96	28.89	1.12	0.43	-9.84	0.28	15.08	0.30			25%	21%			54%		-9.31	-0.53
1748	34.70	2.46	27.90	181.70	70.15	2.12	31.18	1.21	0.15	-9.21	0.30	18.94	0.38			56%	4%			40%		-8.46	-0.75
1500	34.64	2.64	27.84	177.70	65.18	2.18	32.13	1.24	0.18	-9.55	0.32	13.68	0.27			77%	6%			17%		-8.46	-1.10
1250	34.52	2.67	27.74	176.90	62.78	2.29	33.68	1.35	0.06	-8.23	0.28	15.36	0.31			89%			8%	3%		-8.52	0.29
999	34.38	2.85	27.60	193.40	50.38	2.26	33.64	1.42	0.32	-7.98	0.28	11.23	0.22			100%						-8.00	0.02
748	34.24	3.13	27.46	227.80	32.14	2.10	31.32	1.45	0.60	-7.94	0.30	12.48	0.25	28%	36%	37%						-8.63	0.70
500	34.15	3.89	27.29	263.10	15.89	1.82	27.30	1.37	1.01	-8.79	0.32	10.51	0.21	16%	85%							-8.49	-0.30
400	34.16	4.41	27.23	264.70	12.13	1.76	26.27	1.32	0.92	-8.79	0.32	10.25	0.21	14%	88%							-8.44	-0.35
247	34.31	6.26	27.10	247.80	7.56	1.55	22.85	1.01	0.90	-8.15	0.30	10.32	0.21										
100	34.64	9.51	26.84	246.70	2.95	1.00	13.51	0.45	0.47	-7.59	0.28	11.27	0.23										
25	34.58	16.31	25.36	255.10	0.00	0.24	0.00	-0.25	-0.74	-6.94	0.32	9.07	0.18										

Table S1. Continued

Depth	Salinity	Potential Temperature	Neutral Density	Oxygen	Silicate	Phosphate	Nitrate	PO_4^*	N^*	ε_{Nd}	Ext. 2sd	[Nd]	Ext. 2sd	SACW	AAIW	UCDW	UNADW	MNADW	LNADW	LCDW	AABW	Predicted ε_{Nd}	$\Delta\varepsilon_{Nd}$
m		°C	kg/m^3	μmol/kg	μmol/kg	μmol/kg	μmol/kg	μmol/kg	μmol/kg			pmol/kg	pmol/kg										
Station 6 (-39.97°N -42.49°E)																							
5132	34.67	-0.16	28.30	221.30	127.25	2.30	33.13	1.61	-0.61	-7.97	0.18	39.23	0.78								100%	-8.00	0.03
5000	34.67	-0.14	28.29	221.50	126.67	2.29	33.11	1.60	-0.44	-8.18	0.18	37.83	0.76								100%	-8.00	-0.18
4001	34.69	0.22	28.24	214.10	119.63	2.25	32.75	1.52	-0.22	-8.42	0.18	29.16	0.58							36%	64%	-8.12	-0.30
3501	34.72	0.82	28.17	205.40	107.82	2.17	31.65	1.40	-0.15	-8.72	0.18	24.45	0.49							96%	4%	-8.46	-0.26
3002	34.75	1.44	28.10	201.20	91.64	2.08	30.32	1.28	-0.04	-10.17	0.18	18.61	0.37						17%	84%		-9.15	-1.02
2000	34.82	2.90	27.93	207.50	48.98	1.79	26.51	1.02	0.76	-10.55	0.18	16.16	0.32			24%	35%	16%		25%		-10.64	0.09
1751	34.76	3.04	27.87	195.70	49.60	1.92	28.56	1.09	0.65	-10.27	0.18	15.61	0.31			56%	31%	9%		5%		-10.18	-0.09
1499	34.63	2.84	27.81	183.60	57.34	2.15	31.99	1.25	0.44	-8.98	0.18	14.01	0.28			80%	11%		10%			-9.17	0.19
1250	34.48	2.82	27.69	183.70	55.85	2.28	33.68	1.38	0.17	-8.35	0.18	13.11	0.26			100%						-8.00	-0.35
1000	34.35	3.13	27.54	202.80	42.52	2.23	32.82	1.44	0.02	-8.31	0.18	12.16	0.24	27%	2%	71%						-8.53	0.22
750	34.24	3.66	27.39	231.80	26.14	2.04	30.21	1.42	0.42	-9.62	0.18			42%	39%	19%						-9.00	
500	34.17	4.38	27.25	267.40	13.05	1.77	26.09	1.35	0.58	-8.36	0.18	10.35	0.21	10%	92%							-8.34	-0.02
399	34.24	5.31	27.18	251.80	10.80	1.71	25.18	1.20	0.70	-8.45	0.18	10.19	0.20	35%	68%							-8.92	0.47
250	34.52	8.09	26.99	223.00	7.41	1.41	20.63	0.74	0.83	-9.04	0.18	10.47	0.21										
101	35.17	13.03	26.58	215.80	2.48	0.72	9.71	0.01	0.94	-9.09	0.18	12.39	0.25										
25	35.29	21.32	24.62	224.40	0.99	0.08	0.00	-0.59	1.45	-9.41	0.18	16.92	0.34										
Station 7 (-37.83°N -41.12°E)																							
5023	34.67	-0.15	28.29	221.20	126.70	2.27	33.09	1.59	-0.27	-8.01	0.28	37.34	0.75								100%	-8.00	-0.01
5000	34.67	-0.15	28.29	221.20	126.97	2.27	33.04	1.62	-0.30	-8.18	0.37	37.92	0.76								100%	-8.00	-0.18
4000	34.69	0.34	28.23	212.30	116.90	2.20	32.42	1.50	0.13	-9.88	0.37	27.69	0.55							50%	51%	-8.18	-1.71
3500	34.73	0.98	28.15	203.40	104.69	2.13	31.52	1.37	0.39	-8.32	0.37	23.91	0.48						1%	99%		-8.56	0.24
2501	34.82	2.47	27.99	210.20	57.66	1.80	26.65	1.05	0.65	-10.28	0.28	16.80	0.34				23%	21%		56%		-10.25	-0.03
2000	34.74	2.71	27.90	191.10	60.10	2.00	29.54	1.14	0.40	-12.57	0.37	15.26	0.31			47%	24%			29%		-9.40	-3.17
1748	34.64	2.73	27.83	180.00	61.83	2.17	31.94	1.25	0.17	-9.22	0.37	14.04	0.28			80%	7%		6%	8%		-8.75	-0.47
1500	34.52	2.76	27.73	179.30	58.76	2.27	33.42	1.34	0.10	-9.32	0.37	12.96	0.26			85%	14%		1%			-8.87	-0.45
1249	34.36	3.01	27.57	198.10	45.54	2.23	33.10	1.41	0.31	-8.30	0.28	11.78	0.24	4%	49%	48%						-8.12	-0.19
1000	34.24	3.59	27.40	230.90	27.37	2.03	30.22	1.40	0.62	-7.93	0.37	10.80	0.22	7%	74%	19%						-8.23	0.30
751	34.20	4.55	27.25	254.90	14.15	1.77	26.46	1.28	0.90	-8.46	0.37	9.92	0.20	16%	84%							-8.48	0.02
409	34.91	10.82	26.82	212.10	4.51	1.04	14.83	0.30	1.05	-9.23	0.28	10.66	0.21										
349	35.19	12.66	26.68	216.00	3.00	0.78	10.66	0.09	1.02	-10.24	0.37	11.51	0.23										
249	35.52	14.35	26.57	221.70	1.94	0.53	6.46	-0.12	0.81	-10.53	0.37	12.38	0.25										
101	35.67	15.43	26.44	224.20	1.59	0.34	3.15	-0.30	0.62	-10.06	0.37	12.10	0.24										
24	35.47	20.04	25.12	228.50	0.87	0.07	0.00	-0.54	1.55	-10.55	0.37	12.47	0.25										

Table S1. Continued

Depth	Salinity	Potential Temperature	Neutral Density	Oxygen	Silicate	Phosphate	Nitrate	PO_4^*	N^*	ε_{Nd}	Ext. 2sd	[Nd]	Ext. 2sd	SACW	AAIW	UCDW	UNADW	MNADW	LNADW	LCDW	AABW	Predicted ε_{Nd}	$\Delta\varepsilon_{Nd}$
m		°C	kg/m^3	µmol/kg	µmol/kg	µmol/kg	µmol/kg	µmol/kg	µmol/kg			pmol/kg	pmol/kg										
Station 8 (-35.01°N -39.44°E)																							
4838	34.67	-0.13	28.29	219.90	126.81	2.25	33.16	1.56	0.05	-8.70	0.32	39.13	0.78								100%	-8.00	-0.70
4787	34.67	-0.13	28.29	220.30	126.78	2.27	33.14	1.57	-0.13	-8.59	0.26	37.62	0.75								100%	-8.00	-0.59
4000	34.70	0.43	28.22	211.10	114.90	2.18	32.26	1.44	0.27	-8.30	0.28	34.08	0.68							59%	41%	-8.22	-0.07
3501	34.80	1.53	28.12	223.00	74.33	1.80	26.69	1.12	0.74	-10.07	0.28	23.71	0.47						23%	78%		-9.38	-0.69
2500	34.90	2.84	28.00	235.60	34.43	1.47	22.19	0.86	1.47	-11.57	0.26	17.42	0.35					47%	47%	6%		-12.06	0.50
2001	34.81	2.94	27.92	210.10	45.70	1.75	26.31	1.00	1.16	-11.24	0.32	15.46	0.31			25%	30%	28%		17%		-10.91	-0.33
1749	34.70	2.85	27.86	190.20	54.69	2.01	29.82	1.14	0.59	-9.65	0.28	14.96	0.30			62%	21%	8%		9%		-9.64	-0.01
1501	34.54	2.81	27.74	183.20	56.47	2.21	32.97	1.30	0.54	-9.10	0.30	13.53	0.27			79%	18%		3%			-9.20	0.10
1251	34.38	3.11	27.57	197.70	44.56	2.20	32.77	1.38	0.42	-8.71	0.28	12.20	0.24	5%	46%	49%						-8.14	-0.57
1001	34.26	3.87	27.38	226.60	25.32	2.00	29.96	1.35	0.78	-7.88	0.32	10.74	0.21	10%	73%	17%						-8.30	0.43
751	34.25	5.24	27.21	245.90	11.95	1.71	25.56	1.17	0.97	-8.57	0.26	10.04	0.20	23%	77%							-8.66	0.09
501	34.97	11.07	26.83	206.00	4.75	1.05	14.95	0.28	0.96	-10.35	0.32	11.20	0.22										
400	35.33	13.23	26.67	212.90	2.70	0.70	9.38	-0.03	0.97	-10.24	0.28	11.69	0.23										
251	35.63	15.06	26.50	216.10	1.75	0.43	5.35	-0.28	1.19	-10.35	0.28	12.12	0.24										
100	35.82	16.63	26.28	229.00	0.48	0.13	0.00	-0.52	0.81	-11.42	0.28	9.86	0.20										
24	35.73	21.98	24.78	219.70	0.47	0.03	0.00	-0.66	2.09	-11.43	0.26	11.29	0.23										
Station 9 (-32.09°N -37.46°E)																							
4121	34.69	0.21	28.25	214.70	119.19	2.23	32.29	1.50	-0.35	-7.77	0.32	32.18	0.64							36%	64%	-8.12	0.36
4085	34.69	0.29	28.23	214.10	116.58	2.21	32.03	1.48	-0.32	-8.55	0.13	30.95	0.62							46%	54%	-8.16	-0.39
3498	34.82	1.55	28.13	232.60	67.86	1.72	25.51	1.10	0.83	-10.43	0.19	25.32	0.51						37%	64%		-9.90	-0.52
2999	34.91	2.44	28.06	243.30	37.27	1.43	21.57	0.87	1.43	-11.88	0.24	19.79	0.40						93%	7%		-11.87	0.00
2500	34.92	2.81	28.02	239.60	32.71	1.44	21.50	0.86	1.23	-11.88	0.19	17.72	0.35					24%	75%	1%		-12.16	0.27
1999	34.82	2.88	27.94	215.40	44.16	1.74	25.72	1.02	0.69	-9.95	0.19	15.69	0.31			25%	25%		38%	12%		-11.08	0.81
1749	34.71	2.77	27.87	196.30	53.59	1.98	29.48	1.15	0.67	-9.32	0.19	14.71	0.29			57%	10%		26%	7%		-9.94	-0.01
1499	34.57	2.84	27.76	186.10	54.78	2.18	31.93	1.29	-0.01	-8.52	0.19	13.25	0.27			75%	20%		5%			-9.44	0.12
1249	34.41	3.12	27.59	194.10	46.63	2.23	32.95	1.39	0.22	-8.68	0.19	12.51	0.25	5%	41%	54%						-8.14	-0.38
1001	34.29	3.91	27.40	219.10	28.08	2.05	30.30	1.35	0.39	-9.41	0.32	11.31	0.23	11%	68%	21%						-8.31	-1.10
752	34.33	5.76	27.20	231.00	12.77	1.71	25.45	1.08	0.93	-8.68	0.19	10.36	0.21	29%	71%							-8.79	0.12
500	34.99	11.21	26.81	206.40	4.73	0.99	14.32	0.22	1.22	-10.08	0.22	11.22	0.22										
401	35.29	13.03	26.68	212.10	3.05	0.72	9.94	-0.02	1.25	-10.16	0.22	11.30	0.23										
250	35.60	15.02	26.48	216.50	1.77	0.43	5.15	-0.28	1.03	-10.74	0.13	11.46	0.23										
101	35.89	17.41	26.13	229.30	0.74	0.09	0.00	-0.55	1.33	-11.86	0.22	10.02	0.20										
26	35.97	23.71	24.46	212.20	0.35	0.00	0.00	-0.74	2.57	-12.87	0.19	10.69	0.21										

Table S1. Continued

Depth	Salinity	Potential Temperature	Neutral Density	Oxygen	Silicate	Phosphate	Nitrate	PO_4^*	N^*	ε_{Nd}	Ext. 2sd	[Nd]	Ext. 2sd	SACW	AAIW	UCDW	UNADW	MNADW	LNADW	LCDW	AABW	Predicted ε_{Nd}	$\Delta\varepsilon_{Nd}$
m		°C	kg/m^3	μmol/kg	μmol/kg	μmol/kg	μmol/kg	μmol/kg	μmol/kg			pmol/kg	pmol/kg										
Station 10 (-29.06°N -35.78°E)																							
3835	34.78	1.09	28.17	229.10	82.95	1.86	27.56	1.22	0.64	-9.90	0.13	31.39	0.63						46%	22%	32%	-9.68	-0.22
3786	34.79	1.13	28.17	229.80	81.63	1.84	27.50	1.21	0.84	-10.06	0.22	30.17	0.60						48%	21%	32%	-9.74	-0.32
3502	34.85	1.68	28.13	239.60	58.08	1.61	24.04	1.03	1.07	-11.06	0.19	25.99	0.52						81%	3%	16%	-11.05	-0.01
2999	34.91	2.38	28.07	246.10	35.97	1.42	21.18	0.88	1.16	-11.52	0.32	20.39	0.41						96%	4%		-11.97	0.46
2502	34.91	2.69	28.03	242.50	32.85	1.42	21.44	0.86	1.44	-12.07	0.22	17.93	0.36				1%		99%			-12.11	0.04
2001	34.84	2.75	27.97	223.90	42.04	1.64	24.53	0.97	1.12	-11.08	0.19	16.72	0.33			6%	13%	37%	24%	20%		-11.44	0.36
1750	34.77	2.73	27.92	208.30	48.84	1.82	27.17	1.06	0.82	-10.66	0.37	15.61	0.31			33%	19%	4%	29%	15%		-10.62	-0.04
1501	34.65	2.81	27.83	191.60	53.78	2.05	30.40	1.19	0.51	-9.79	0.19	14.56	0.29			68%	11%		21%			-9.73	-0.05
1296	34.54	2.95	27.72	186.00	52.86	2.18	32.44	1.30	0.38	-9.17	0.37	13.68	0.27			72%	28%					-9.60	0.43
1003	34.32	3.57	27.46	209.80	34.47	2.12	31.68	1.37	0.59	-8.32	0.19	11.89	0.24	8%	60%	32%						-8.23	-0.09
751	34.34	5.51	27.24	220.60	15.95	1.83	26.94	1.14	0.60	-8.83	0.37	10.91	0.22	26%	74%							-8.73	-0.10
500	34.84	10.14	26.90	205.80	5.89	1.17	16.93	0.40	1.02	-9.81	0.22	11.35	0.23										
402	35.22	12.60	26.71	211.50	3.25	0.80	11.00	0.06	1.02	-10.53	0.37	12.06	0.24										
252	35.54	14.64	26.52	215.80	1.91	0.48	6.14	-0.23	1.20	-10.53	0.22	11.77	0.24										
107	35.84	17.21	26.14	231.50	0.61	0.07	0.00	-0.56	1.59	-11.54	0.22	9.61	0.19										
25	35.69	24.05	24.14	211.50	0.27	0.01	0.00	-0.73	2.40	-12.95	0.37	9.64	0.19										
Station 11 (-26.09°N -34.26°E)																							
4548	34.67	-0.06	28.29	218.70	124.47	2.24	32.79	1.54	-0.09	-8.37	0.37	36.82	0.74							9%	91%	-8.03	-0.34
4001	34.78	1.04	28.18	228.80	85.16	1.87	27.71	1.23	0.67	-10.72	0.37	31.74	0.63						43%	21%	36%	-9.55	-1.17
3493	34.88	2.03	28.10	246.20	44.49	1.47	22.03	0.92	1.31	-11.80	0.30	24.76	0.50						81%	19%		-11.48	-0.33
3000	34.92	2.49	28.06	247.90	32.63	1.38	20.59	0.85	1.23	-12.16	0.30	19.58	0.39						100%			-12.10	-0.06
2503	34.93	2.82	28.02	246.30	28.15	1.36	20.36	0.82	1.29	-12.50	0.30	18.25	0.36				35%		66%			-12.36	-0.14
2000	34.93	3.18	27.98	240.40	26.32	1.40	20.98	0.83	1.31	-11.94	0.37	16.69	0.33				58%		43%			-12.56	0.62
1749	34.88	3.24	27.94	225.40	32.24	1.56	23.33	0.89	1.22	-11.80	0.30	15.72	0.31			13%	30%	57%				-12.17	0.37
1501	34.75	3.13	27.86	200.70	43.94	1.86	27.92	1.06	0.92	-10.80	0.30	14.04	0.28			50%	49%		1%			-10.74	-0.06
1249	34.53	3.04	27.70	185.80	51.03	2.17	32.28	1.29	0.39	-9.46	0.30	12.60	0.25			69%	31%					-9.77	0.32
998	34.38	3.68	27.50	195.90	37.83	2.16	32.16	1.33	0.48	-9.22	0.30	11.68	0.23	10%	52%	38%						-8.26	-0.96
750	34.36	5.57	27.24	212.90	17.50	1.85	27.52	1.11	0.82	-9.87	0.37	10.55	0.21	27%	71%	2%						-8.74	-1.13
501	34.92	10.85	26.83	201.10	5.59	1.10	15.65	0.30	0.87	-10.69	0.30	10.46	0.21										
403	35.20	12.83	26.65	209.10	3.13	0.78	10.30	0.02	0.73	-10.97	0.30	10.73	0.21										
249	35.61	15.98	26.26	206.10	1.64	0.41	4.11	-0.36	0.39	-12.61	0.28	9.03	0.18										
100	36.64	21.31	25.68	212.60	0.77	0.08	0.00	-0.62	1.46	-13.73	0.37	8.25	0.16										
25	36.51	25.90	24.20	201.80	0.35	0.01	0.00	-0.76	2.43	-16.37	0.37	9.04	0.18										

Table S1. Continued

Depth	Salinity	Potential Temperature	Neutral Density	Oxygen	Silicate	Phosphate	Nitrate	PO_4^*	N^*	ε_{Nd}	Ext. 2sd	[Nd]	Ext. 2sd	SACW	AAIW	UCDW	UNADW	MNADW	LNADW	LCDW	AABW	Predicted ε_{Nd}	$\Delta\varepsilon_{Nd}$
m		°C	kg/m^3	µmol/kg	µmol/kg	µmol/kg	µmol/kg	µmol/kg	µmol/kg			pmol/kg	pmol/kg										
Station 12 (-22.47°N -32.73°E)																							
4510	34.69	0.10	28.28	218.00	120.55	2.19	32.92	1.49	0.67	-8.50	0.24	35.03	0.70							23%	77%	-8.07	-0.42
4002	34.78	1.05	28.18	229.70	83.56	1.87	27.59	1.23	0.59	-12.63	0.37	29.42	0.59						45%	19%	36%	-9.63	-3.01
3499	34.89	2.06	28.10	246.00	42.41	1.44	21.75	0.90	1.43	-11.52	0.28	22.85	0.46						85%	15%		-11.60	0.08
3002	34.92	2.51	28.06	247.30	32.09	1.37	20.71	0.83	1.51	-12.11	0.24	19.01	0.38				1%		100%			-12.10	0.00
2501	34.94	2.83	28.03	246.90	27.48	1.33	20.28	0.79	1.67	-12.50	0.37	17.36	0.35				39%		61%			-12.40	-0.10
1999	34.95	3.29	27.98	244.80	22.20	1.32	20.13	0.77	1.69	-12.34	0.28	17.75	0.36				86%		15%			-12.83	0.50
1751	34.95	3.55	27.95	235.70	22.05	1.37	21.09	0.77	1.83	-12.30	0.24	16.97	0.34				99%		1%			-12.99	0.69
1502	34.86	3.65	27.87	212.10	29.67	1.63	24.77	0.89	1.43	-11.80	0.28	16.00	0.32			20%	80%					-12.15	0.34
1250	34.66	3.43	27.76	188.50	41.31	1.99	29.98	1.12	0.93	-10.54	0.26	14.50	0.29			50%	50%					-10.73	0.19
999	34.45	3.66	27.56	182.50	40.01	2.18	32.81	1.27	0.78	-10.00	0.24	12.76	0.26	11%	40%	49%						-8.26	-1.74
752	34.39	5.23	27.31	191.70	22.79	2.01	30.09	1.16	0.75	-9.67	0.28	11.60	0.23	24%	63%	13%						-8.64	-1.03
502	34.81	9.98	26.90	194.60	7.58	1.27	18.51	0.44	0.95	-10.47	0.24	11.36	0.23										
401	35.12	12.40	26.68	202.70	3.97	0.87	11.93	0.08	0.86	-11.26	0.24	11.23	0.22										
250	35.63	16.03	26.27	209.10	1.83	0.37	3.81	-0.38	0.68	-12.69	0.24	10.06	0.20										
100	36.76	22.04	25.56	210.90	0.75	0.05	0.00	-0.69	1.81	-13.71	0.37	9.22	0.18										
24	36.49	26.35	24.04	201.80	0.46	0.03	0.00	-0.76	2.09	-13.87	0.24	8.56	0.17										
Station 13 (-17.02°N -30.59°E)																							
4893	34.68	0.02	28.28	218.20	122.80	2.26	32.73	1.56	-0.44	-8.73	0.37	36.53	0.73							16%	84%	-8.05	-0.68
4844	34.68	0.04	28.28	218.50	121.97	2.22	32.63	1.52	0.00	-8.44	0.17	38.25	0.76							18%	83%	-8.05	-0.39
3999	34.84	1.59	28.14	239.80	59.71	1.60	24.02	1.02	1.13	-11.81	0.37	28.68	0.57						79%	1%	20%	-10.91	-0.90
3503	34.89	2.14	28.09	245.90	40.89	1.44	21.69	0.90	1.36	-11.94	0.17	23.26	0.47						88%	13%		-11.69	-0.25
2501	34.92	2.66	28.04	242.00	32.77	1.39	21.38	0.83	1.76	-12.47	0.20	19.65	0.39				2%		98%			-12.12	-0.36
2002	34.93	3.05	28.00	241.40	27.24	1.38	21.10	0.81	1.73	-12.02	0.17	18.29	0.37				49%		52%			-12.48	0.46
1749	34.92	3.30	27.96	233.30	26.26	1.45	22.02	0.83	1.53	-12.42	0.17	17.39	0.35				54%	37%	8%			-12.72	0.30
1502	34.91	3.77	27.89	222.20	23.65	1.51	22.99	0.82	1.62	-12.16	0.17	17.15	0.34			5%	95%					-12.79	0.63
1251	34.76	3.86	27.78	190.80	30.89	1.87	28.16	1.01	0.99	-12.48	0.17	15.84	0.32			31%	70%					-11.67	-0.30
1000	34.51	3.70	27.60	178.70	38.29	2.19	32.54	1.26	0.39	-10.81	0.17	14.44	0.29	12%	30%	58%						-8.84	-1.97
750	34.42	4.52	27.42	175.40	30.10	2.20	32.69	1.26	0.34	-10.27	0.17	12.38	0.25	18%	53%	29%						-9.36	-0.92
500	34.67	8.22	27.09	151.30	13.91	1.75	26.99	0.69	1.66	-14.38	0.37	12.54	0.25										
401	34.93	10.89	26.82	162.30	7.93	1.33	20.16	0.33	1.63	-13.20	0.37	12.06	0.24										
250	35.60	15.99	26.25	189.90	2.36	0.52	6.30	-0.31	0.74	-13.68	0.37	10.58	0.21										
100	37.07	24.18	25.16	218.00	0.69	0.08	0.00	-0.63	1.49	-14.38	0.17	10.16	0.20										
24	37.44	27.85	24.28	193.60	0.67	0.02	0.00	-0.83	2.34	-13.20	0.17	13.60	0.27										

Table S1. Continued

Depth	Salinity	Potential Temperature	Neutral Density	Oxygen	Silicate	Phosphate	Nitrate	PO_4^*	N^*	ε_{Nd}	Ext. 2sd	[Nd]	Ext. 2sd	SACW	AAIW	UCDW	UNADW	MNADW	LNADW	LCDW	AABW	Predicted ε_{Nd}	$\Delta\varepsilon_{Nd}$
m		°C	kg/m^3	µmol/kg	µmol/kg	µmol/kg	µmol/kg	µmol/kg	µmol/kg			pmol/kg	pmol/kg										
Station 14 (-12.89°N -29.22°E)																							
5435	34.69	0.15	28.27	219.70	117.67	2.16	32.01	1.47	0.31	-8.24	0.26	37.45	0.75						1%	26%	73%	-8.10	-0.13
4999	34.71	0.33	28.25	221.40	110.92	2.13	31.22	1.45	0.02	-9.21	0.30	36.49	0.73						9%	26%	65%	-8.37	-0.84
4000	34.82	1.40	28.15	235.00	68.07	1.71	25.25	1.10	0.80	-10.43	0.20	29.37	0.59						37%	64%		-9.91	-0.51
3502	34.89	2.12	28.10	243.60	41.84	1.45	21.84	0.89	1.40	-12.01	0.30	23.71	0.47						85%	15%		-11.61	-0.40
2500	34.91	2.61	28.04	237.90	35.79	1.45	21.89	0.86	1.41	-13.07	0.37	19.05	0.38					10%	84%	6%		-11.93	-1.14
1999	34.95	3.17	27.99	243.40	23.86	1.34	20.36	0.78	1.61	-12.48	0.26	17.96	0.36				74%		27%			-12.72	0.23
1748	34.95	3.57	27.94	236.10	21.10	1.39	20.97	0.78	1.53	-12.50	0.30	17.30	0.35				100%					-13.00	0.50
1497	34.91	4.06	27.86	212.60	21.49	1.55	23.53	0.81	1.52	-11.57	0.37	16.67	0.33			5%	95%					-12.79	1.22
1250	34.74	3.99	27.75	183.40	29.72	1.92	28.96	1.02	1.04	-12.08	0.26	15.17	0.30			32%	69%					-11.63	-0.45
998	34.53	3.95	27.59	165.20	35.39	2.21	33.20	1.21	0.63	-11.59	0.20	14.09	0.28	14%	31%	53%	3%					-9.13	-2.46
749	34.43	4.49	27.44	167.20	30.62	2.20	33.54	1.21	1.09	-10.70	0.26	13.63	0.27	18%	51%	30%	2%					-9.45	-1.25
500	34.54	6.50	27.25	151.30	19.25	2.02	30.96	0.93	1.45	-11.29	0.26	13.41	0.27										
401	34.71	8.52	27.07	143.60	13.33	1.77	27.04	0.64	1.50	-11.50	0.37	13.11	0.26										
250	35.38	14.08	26.52	146.50	4.68	1.06	15.51	-0.05	1.28	-14.12	0.28	12.68	0.25										
100	37.10	24.30	25.15	213.60	0.58	0.10	0.00	-0.59	1.11	-17.74	0.37	11.80	0.24										
25	37.04	27.81	23.99	197.10	0.48	0.10	0.00	-0.70	1.19	-15.45	0.37	15.70	0.31										
Station 15 (-9.15°N -28.00°E)																							
5607	34.69	0.18	28.27	219.60	116.35	2.19	31.86	1.49	-0.15	-9.00	0.20	37.76	0.76						2%	28%	70%	-8.15	-0.85
5001	34.72	0.38	28.25	222.20	107.94	2.11	30.83	1.43	0.04	-8.73	0.32	38.41	0.77						13%	26%	61%	-8.49	-0.25
4000	34.83	1.42	28.16	236.30	66.97	1.68	25.42	1.08	1.25	-10.77	0.28	30.73	0.61						69%	8%	23%	-10.52	-0.25
3498	34.91	2.21	28.10	249.30	35.12	1.38	20.38	0.89	1.09	-11.99	0.32	23.00	0.46						99%	2%		-12.05	0.06
2499	34.93	2.76	28.03	240.90	30.77	1.41	20.99	0.87	1.22	-13.69	0.37	18.82	0.38				20%		80%			-12.25	-1.44
2003	34.95	3.23	27.99	240.50	23.94	1.37	20.68	0.79	1.49	-12.57	0.17	17.46	0.35				77%		23%			-12.75	0.18
1750	34.97	3.66	27.95	238.20	18.89	1.35	20.40	0.76	1.55	-12.60	0.30	17.26	0.35				100%					-13.00	0.40
1500	34.94	4.01	27.88	220.20	19.86	1.49	22.51	0.80	1.35	-12.68	0.30	16.98	0.34				100%					-13.00	0.32
1252	34.80	4.13	27.77	186.30	26.53	1.85	27.76	0.97	0.92	-12.25	0.32	16.18	0.32			25%	76%					-11.94	-0.31
1000	34.58	3.98	27.62	165.90	34.47	2.19	32.72	1.19	0.51	-11.27	0.26	14.86	0.30	16%	22%	62%						-9.04	-2.23
750	34.47	4.75	27.43	145.70	29.66	2.33	35.02	1.21	0.63	-11.78	0.32	15.05	0.30	21%	46%	33%						-9.52	-2.25
499	34.58	6.60	27.27	110.60	20.92	2.27	34.98	0.95	1.47	-11.98	0.30	15.74	0.31										
400	34.55	7.73	27.07	97.80	17.37	2.19	33.86	0.80	1.55	-12.39	0.32	15.72	0.31										
249	35.05	10.97	26.90	93.40	10.33	1.75	27.33	0.33	2.03	-13.10	0.28	14.22	0.28										
100	36.86	24.49	24.91	204.70	0.26	0.10	0.00	-0.68	1.17	-12.29	0.37	15.32	0.31										
25	36.69	28.70	23.42	192.70	0.21	0.09	0.00	-0.76	1.34	-12.86	0.17	16.17	0.32										

Table S1. Continued

Depth	Salinity	Potential Temperature	Neutral Density	Oxygen	Silicate	Phosphate	Nitrate	PO_4^*	N^*	ε_{Nd}	Ext. 2sd	[Nd]	Ext. 2sd	SACW	AAIW	UCDW	UNADW	MNADW	LNADW	LCDW	AABW	Predicted ε_{Nd}	$\Delta\varepsilon_{Nd}$
m		°C	kg/m^3	μmol/kg	μmol/kg	μmol/kg	μmol/kg	μmol/kg	μmol/kg			pmol/kg	pmol/kg										
Station 16 (-5.67°N -28.46°E)																							
5519	34.70	0.24	28.26	219.60	114.46	2.18	31.74	1.49	-0.18	-9.19	0.30	44.57	0.89						4%	30%	66%	-8.22	-0.97
4999	34.72	0.38	28.25	220.50	108.99	2.14	30.99	1.45	-0.22	-9.63	0.24	40.16	0.80						11%	32%	58%	-8.44	-1.19
3998	34.84	1.51	28.15	240.40	59.64	1.62	23.93	1.05	0.78	-11.26	0.30	30.45	0.61						80%		20%	-10.90	-0.35
3500	34.91	2.24	28.09	252.50	31.64	1.35	19.92	0.84	1.17	-12.46	0.17	23.66	0.47						100%			-12.10	-0.36
2500	34.92	2.69	28.04	238.50	33.71	1.44	21.51	0.85	1.21	-12.35	0.30	19.26	0.39					25%	72%	3%		-12.09	-0.26
2000	34.96	3.31	27.98	243.00	21.98	1.34	20.20	0.78	1.49	-12.73	0.24	18.68	0.37				90%		11%			-12.88	0.15
1751	34.97	3.78	27.93	238.30	17.90	1.35	20.30	0.76	1.45	-12.84	0.24	17.41	0.35				100%					-13.00	0.16
1499	34.95	4.08	27.88	220.40	19.42	1.52	22.40	0.83	0.88	-12.67	0.17	16.66	0.33				100%					-13.00	0.33
1247	34.82	4.25	27.77	185.80	25.10	1.86	27.53	0.98	0.57	-11.96	0.17	17.06	0.34			23%	78%					-12.04	-0.44
999	34.55	4.10	27.59	162.10	33.61	2.25	33.25	1.23	0.12	-11.75	0.24	15.47	0.31	16%	27%	56%						-9.11	-2.64
749	34.48	4.98	27.41	142.90	28.22	2.35	35.09	1.21	0.41	-11.48	0.30	15.02	0.30	23%	47%	30%						-9.68	-1.79
499	34.58	6.66	27.26	114.80	20.86	2.26	34.66	0.96	1.32	-11.64	0.17	15.78	0.32										
376	34.75	8.41	27.12	78.90	16.64	2.18	34.62	0.68	2.30	-12.63	0.24	16.83	0.34										
250	34.94	10.22	26.95	98.00	11.74	1.82	28.54	0.43	2.10	-12.23	0.30	17.70	0.35										
109	36.35	21.71	25.34	164.70	1.48	0.48	3.17	-0.53	-1.30	-13.79	0.30	12.63	0.25										
25	36.36	28.78	23.15	194.80	0.28	0.09	0.00	-0.75	1.37	-12.61	0.24	17.03	0.34										
Station 17 (-2.64°N -28.91°E)																							
4891	34.71	0.37	28.24	219.50	110.34	2.14	31.12	1.45	-0.17	-10.19	0.32	38.88	0.78						8%	35%	57%	-8.38	-1.81
4840	34.71	0.37	28.25	219.10	110.37	2.14	31.13	1.44	-0.10	-9.53	0.26	38.75	0.77						8%	36%	56%	-8.38	-1.16
4000	34.85	1.61	28.14	245.60	52.90	1.53	22.64	0.98	1.02	-8.86	0.30	28.87	0.58						67%	34%		-10.96	2.10
3500	34.91	2.19	28.10	253.30	31.56	1.31	19.79	0.81	1.52	-12.43	0.30	23.30	0.47						100%			-12.10	-0.33
2502	34.93	2.76	28.03	239.40	32.21	1.40	21.31	0.82	1.60	-12.52	0.26	18.42	0.37					31%	69%	0%		-12.20	-0.32
2001	34.97	3.51	27.96	247.20	17.92	1.27	19.38	0.73	1.80	-12.61	0.26	17.93	0.36				100%					-13.00	0.39
1750	34.98	3.72	27.95	243.20	17.09	1.29	19.70	0.73	1.71	-12.80	0.26	18.42	0.37				100%					-13.00	0.20
1501	34.98	4.07	27.90	233.50	16.26	1.35	20.39	0.73	1.58	-12.81	0.32	17.61	0.35				100%					-13.00	0.19
1251	34.87	4.39	27.79	191.70	22.93	1.75	26.21	0.90	1.01	-12.10	0.26	16.85	0.34			16%	85%					-12.32	0.21
1000	34.62	4.30	27.62	157.10	31.33	2.21	32.83	1.16	0.39	-11.76	0.26	15.95	0.32	19%	19%	62%						-9.25	-2.52
750	34.48	4.83	27.43	150.80	29.16	2.29	34.36	1.20	0.57	-12.89	0.32	14.94	0.30	22%	46%	32%						-9.58	-3.31
499	34.68	7.71	27.18	97.10	17.85	2.15	34.14	0.76	2.33	-9.41	0.32	16.23	0.32										
374	34.93	10.05	26.98	77.00	13.06	1.93	31.27	0.42	2.88	-13.11	0.26	16.49	0.33										
249	35.17	12.10	26.77	95.30	9.26	1.60	25.18	0.21	2.17	-14.68	0.32	15.31	0.31										
100	35.49	14.61	26.49	117.10	5.73	1.22	18.63	-0.04	1.77	-12.28	0.32	13.60	0.27										
17	35.73	28.75	22.68	195.00	0.37	0.03	0.00	-0.80	2.13	-12.35	0.26	19.83	0.40										

Table S1. Continued

Depth	Salinity	Potential Temperature	Neutral Density	Oxygen	Silicate	Phosphate	Nitrate	PO_4^*	N^*	ε_{Nd}	Ext. 2sd	[Nd]	Ext. 2sd	SACW	AAIW	UCDW	UNADW	MNADW	LNADW	LCDW	AABW	Predicted ε_{Nd}	$\Delta\varepsilon_{Nd}$
m		°C	kg/m^3	μmol/kg	μmol/kg	μmol/kg	μmol/kg	μmol/kg	μmol/kg			pmol/kg	pmol/kg										
Station 18 (-0.18°N -32.88°E)																							
4338	34.77	0.83	28.20	228.40	88.12	1.89	27.92	1.25	0.53	-10.24	0.26	34.60	0.69						39%	20%	41%	-9.39	-0.85
3999	34.87	1.74	28.14	250.00	45.19	1.44	21.42	0.92	1.18	-12.25	0.32	28.69	0.57						99%		1%	-12.04	-0.21
3249	34.91	2.27	28.09	247.80	34.30	1.35	20.55	0.82	1.61	-12.11	0.13	22.69	0.45						100%	0%		-12.08	-0.03
2994	34.92	2.41	28.08	248.70	32.17	1.33	20.42	0.80	1.81	-12.51	0.32	21.14	0.42						100%			-12.10	-0.41
2498	34.94	2.74	28.05	247.40	27.38	1.30	20.03	0.77	1.85	-12.27	0.13	19.47	0.39				39%		61%			-12.40	0.13
2000	34.96	3.29	27.99	245.30	21.45	1.30	19.93	0.75	1.87	-12.62	0.13	18.37	0.37				91%		10%			-12.89	0.27
1750	34.98	3.79	27.94	242.30	16.50	1.28	19.66	0.71	1.92	-14.16	0.32	18.01	0.36				100%					-13.00	-1.16
1500	34.99	4.16	27.90	233.50	15.92	1.33	20.20	0.72	1.58	-13.60	0.32	17.99	0.36				100%					-13.00	-0.60
1252	34.87	4.46	27.78	189.50	22.66	1.74	26.35	0.87	1.26	-12.04	0.26	17.37	0.35			17%	84%					-12.30	0.26
998	34.61	4.43	27.59	156.60	30.70	2.17	32.76	1.12	0.84	-11.64	0.32	15.91	0.32	21%	21%	57%	1%					-9.43	-2.22
750	34.51	5.18	27.41	147.60	27.09	2.23	33.97	1.12	1.14	-10.75	0.32	15.56	0.31	26%	45%	29%						-9.86	-0.89
499	34.61	6.96	27.23	128.80	19.57	2.06	32.39	0.85	2.00	-11.43	0.32	15.65	0.31										
400	34.71	8.02	27.15	116.70	16.77	1.97	31.38	0.69	2.43	-11.85	0.32	16.04	0.32										
244	35.17	12.12	26.77	108.80	9.03	1.51	23.91	0.18	2.36	-12.20	0.13	15.61	0.31										
150	35.40	14.08	26.54	161.10	5.07	0.99	14.28	-0.04	1.26	-13.38	0.32	12.56	0.25										
22	35.79	28.45	22.83	196.90	0.47	0.03	0.00	-0.80	2.22	-12.09	0.13	18.30	0.37										

Table S2.

Sample ID	Latitude °N	Longitude °E	ε_{Nd}	Reference
RGR volcanic rocks				
DSDP072-0516F-128R-001/122-126	-30.28	-35.29	-1.2	3
DSDP072-0516F-128R-002/130-135	-30.28	-35.29	-1.4	3
74-516F-128-2,130-135	-30.28	-35.29	-1.4	3
74-516F-128-1,122-126	-30.28	-35.29	-1.2	3
DSDP072-0516F-128R-002W/063-084	-30.28	-35.29	-1.9	4
CON0016-011-001	-30.43	-36.02	-5.6	4
CON0016-011-002	-30.43	-36.02	-5.5	4
CON0016-011-002	-30.43	-36.02	-5.7	4
CON0016-012-001	-30.43	-36.02	-5.8	4
CON0016-012-003	-30.43	-36.02	-7.1	4
VTR volcanic rocks				
TD3	-20.50	-29.30	2.4	5
TD4	-20.50	-29.30	2.6	5
TD5	-20.50	-29.30	3.1	5
91TR80	-20.50	-29.30	3.0	6
91TR93	-20.50	-29.30	4.5	6
91TR98	-20.50	-29.30	3.7	6
91TR101A	-20.50	-29.30	3.6	6
91-MV-2	-20.50	-28.80	4.7	6
10745	-20.50	-29.30	3.9	7
10759	-20.50	-29.30	3.5	7
10761	-20.50	-29.30	2.2	7
10763	-20.50	-29.30	2.7	7
10764	-20.50	-29.30	2.8	7
10769	-20.50	-29.30	3.1	7
10770	-20.50	-29.30	2.4	7
10771	-20.50	-29.30	2.7	7
10773	-20.50	-28.80	2.9	7
10774	-20.50	-28.80	2.9	7
HIT-4	-20.50	-29.30	2.9	7
91-TR-7	-20.50	-29.30	3.3	8
91-TR-23	-20.50	-29.30	3.2	8
91-TR-31	-20.50	-29.30	3.7	8
91-TR-51	-20.50	-29.30	2.5	8
91-TR-57	-20.50	-29.30	2.7	8
91-TR-79	-20.50	-29.30	3.6	8
91-TR-88	-20.50	-29.30	2.6	8
91-TR-90	-20.50	-29.30	2.9	8
91-TR-97	-20.50	-29.30	2.7	8

Table S2. Continued

Sample ID	Latitude	Longitude	ε_{Nd}	Reference
	°N	°E		
VTR volcanic rocks				
91-TR-98	-20.50	-29.30	3.1	8
91-TR-103	-20.50	-29.30	3.4	8
91-TR-106	-20.50	-29.30	2.8	8
91-MV-2	-20.50	-28.80	2.9	8
V2403/2	-20.85	-34.05	2.2	9
V2403/4	-20.85	-34.05	2.6	9
V2403/12	-20.85	-34.05	1.6	9
V2410/5	-20.79	-34.92	3.9	9
V2410/12	-20.79	-34.92	2.2	9
V2414/1	-20.40	-35.80	2.6	9
EMB-02 A	-20.50	-29.30	2.5	10
EMB-04 A	-20.50	-29.30	2.4	10
EMB-06 A	-20.50	-29.30	2.6	10
EMB-09 A	-20.50	-29.30	3.0	10
EMB-11 A	-20.50	-29.30	4.0	10
EMB-15 A	-20.50	-29.30	2.4	10
EMB-16 A	-20.50	-29.30	2.5	10
EMB-19 A	-20.50	-29.30	2.6	10
XEN-02 A	-20.50	-29.30	2.1	10